ENGINEERING PLASMONIC NANOMATERIALS FOR SERS APPLICATIONS

Mariacristina Turino

UNIVERSITAT ROVIRA i VIRGILI

Engineering plasmonic nanomaterials for SERS applications

MARIACRISTINA TURINO

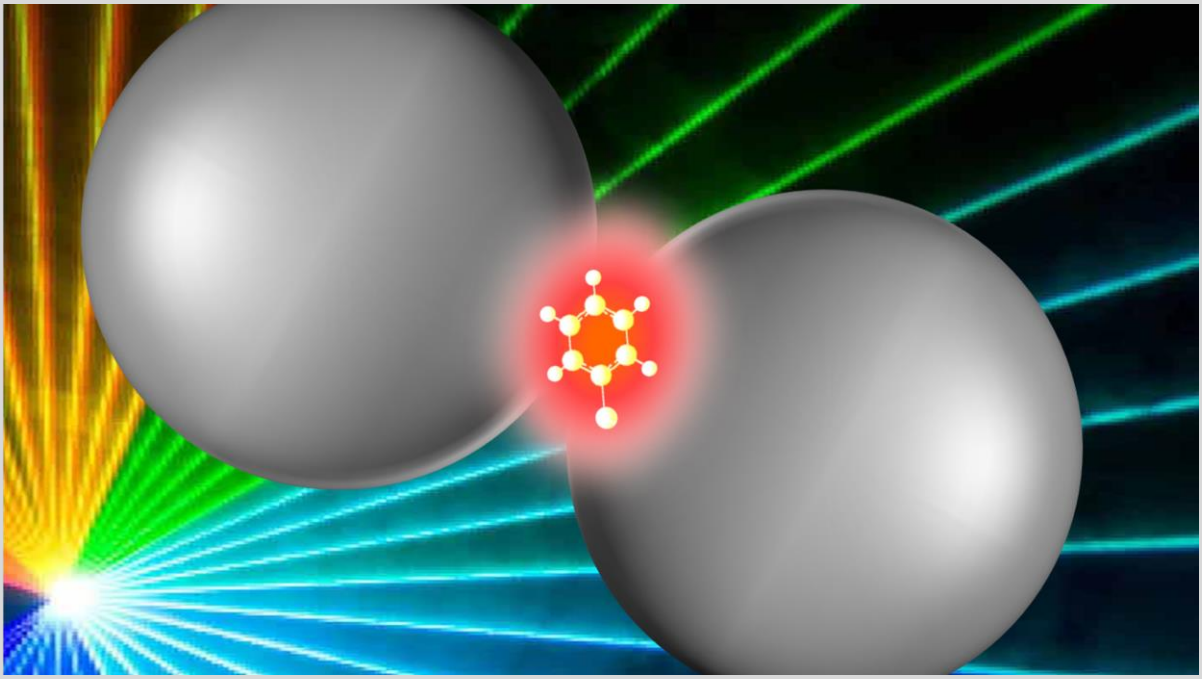

DOCTORAL THESIS
2022

UNIVERSITAT ROVIRA i VIRGILI

ZEPTONIC GROUP

ENGINEERING PLASMONIC NANOMATERIALS FOR SERS APPLICATIONS

Mariacristina Turino

DOCTORAL THESIS

Supervised by

Dr. Luca Guerrini

Prof. Ramón A. Álvarez-Puebla

FACULTY OF CHEMISTRY
DEPARTMENT OF PHYSICAL AND INORGANIC CHEMISTRY

Tarragona, 2022

UNIVERSITAT ROVIRA i VIRGILI

FAIG CONSTAR que aquest treball, titulat “ENGINEERING PLASMONIC NANOMATERIALS FOR SERS APPLICATIONS”, que presenta Mariacristina Turino per a l’obtenció del títol de Doctor, ha estat realitzat sota la meva direcció al Departament de Química Física i Inorgànica d’aquesta universitat.

HAGO CONSTAR que el presente trabajo, titulado “ENGINEERING PLASMONIC NANOMATERIALS FOR SERS APPLICATIONS”, que presenta Mariacristina Turino para la obtención del título de Doctor, ha sido realizado bajo mi dirección en el Departamento Química Física e Inorgánica de esta universidad.

I STATE that the present study, entitled “ENGINEERING PLASMONIC NANOMATERIALS FOR SERS APPLICATIONS”, presented by Mariacristina Turino for the award of the degree of Doctor, has been carried out under my supervision at the Department of Physical and Inorganic Chemistry of this university.

Tarragona, 21/07/2022

El/s director/s de la tesi doctoral
El/los director/es de la tesis doctoral
Doctoral Thesis Supervisor/s

Ramon [signatura] / [firma] / [signature]
Firmado digitalmente por Ramon Nombre de reconocimiento (DN): cn=Ramon, o=URV, ou, email=ramon.alvarez@urv.cat, c=ES
Fecha: 2022.07.21 15:01:45 +02'00'

Prof. Ramón A. Álvarez-Puebla

LUCA GUERRINI - DNI X6331661Z [signatura] / [firma] / [signature]
Digitally signed by LUCA GUERRINI - DNI X6331661Z
DN: c=ES, sn=GUERRINI, givenName=LUCA, serialNumber=IDCES-X6331661Z, cn=LUCA GUERRINI - DNI X6331661Z
Date: 2022.08.05 14:39:26 +02'00'

Dr. Luca Guerrini

CONTENTS

LIST OF ABBREVIATIONS AND ACRONYMS (by alphabetical order)

4-ATP: 4-aminothiophenol

AA: Ascorbic acid

ABT: 4-amino benzenethiol

Ag: Silver

AgNPs: Silver nanoparticles

Au: Gold

AuNPs: Gold nanospheres

AuNPs: Gold nanoparticles

AuNRs: Gold nanorods

AuNWs: Gold nanowires

BSA: Bovine serum albumin

BSI: British Standards Institution

BT: Benzenethiol

CE: Chemical enhancement

CT: Charge transfer

CTAB: Cetyltrimethylammonium bromide

Cu: Copper

Cys: Cysteine

DMAB: 4,4′-dimercaptoazobenzene

EDL: Electric double layer

EDX: Energy-dispersive X-ray spectroscopy

EF: Enhancement factor

EM: Electromagnetic mechanism

GSH: Glutathione

GSSG: Glutathione disulfide

HAADF STEM: High-angle annular dark-field scanning transmission electron microscopy

HOMO: Highest occupied molecular orbitals

IR: Infrared spectroscopy

ISO: International Organization for Standardization

LBL: layer-by-layer

LFEF: Local field enhancement factor

LSPR: Localized surface plasmon resonance

LUMO: Lowest unoccupied molecular orbitals

MUA: 11-Mercaptoundecanoic acid

MYP: 4-mercaptopyridine

NA: 1-naphthylamine

NPs: Nanoparticles

OA: Oleylamine

PAA: Poly(acrylic acid)

PAH: Poly(allylamine hydrochloride)

PBS: Phosphate buffer saline

PDDA: Poly(diallyldimethylammonium chloride)

PEG: Polyethylene glycol

PEG-SH: Thiolated polyethylene glycol

PEI: Branched polyethyleneimine

PHE: Phenol

PS: Polystyrene

SEM: Scanning electron microscopy

SERS: Surface-enhanced Raman scattering

TEM: Transmission electron microscopy

USFDA: US Food and Drug Administration

UV: Ultraviolet

Vis: Visible

THESIS SCOPE

Gold and silver nanoparticles show exceptional chemical, physical, and electrical properties. Most notably, they are capable of manipulating the light-matter interaction at the nanoscale. Their unique optical properties mainly arise from the generation of collective oscillations of the free conduction electrons, better known as localized surface plasmon resonances.

Metal nanoparticles' ability to absorb and concentrate the incident electromagnetic field at the nanostructure has been used in a variety of applications, including those based on the so-called plasmon-enhanced spectroscopies such as surface-enhanced Raman scattering (SERS) spectroscopy

SERS combines the inherent structural specificity and high experimental flexibility of Raman spectroscopy with the extremely high sensitivity provided by the plasmonic-mediated enhancement. As a result, SERS spectroscopy emerged as an ultrasensitive analytical tool that has been continuously expanding its range of applications in several fields, including sensing and biosensing, biology, medicine, environmental monitoring, food safety, or catalysi, among others. In particular, further improvements in the engineering of low-cost, robust, sensitive substrates are of utmost importance to further boost the translation of SERS-based analytical tools into competitive, commercially viable applications. In this regard, it is also important to expand the molecular library of surface ligands that can equip the SERS platform with the required properties for a given application (e.g., selectivity, sensitivity, biocompatibility, stability, etc.).

On these bases, the **general objective** of this dissertation is to strengthen the fundamental knowledge about the design and fabrication of advanced plasmonic materials with a special focus on their application as SERS platforms.

The dissertation is organized according to the following **specific objectives**: **(i)** gain a better understanding of the role of different parameters in enabling the formation of well-defined bimetallic structures via the cold-welding process of silver nanoparticles onto gold substrates; **(ii)** design and application of a novel plasmonic/azobenzene sensing platform in the SERS detection of clinically relevant low molecular weight thiols; and **(iii)** fabrication of a graded-index (GRIN) lens metallic metamaterial via self-assembling of SERS-encoded gold nanoparticles of different sizes onto a micrometric silica spherical core.

Accordingly, the dissertation will comprise four chapters:

Chapter 1 provides a basic theoretical background for understanding the key features of (i) plasmonic materials and their unique optical response and (ii) surface-enhanced Raman scattering (SERS) spectroscopy. Then, the rationale for using colloidal Au and Ag nanoparticles as SERS substrates is outlined, with special emphasis on the role of structural parameters (size, shape, composition, and geometrical organization) in determining the overall enhancing properties of the nanomaterial. In the latter part of the chapter, different methodologies for the application of SERS spectroscopy as a sensing tool are discussed. A brief introduction of the use of silver and gold as building blocks in the production of metamaterials with exotic optical properties is also provided.

Chapter 2 reports an extensive study on the cold nanowelding process of metallic nanoparticles with increasing diameters assembled onto gold nanostructures that possess diverse geometrical features. The research aims to obtain a better understanding of the role of different variables involved in the formation of well-defined bimetallic structures that retain the original gold substrate morphology (e.g., silver nanoparticles diameter, gold substrate dimensions and geometries, solvent polarity, and structural nature of the polymeric coating). To this end, a wide range of optical and microscopy techniques have been employed to provide a detailed description of the nanowelding process.

Chapter 3 illustrates a novel approach for engineering a highly efficient, low-cost platform for the SERS sensing of low molecular weight thiols (biothiols). Biothiols are highly active substances extensively involved in human physiology and their abnormal levels have been associated with various diseases. For their detection, colloidally stable silver nanoparticle clusters equipped with a specifically designed azobenzene derivative (AzoProbe) as a SERS chemosensor were generated.

Chapter 4 describes the experimental protocol for fabricating a highly hierarchized metamaterial comprising a silica core covered by a total of 32 layers of densely packed gold nanoparticles of different sizes. Such a complex material experimentally reproduces the optical behaviour of a theoretically calculated graded-index (GRIN) lens.

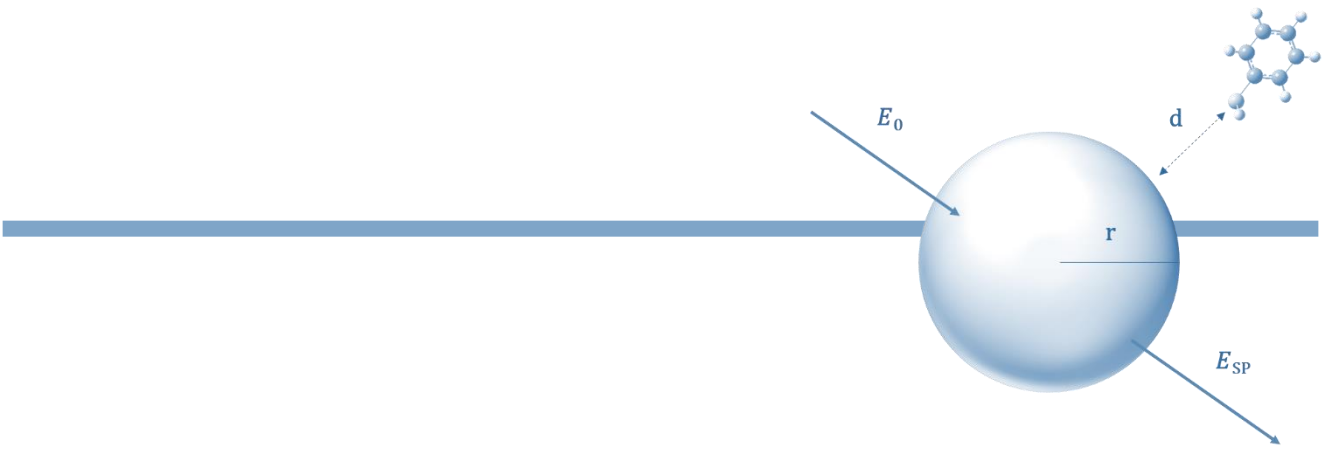

Chapter 1

General Introduction

1.1 NANOTECHNOLOGY

Nanotechnology is a 21st-century science focused on the study of matter at the nanoscale. At such nanoscopic scale, unique phenomena occur enabling novel applications across all science fields,[1] such as chemistry,[2] biology,[3] physics,[4] materials science,[5] and engineering.[6]

The general idea behind nanotechnology was introduced by physicist Richard Feynman in a talk entitled *"There's Plenty of Room at the Bottom"* conferred in California in 1959. In his visionary talk, Feynman predicted the possibility to manipulate matter at the atomic level.[7] Over a decade later, exactly in 1974, Professor Norio Taniguchi coined the term *nanotechnology* in his talk *"On the basic concept of Nano-technology"*.[8] In 1986, as a consequence of the publication of the book *"Engines of Creation: The Coming Era of Nanotechnology"* by the American engineer Erik Drexler,[9] the term starts to be popular. The nanotechnology topic attracted growing interest among the scientific community consolidating a new research area from that moment on.

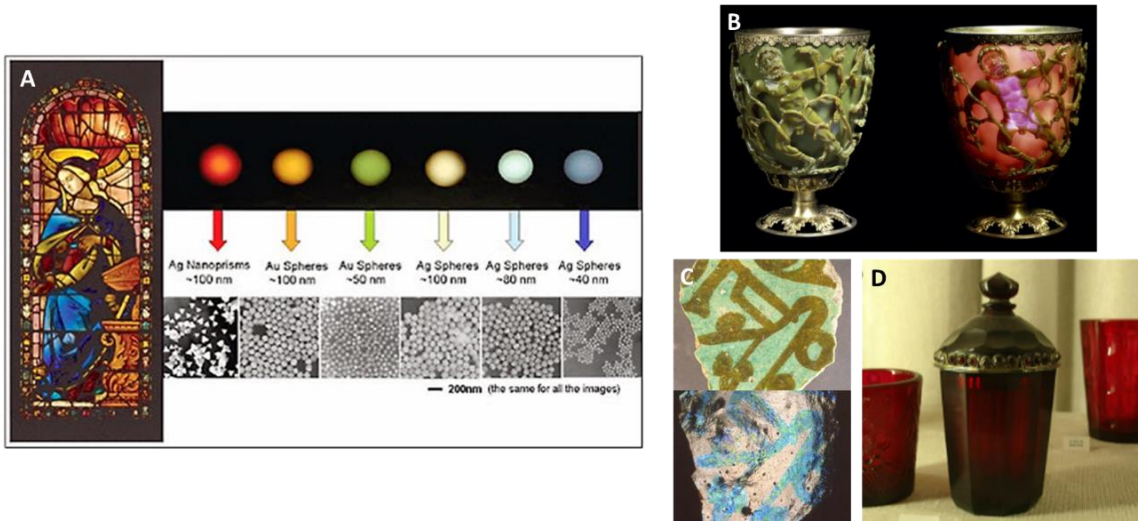

Figure 1.1 (A) Stained glass window with nanoparticles of different sizes to achieve different colors.[10] (B) *Lycurgus Cup* in reflected (left) and in transmitted (right) light, (C) medieval glazed ceramic observed by scattered light and specular reflection, (D) becker made with Purple of Cassius pigment. Adapted with permission from ref. [10] and [11].

However, it is possible to find early examples of nanomaterials more than 4500 years BC. Egyptians and later Romans used particles of lead to produce tints for decorative purposes.[12] Also, the use of metallic nanoparticles, such as gold and silver, dates back to the 14th BC with the Egyptian fabrication of glass. The use of metals was then extended for centuries. For example,

in the Medieval Age, windows of the churches were decorated with metallic nanoparticles showing different colors according to the distribution of size and shape (Figure 1.1A, C).[10, 11] The most famous example of ancient metallic nanoparticles is a Roman glass workpiece called the *Lycurgus Cup* (Figure 1.1B) in which the dichroic glass is made of an alloy of gold and silver. The cup displays green color when light is reflected or red if it is transmitted.[11, 13] After the Romans, the employment of particles was forgotten to be then rediscovered in the seventeenth century and used to produce colors such as the *Purple of Cassius pigment* (Figure 1.1D).[11]

Nowadays is not possible to find a common definition of nanotechnology and the most important world organizations, such as the US Food and Drug Administration (USFDA), the International Organization for Standardization (ISO), and the British Standards Institution (BSI), developed their own. In Europe, the European Commission established that a nanomaterial can be defined as (Figure 1.2):

"A natural, incidental or manufactured material containing particles, in an unbound state or as an aggregate or as an agglomerate and where, for 50 % or more of the particles in the number size distribution, one or more external dimensions is in the size range 1 nm - 100 nm".

[Recommendation 2011 (2011/696/EU)].

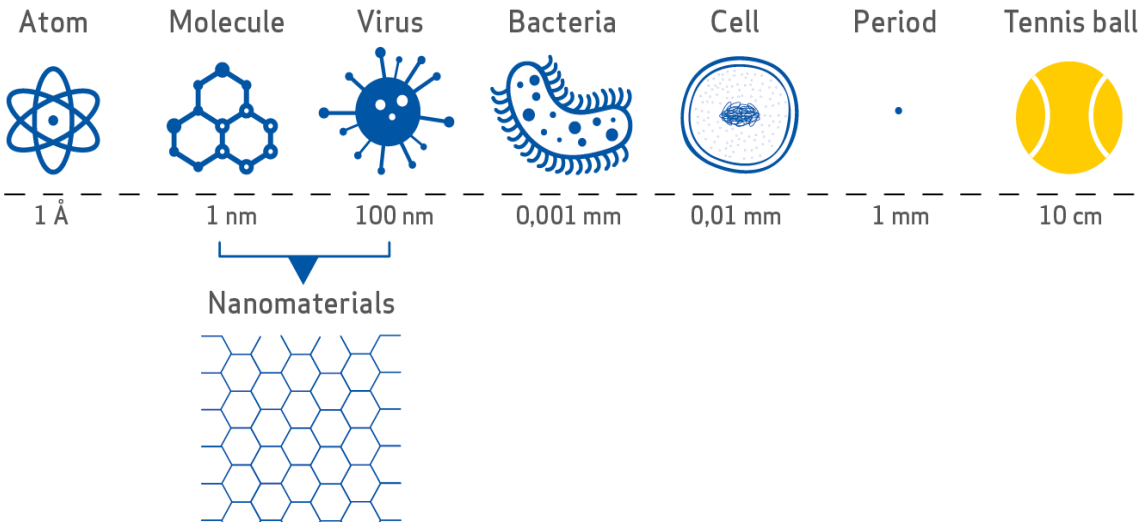

Figure 1.2. Schematic representation of materials at the nanoscale in comparison with macro objects. To be considered nanomaterials the size must range from approximately 1 to 100 nm. *Copyright* **2016***, European Chemicals Agency*.

Due to their nanoscale size, nanomaterials show exceptional chemical, physical, and electrical properties with enhanced performances as compared to their bulk counterpart. Indeed, the surface-area-to-volume (S/V) ratio for a general material has a significant effect on

its properties (Figure 1.3). In the case of nanomaterials, extremely high S/V values cause an increase in chemical reactivity. Moreover, at the nanoscale, quantum effects become relevant altering electrical, magnetic, and optical properties. Most remarkably, the ability of metal nanoparticles to absorb and concentrate the incident electromagnetic field at the nanostructure has been used in a variety of applications, including those based on the so-called plasmon-enhanced spectroscopies such as surface-enhanced Raman scattering (SERS) spectroscopy.[14]

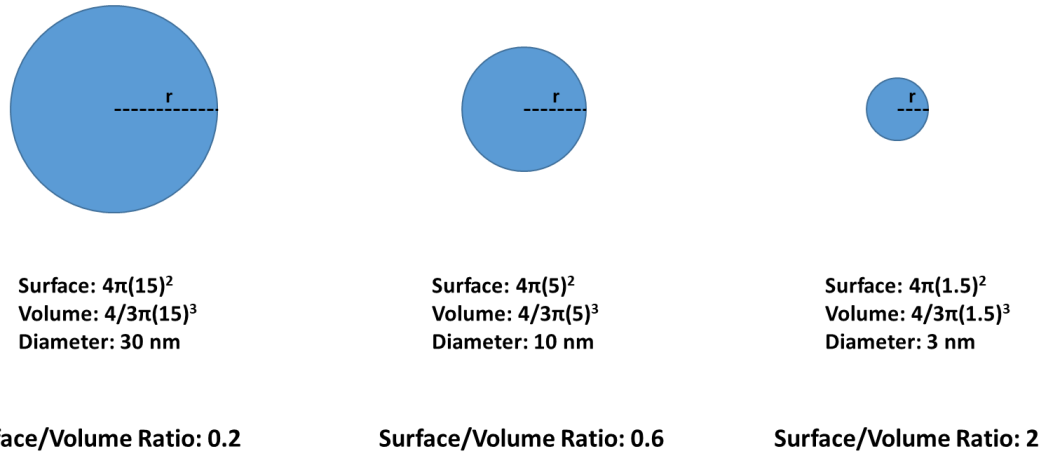

Figure 1.3. Representation of the surface-to-volume ratio for decreasing size nanoparticles.

1.2 RAMAN SPECTROSCOPY

Raman spectroscopy is a spectroscopic technique that employs inelastically scattered light to measure the vibrational energy modes of a molecule. When a monochromatic incident light interacts with molecules, the incoming photons may be absorbed or scattered. Absorption typically occurs when the energy of the incident photon corresponds to the molecule energy gap between the ground state and the excited one (electronic or vibrational). In this case, the molecule is promoted to a higher energy excited state. Alternatively, incident photons can be scattered, which is a physical process that consists of the simultaneous absorption of an incident photon and emission of another photon.[15] For the sake of understanding, the scattering process can be exemplified by imagining the existence of a virtual state (Figure 1.4). In this approximation, light interacting with molecules distorts the electron cloud generating an induced dipole which leads molecules to a virtual state. This state is not stable and the photon is immediately re-radiated as the scattered photon.[15, 16]

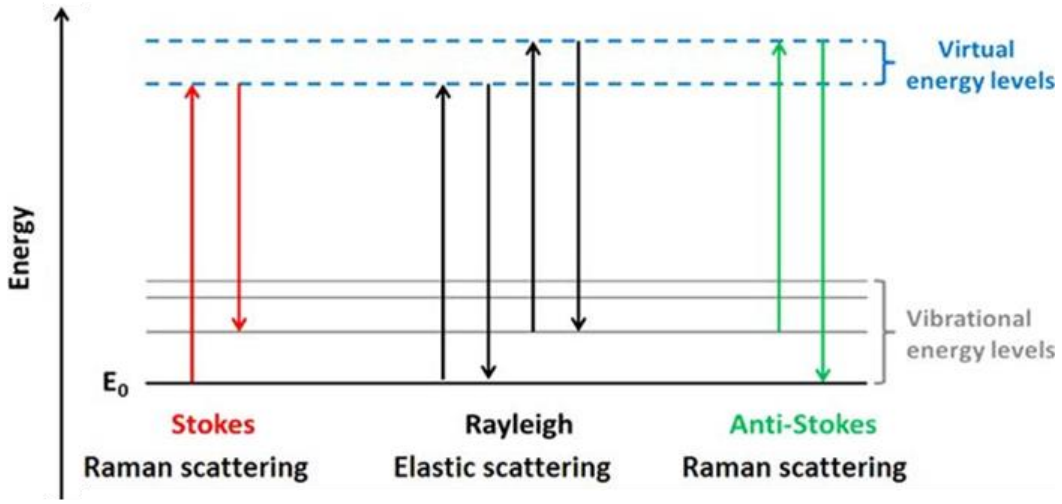

Figure 1.4. Jablonski diagram of energetic transitions involved in Raman scattering.

Most photons are elastically scattered in a process called *Rayleigh scattering* (Figure 1.4). Here, a photon impinges a molecule and polarizes the electron cloud promoting it from the ground vibrational state to the virtual energy state. When the molecule relaxes, the photon is released with the same frequency as the incident light (v_0). On the other hand, a small fraction of the incident photons is scattered at different energies than the incident ones constituting the so-called *inelastic scattering*. This energy change corresponds to an accompanying transition between two vibrational states in the molecule. The scattered photon can either have less energy than the incident one (Stokes scattering) or higher energy (anti-Stokes scattering). Stokes process typically involves the excitation from the ground state (v_0) to the first higher energy

state (v_1). Viceversa, in the anti-Stokes scattering, the molecule commonly relaxes from v_1 to v_0 (Figure 1.4).[17] In typical conditions (e.g., room temperature), the anti-Stokes process is much weaker than the Stokes scattering. This depends on the fact that only a small fraction of molecules populates the v_1 level, as described by the Boltzmann distribution (equation 1.1).

$$N_i \propto e^{-\left(\frac{E_i}{k_B T}\right)} \tag{1.1}$$

where N_i is the probability that molecules' population be in state i, E_i is the energy associated with the state i, k_B is Boltzmann's constant, and T is the temperature.

It is worth noting that large intensifications of the Raman signals can occur when the virtual state coincides with a real electronic state of the molecule (Resonance Raman, RR). In this resonant condition, molecules such as dyes with electronic energies close to the exciting laser energy have been shown to yield Raman intensities several orders of magnitude larger than non-resonant Raman ones.

The collection of the inelastically scattered photons constitutes the Raman spectrum which provides a vibrational fingerprint of the investigated molecule.[18] To represent Raman spectra, Raman intensity is expressed as a function of the wavenumber ($\tilde{\nu}$). The latter is related to energy gain or loss by photons and is defined by Planck's equations (equation 1.2):

$$\Delta E = E_L - E_S = h\nu = hc\tilde{\nu} \tag{1.2}$$

in which E_L represents the energy of the incident photon, E_S is the energy of the scattered photon, h is the Planck constant, ν is the frequency and c is the speed of light. The energy lost/acquired by the photons in the scattering event is called the Raman shift which is positive for Stokes and negative for anti-Stokes scattering. Thus, Stokes and anti-Stokes scattering appear in the Raman spectra shifted in opposite directions from the zero value assigned to the Rayleigh scattering (Figure 1.5).[19]

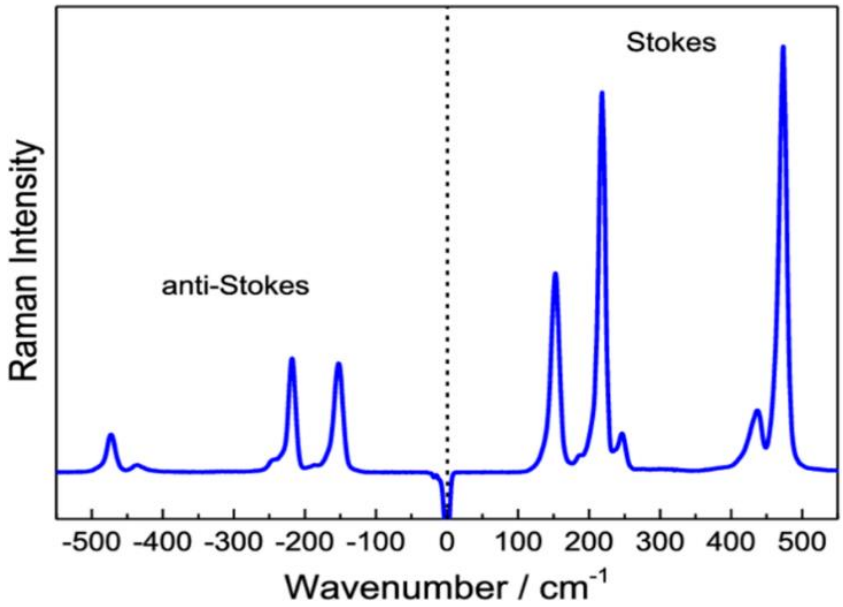

Figure 1.5. Typical Raman spectrum in which Raman intensity is a function of the Raman shift. Stokes scattering and the weaker anti-Stokes counterpart are symmetrical to Rayleigh scattering (zero shift). Adapted with permission from ref. [19]

The Raman shift of the peaks constituting the Raman spectrum corresponds to the vibrational energy gap related to the specific vibrational mode. However, not all of these vibrational modes are susceptible to scattering light but are subject to specific *selection rules* which are related to the polarizability of the molecule.[20] Polarizability is a property that measures the ease of distorting the electrons cloud of a molecule from their original position under an applied external electric field. For a vibrational transition to be Raman active, the molecule must change polarizability during the vibration (Figure 1.6). In this case, the interaction leads to the generation of an induced dipole p_R (Raman dipole) oscillating at a frequency $\omega_R = \omega_L - \omega_v$ which differs from the incident field frequency (ω_L) because of the modulation determined by the vibration frequency (ω_v). Thus, the Raman dipole can be described as:[21]

$$p_R(\omega_R)=\alpha_R(\omega_L, \omega_V)\, E(\omega_L) \qquad (1.3)$$

where $\alpha_R(\omega_L, \omega_v)$ is the Raman polarizability tensor for a specific vibrational mode.

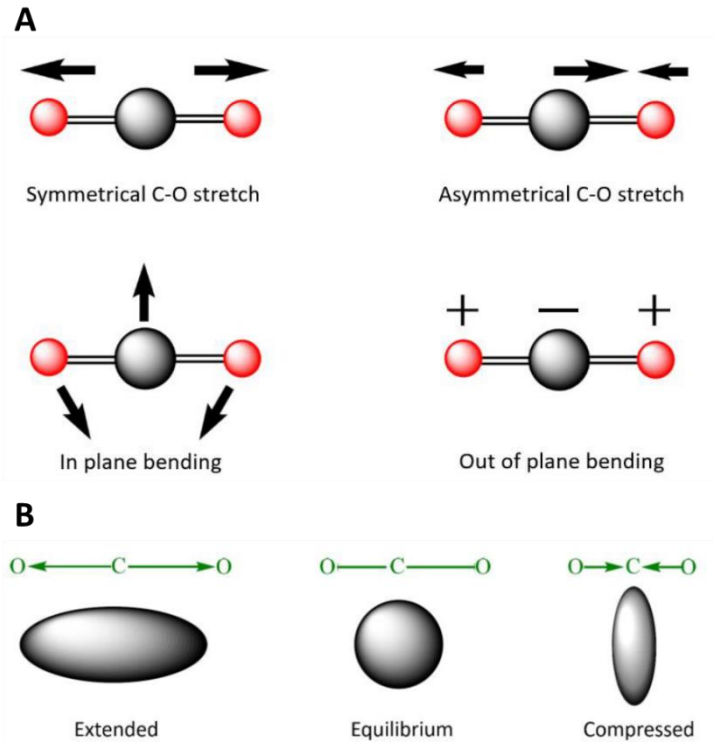

Figure 1.6. (A) Representation of CO_2 vibrational modes. (B) Electron cloud distortion in C-O symmetrical stretch of CO_2 that results in Raman active mode.

The efficiency of the Raman scattering process for a specific vibrational mode (i.e., the ability to convert incident photons into scattered ones) can be described in terms of Raman cross-section (σ_{RS}) according to the following equation:

$$I_{RS} = \sigma_{RS} I_0 \tag{1.4}$$

where I_0 is the incident power density [W m^{-2}] at the molecule position and I_{RS} is the total inelastically scattered power [W].[22] Thus, σ_{RS} [m^2] can be viewed as the area of a homogeneous incoming beam from which the molecule will absorb every photon.[23] The Raman cross-section is referred to a randomly orientated molecule and depends on several parameters, most importantly the wavelength of the excitation source ω_L (σ_{RS} is proportional to ω_L^4) and the refractive index of the medium in which the molecule is immersed.

The experimental flexibility and structural specificity of Raman spectroscopy made this technique a universal tool exploited in a wide range of applications.[24, 25, 26, 27] However, except for specific conditions (Resonance Raman), the intrinsic inefficiency of the Raman process

hampers the application of conventional Raman spectroscopy to the investigation of materials at low concentrations.

1.3 PLASMONICS AND SURFACE-ENHANCED RAMAN SCATTERING (SERS) SPECTROSCOPY

1.3.1 The optical properties of noble metallic nanoparticles: the localized surface plasmon resonances

The unique optical properties, as well as large heat or electrical conductivity, of metals such as gold (Au), silver (Ag), or copper (Cu), originate from the presence of free conduction electrons. To a first approximation, such free-electron plasma moves in a background of fixed positive ions. The action of an external electric field (e.g., incident light) causes the conduction electrons to oscillate coherently as the free-electron plasma cloud is displaced relative to its original position and then pull back by a restoring force associated with the coulombic attraction between electrons and nuclei (Figure 1.7). The optical response of this free-electron plasma largely defines the overall optical properties of the metals, at least in the visible part of the spectrum where the characteristic resonant energies reside.[28]

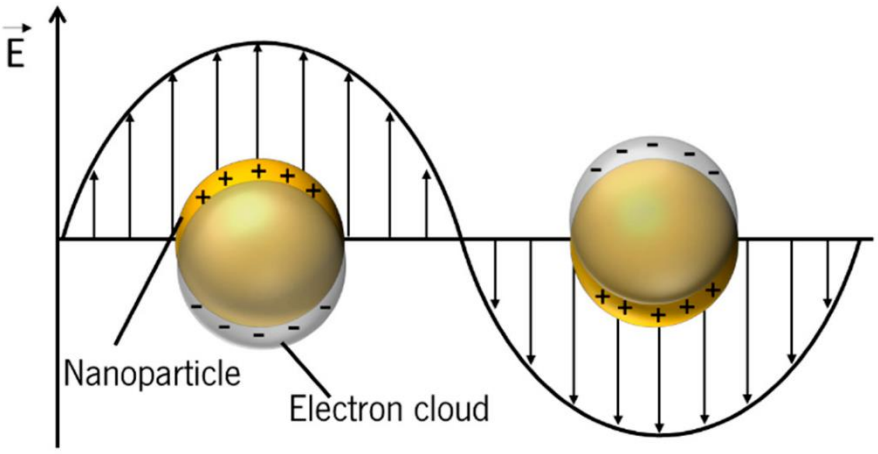

Figure 1.7. Schematic representation of localized surface plasmon resonance (LSPR) in nanospheres. Adapted with permission from ref. [29].

Contrarily, in dielectrics, electrons are bound to atoms thus they are not free to move. Then, electrons will be polarised under an applied field and the induced electromagnetic field will be represented by the sum of the response given by each atom rather (Figure 1.8).[30]

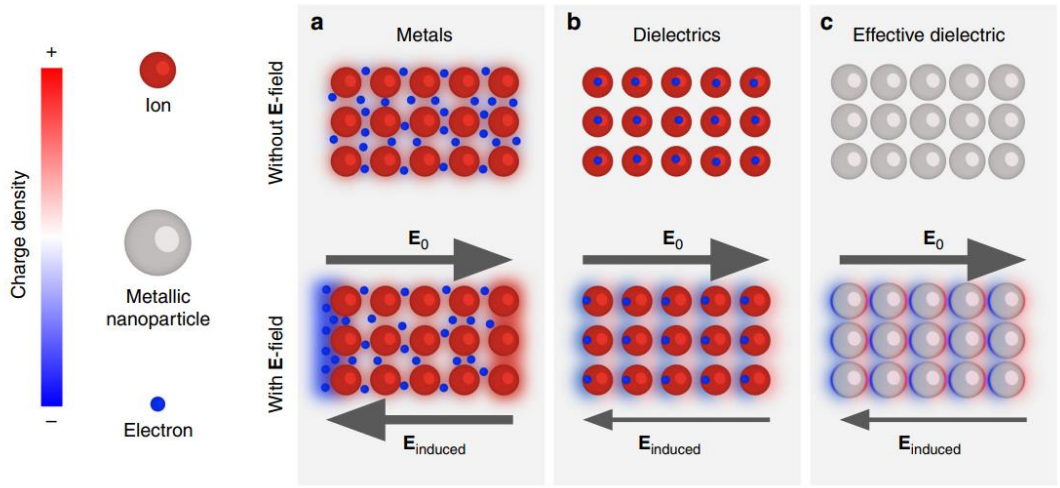

Figure 1.8. Illustration of metals, dielectrics, and effective dielectrics response to a slowly varying electric field. Figure from ref. [30]

An important parameter that must be considered in the understanding of the interaction between light and metals is the dielectric function $[(\omega)]$ which describes the dielectric response to the incident electric field. In fact, the characteristic frequency of the free-plasma oscillation can be related to the metal-dielectric function. This parameter depends on the incident electromagnetic frequency (ω). In the most common materials, the dielectric function is a positive real number but in the case of metals that are not able to transmit light, this parameter is a complex number and can be represented as follow (equation 1.5):[28, 31, 32]

$$[\varepsilon(\omega)=\varepsilon'(\omega)+\varepsilon''(\omega)\, i] \tag{1.5}$$

where $[\varepsilon'(\omega)]$ is the real part and $[\varepsilon''(\omega)\, i]$ is the imaginary one.

The simplest way to model the optical response of a free-electron plasma is the Drude model [33, 34] which provides a simple framework to understand electrical conductivity. This model is based on the Lorentz model for atomic polarizability. The latter describes the optical response of an electron in an atom or molecule, bound and with a restoring force having a resonant frequency ω_0. Since in a metal conduction electrons are not bound, they can be defined by the Lorentz model without a restoring force ($\omega_0 \approx 0$). Furthermore, because the free electrons are distributed uniformly and randomly in the metal, their contribution to the total optical properties is represented by the sum of their individual polarizabilities, without any local field correction.

The Drude relative dielectric function $\varepsilon(\omega)$ of a metal is expressed by the equation 1.6:[35]

$$\varepsilon(\omega)=\varepsilon_{\infty}\left(1-\frac{\omega^{2}_{p}}{\omega^{2}+i\Upsilon_{0}\omega}\right) \quad (1.6)$$

where ω_p [rad s^{-1}] is the plasma frequency (i.e., the natural oscillation frequency of the free-electron plasma). Without an external perturbation, the charge density of plasma is uniform and zero. The damping term, Υ_0 [rad s^{-1}], corresponds to the collision rate of free electrons with the positive core represented by the term ε_{∞}. Thus, the model assumes that plasma frequency depends on the free electrons interactions among themselves and their collisions with the positive crystal.[35] Considering the real and imaginary parts of the previous equation, it is possible to write:

$$\mathrm{Re}(\varepsilon(\omega))=\varepsilon_{\infty}\left(1-\frac{\omega^{2}_{p}}{\omega^{2}+\Upsilon^{2}_{0}}\right) \quad (1.7)$$

$$\mathrm{Im}(\varepsilon(\omega))=\frac{\varepsilon_{\infty}\omega^{2}_{p}\Upsilon_{0}}{\omega(\omega^{2}+\Upsilon^{2}_{0})} \quad (1.8)$$

The collision rate Υ_0 is a small contribution in comparison to ω, thus the plasma frequency can be obtained. In the region where $\omega < \omega_p$, $\mathrm{Re}(\varepsilon(\omega_p)) < 0$. Additionally, when ω is not too small, the absorption characterized by $\mathrm{Im}(\varepsilon(\omega))$, will be also small in this region. These two conditions, a large negative real part and a small positive imaginary part, make possible interesting optical properties such as plasmon resonances.

Notably, when the particle size is smaller than the incident wavelength, the plasmon resonance remains confined at the surface (i.e., localized surface plasmon resonance, LSPR) causing a large enhancement of the local field inside the metal and, more importantly, on the outside surface.[36]

Let's thus consider the simple case of a small metallic sphere of radius *a* embedded in a non-absorbing dielectric medium of dielectric constant ε_M and interacting with an electromagnetic field (in a laser beam of wavelength much larger than the sphere). In this case, the (complex) electric field inside the sphere $\mathrm{E_{In}}$ is proportional to the incident field $\mathrm{E_0}$ and can be described as:[37]

$$\mathrm{E_{In}}=\frac{3\varepsilon_{M}}{\varepsilon(\omega)+2\varepsilon_{M}}\mathrm{E_0} \quad (1.9)$$

The electric field is therefore constant and uniform inside.

The incident field E_0 induces a polarization in the metallic sphere yielding an induced dipole:

$$\mathbf{p_M} = \alpha_S \mathbf{E_0} \tag{1.10}$$

where α_S is the polarizability of the sphere, which is proportional to:

$$\alpha_S \propto a^3 \frac{\varepsilon(\omega) - \varepsilon_M}{\varepsilon(\omega) + 2\varepsilon_M} \tag{1.11}$$

This induced dipole creates, in turn, an electrostatic field E_{pM} (the scattered field) outside the sphere which adds up to the incident field E_0 to yield the electric field outside the sphere, E_{out}:[38]

$$\mathbf{E_{out}} = \mathbf{E_0} + \mathbf{E_{pM}} \tag{1.12}$$

Based on this approximation (dipolar approximation), E_{out} is maximized at a frequency where $\varepsilon(\omega) + 2\varepsilon_M = 0$ which means, taking into account the complex nature of the dielectric constant, when $\mathrm{Re}(\varepsilon(\omega)) \approx -2\varepsilon_M$ and $\mathrm{Im}(\varepsilon(\omega))$ is small. In this scenario (resonance condition) the optical response (absorption and scattering) is then very large, which is the signature of a LSPR.

It is important to note that the electric field outside the sphere decays as $1/(a+d)^{12}$ when one progressively moves further from the metallic surface at a distance *d*. This means that E_{out} is maximum for $d = 0$ and rapidly decreases until approximately 10 nm distance. Such a distance dependency of the electromagnetic field generated at the metallic surface has a major impact on defining the intrinsic nature of SERS spectroscopy, which can then be mostly viewed as a first-layer effect (i.e., SERS signals can be obtained, by and large, only from those molecules adsorbed onto or located close to the plasmonic substrate).[39, 40]

As pointed out, the occurrence of a LSPR is then primarily determined by the real part of the dielectric function whereas the imaginary part defines how large such resonance can be. Thus, we can qualitatively infer that good metals for plasmonics should display, in the wavelength range of interest for Raman (typically from the visible to the near-infrared), negative $\mathrm{Re}(\varepsilon(\omega))$ and small $\mathrm{Im}(\varepsilon(\omega))$ values. Figure 1.9 illustrates the real and imaginary parts of the

dielectric function of various metals, showing the characteristic monotonous decay of Re(ε) from small values in the UV to negative values in the visible, and very negative values in the infrared, for all metals.[37] Based on the previous considerations, silver and lithium are, in principle, promising plasmonic materials. However, lithium high reactivity makes not practical its use in the fabrication of nanostructures. On the other hand, gold and copper exhibit suitable optical properties at longer wavelengths (>600 nm) where the Im($\varepsilon(\omega)$) part becomes sufficiently small to prevent extensive damping of the LSPRs. The damping at shorter wavelengths can be ascribed to the presence of other relevant optical processes besides the oscillations of free electrons in the conduction band such as inter-band transitions (i.e., bound electrons optically excited to a higher energy band). In the case of silver, such contributions only become relevant in the UV spectral range.[37]

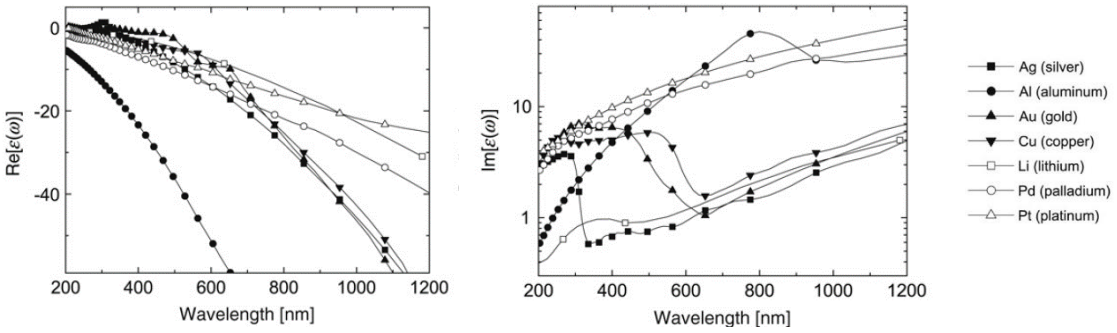

Figure 1.9. Real and imaginary parts of ε as a function of wavelength for a selection of metals. Figure from ref. [37].

By combining the intrinsic optical response of metals with other practical issues such as availability, ease of manipulation, reactivity, toxicity, durability, and cost, is possible to justify why silver and gold are by far the most widely employed materials in the fabrication of plasmonic nanostructures, including for SERS applications.[41] Overall, Ag constitutes a much more efficient plasmonic material than gold in the visible region (only for $\lambda > 600$ nm, the Au and Ag imaginary parts become comparable, Figure 1.9).[8, 32, 42] On the other hand, gold nanomaterials are more chemically inert (Au is typically less susceptible to oxidation than Ag)[43] while simultaneously allowing for better control over the final size and shape of the nanostructures.[44]

1.3.2 SERS enhancement

In the previous section, the concepts of LSPRs have been introduced, leading to a qualitative description of the origins of the large local field enhancements that are localized at the metallic surfaces. Notably, molecules immersed in such intensified local fields can

experience a dramatic boost in their Raman scattering intensity. This mechanism of intensification, which applies regardless of the nature of the molecule, is called electromagnetic (EM) enhancement and represents the *sine qua non* condition to observe SERS. On the other hand, the direct contact of the metallic nanostructure with the molecular scatterer can further modify its Raman response by altering the Raman polarizability of the molecule via chemical mechanisms (Chemical Enhancement, CE), which contribute in a multiplicative fashion to the final SERS enhancement. Different from EM enhancements, CE is strictly related to the specific chemical nature of the adsorbate.[45, 46]

Electromagnetic mechanism (EM)

The amplification of the Raman scattering from molecules located in close proximity of the metallic surface via LSPR excitations using a source of light of appropriate wavelength (λ_L) can be approximated as the result of two multiplicative events: the enhancement of the local incident field *on* the analyte and the enhancement of the re-emitted Raman scattering *from* the analyte (Figure 1.10A).[47]

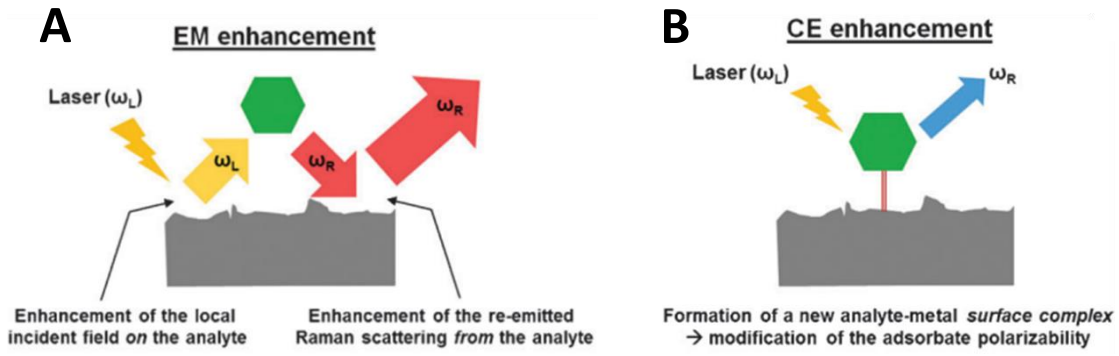

Figure 1.10. Schematic illustration of (A) electromagnetic and (B) chemical enhancement mechanisms in SERS. Adapted with permission from ref. [47].

The local field E_{Loc} felt by the molecule at a specific position induces the following Raman dipole:

$$p_R = \alpha_R E_{Loc}(\omega_L) \tag{1.13}$$

whose magnitude is amplified as compared to the Raman dipole induced by the incident electric field E_0 by a factor of $E_{Loc}(\omega_L)/E_0$. For a dipole radiating in free space (no metal), the energy radiated is proportional to $|p_R|^2$. Thus, the local field intensity enhancement factor associated with the excitation of the Raman dipole can be defined as:[48]

$$M_{Loc}(\omega_L) = \frac{|E_{Loc}(\omega_L)|^2}{|E_0|^2} \quad (1.14)$$

However, the Raman dipole does radiate in proximity to the plasmonic nanomaterial which, in turn, modifies the spontaneous emission by altering the radiation pattern (i.e., the power radiated in a given direction) as well as the total power radiated by the dipole (P_{Rad}). P_{Rad} can be enhanced or quenched as compared to that of the same dipole oscillating in free space (P_0). Thus, the radiation enhancement factor can be defined as $M_{Rad} = P_{Rad} / P_0$.

Therefore, the overall electromagnetic enhancement felt by a single molecule (single molecule-enhancement factor, SM-EF) at a specific point of space can be expressed as the multiplicative contribution of the local field enhancement (excitation) and radiation enhancement (re-emission):[49]

$$\text{SM-EF}(\omega_L, \omega_R) \approx M_{Loc}(\omega_L) \times M^d_{Rad}(\omega_R) \quad (1.15)$$

Here, the radiation enhancement factor M^d_{Rad} is referred to the direction *d* of the detection of the SERS signal (i.e., directional radiation enhancement factor). While M_{Loc} can be calculated by solving the electromagnetic problem for given excitation conditions, estimating M_{Rad} represents a more complicated task. However, since both local field and radiation enhancements share the same physical origin, the resonances should at least be qualitatively similar for both mechanisms which, in turn, justifies the $M^d_{Rad}(\omega_R) \approx M_{Loc}(\omega)$ approximation. This means that the EM enhancement can be then expressed simply as:[49]

$$\text{SM-EF}(\omega_L, \omega_R) \approx M_{Loc}(\omega_L) M_{Loc}(\omega_R) \approx \frac{|E_{Loc}(\omega_L)|^2}{|E_{Inc}|^2} \frac{|E_{Loc}(\omega_R)|^2}{|E_{Inc}|^2} \quad (1.16)$$

Moreover, for small Raman shifts (i.e., $\omega_R \approx \omega_L$), this expression can be further simplified to the well-known $|E|^4$-approximation:[49]

$$\text{SM-EF}(\omega_L) \approx \frac{|E_{Loc}(\omega_L)|^4}{|E_{Inc}|^4} \quad (1.17)$$

In many cases, this approximation is sufficient to obtain SM-EF with the correct order of magnitude. Average SERS EFs can also be derived within this approximation by surface averaging the individual single-molecule EFs. On the other hand, by somehow omitting the radiation enhancement, the $|E|^4$-approximation fails to detail other facets of the SERS process, such as the *surface selection rules*. While these additional factors have only a marginal influence on the overall magnitude of the single-molecule EF, they account for changes in the relative intensities of Raman peaks of different symmetries for a given molecule orientation onto the metal surface.[50]

Chemical enhancement (CE)

Although the EM enhancement is the major contributor to the SERS effect, reaching values as high as 10^{10}-10^{11}, additional modulations of the SERS signal can also originate from the change in the Raman polarizability, α_R, of the analyte upon interaction with the metal. Indeed, the chemical bonding of the molecule to the plasmonic surface yields a new analyte-metal surface complex (Figure 1.10B). Major changes in the electronic distribution in the molecule can result in the formation of new electronic states that are in resonance, or close to, with the excitation wavelength leading to the enhancement of the Raman scattering analogous to the resonant Raman type (Figure 1.11A). Alternatively, the excitation wavelength can also induce resonant charge transfer (CT) processes between the molecule and metal (Figure 1.11B). These CT transitions occur between the Fermi level of the metal nanostructure and the molecular orbitals of the adsorbed molecule: HOMO (highest unoccupied molecular orbital) or LUMO (lowest unoccupied molecular orbital) (see Figure 1.11B).[51] Typically, CE provides increases the overall enhancement up to two/three orders of magnitude.[47]

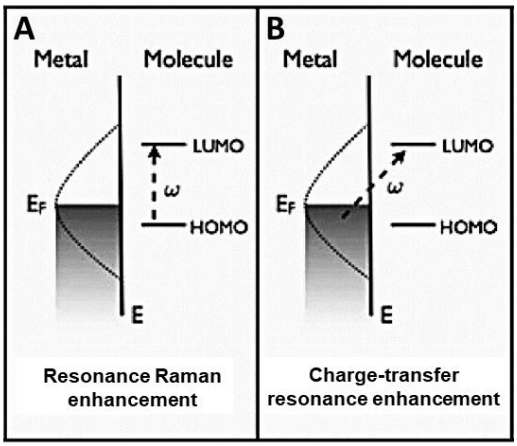

Figure 1.11. Representation of different contributions involved in CE mechanism. Adapted with permission from ref. [52].

Experimental measurement of the SERS enhancement factor (EF)

Experimentally, the SERS enhancement is typically calculated as the average EF for a given SERS substrate under specific conditions (e.g., laser excitation wavelength, detection set-up, etc.) according to the following equation:

$$EF_{SERS} = \frac{I_S N_R}{I_R N_S} \quad (1.18)$$

where I_S is the intensity of the SERS signal originating from N_s molecules adsorbed at the metallic surface and within the scattering volume (for SERS measurements), while I_R is the normal Raman intensity arising from the scattering of N_R molecules in the same scattering volume.[51, 53, 54] Accurate estimations of the substrate EF are performed by maintaining the surface coverage below the monolayer and using molecular probes that minimize signal modulations via chemical mechanisms.[55]

The optical intensities can be written in terms of the molecular cross-section, σ_R. Also, a new factor, Γ_R, can be introduced to include some instrumental contributions (e.g., the optical collection solid angle, the spectrometer transmission efficiency, the detector sensitivities, the physical light scattering efficiency). Thus, for normal Raman measurements, the intensity I_R can be expressed as follows:[55, 56]

$$I_R = \Gamma_R \sigma_R N_R |E_0|^2 \quad (1.19)$$

For SERS, equation 1.19 is modified by introducing the factor G which takes into account the electromagnetic enhancement (equation 1.20).[56]

$$I_S = \Gamma_S \sigma_S N_S G |E_0|^2 \quad (1.20)$$

Substituting G into the equation 1.18 yields:

$$EF_{SERS} = \frac{\Gamma_S \sigma_S G}{\Gamma_R \sigma_R} \quad (1.21)$$

If one considers the instrumental factors to be the same in the two experiments ($\Gamma_R \approx \Gamma_S$), then the expression can be simplified to as:

$$\mathbf{EF_{SERS}} \approx \mathbf{G} \times \frac{\sigma_S}{\sigma_R} \tag{1.22}$$

which qualitatively correlates (a) the observed substrate EF with the different natures of the electromagnetic mechanism G, which is solely related to the optical properties of the plasmonic nanomaterial, and (b) the chemical mechanisms that arise from the deviation of the Raman polarizability of the analyte-metal surface complex (σ_S) to that of the molecule in the free-space (σ_R).[56]

1.4 COLLOIDAL NANOPARTICLES AS SERS SUBSTRATES

Plasmonic substrates designed for SERS applications are characterized by nanostructured features of size much smaller than the exciting radiation wavelength, typically in the ca. 10-100 nm range. Excessively small structures support weak plasmon resonances leading to low SERS enhancements, as their optical response starts deviating from the pseudo-bulk-plasmon behavior.[57, 22] On the other hand, as previously discussed, plasmonic resonances are strongly damped for excessively large structures (i.e., energy is lost through scattering).

A huge number of nanostructured materials for SERS have been fabricated with a large variety of methods, which can be arbitrarily grouped into two main classes:

(1) Structured surfaces. They are commonly obtained via lithographic techniques or fabricated by depositing nanoparticles into highly ordered arrays on solid supports.[58, 59]

(2) Individual nanoparticles and their assemblies in suspension. These materials constitute the most widely exploited substrates for SERS which can be often obtained in a variety of sizes, shapes, and architectures via low-cost and facile fabrication methods.

Universal SERS substrates do not exist and the selection or design of them is strictly correlated to the analytical regime of the experiment and the restriction imposed by the given application. For example, for the analysis of a large number of target molecules, the SERS substrate is usually engineered to provide relatively moderate (10^5-10^8) but highly reproducible and uniform enhancements. On the contrary, for the detection of an ultralow rate of target molecules, nanomaterials are designed to produce the highest enhancements (~10^{10}-10^{11}) at specific points of the substrate.[47, 60]

1.4.1 Individual particles: from isolated spherical particles to asymmetric structures

Spherical or spherical-like gold and silver nanoparticle colloids represent the most common type of SERS-active materials, which can be easily and reproducibly synthesized via a chemical reduction in solution.[61] These colloids typically exhibit LSPRs in the 380-420 nm for Ag and 515-560 nm for Au (Figure 1.12A). Here, the larger the nanoparticle diameter, the more red-shifted and broadened the plasmon resonance. Moreover, additional new multipolar resonances (e.g., quadrupole) emerge in the extinction spectra at lower wavelengths, which are especially distinguishable in the case of Ag colloids.[62, 63] Isolated Ag NPs can provide relatively high enhancements (ca. 10^4-10^5)[64] but only for excitation wavelengths close to the LSPR maxima in the unfavorable spectral range close to the UV. On the other hand, strong damping of the

LSPRs for Au occurs in the sub 600 nm range of excitation. Thus, LSPRs of spherical nanoparticles in the visible range are always strongly damped, either because of the large optical absorption (at wavelengths < 600 nm for Au) or due to energy lost via scattering (for Ag and Au).

Differently from the size parameter, controlling the shape of the individual nanoparticles offers a valuable route to fine-tuning the optical properties of the materials and, thus, efficiently boosting the enhancing ability. Indeed, asymmetric nanoparticles exhibit new LSPRs, as the oscillation of the electron cloud can take place along different morphological symmetric axes, which can be tuned in a much wider spectral range as compared to the simple spherical geometry (Figure 1.12B).[65]

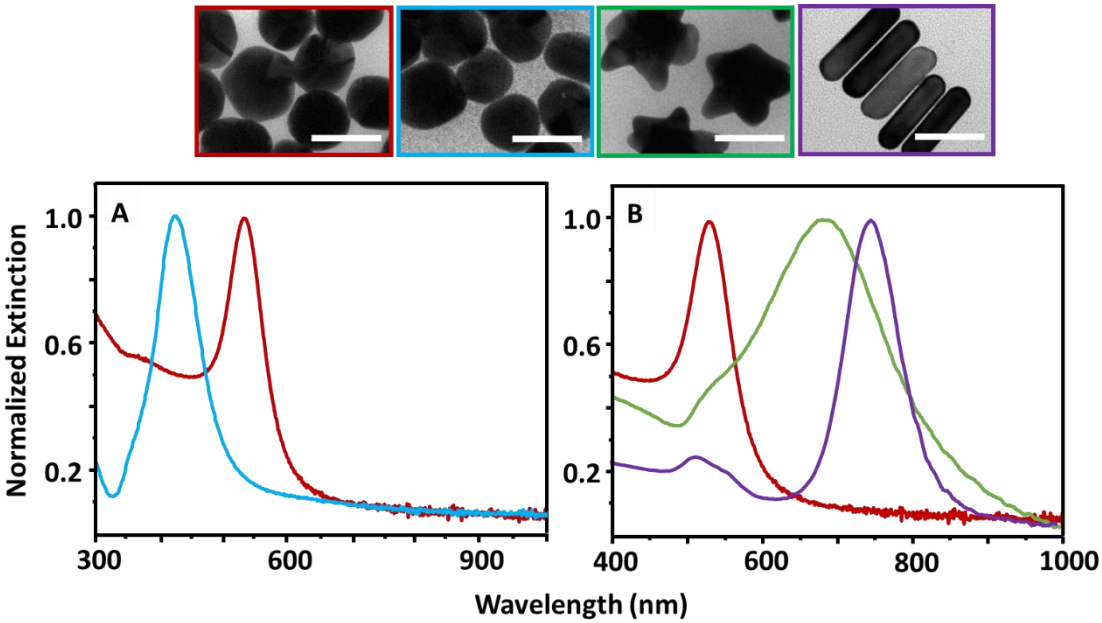

Figure 1.12. Top: TEM images of gold nanoparticles with different morphologies such as spheres (red), stars (green), rods (purple), and silver nanospheres (light blue; scale bar = 50 nm). Bottom: Normalized absorption spectra of (A) gold and silver nanospheres of ca. 50 nm diameter, respectively, and (B) gold nanospheres, nanostars, and nanorods.

In particular, gold nanorods (AuNRs) provide a paradigmatic example of anisotropic nanoparticles by displaying two well-separated plasmonic resonances: a damped blue-shifted one associated with the transversal mode of oscillations of the electron cloud, and an intense red-shifted longitudinal mode (Figure 1.13).[66] The latter contribution is the most important for SERS since it localices the largest EM enhancement at the tips of the rod. These EM enhancements can exceed those located on the single sphere surface by several orders of magnitude.[67] Moreover, in the case of AuNRs, the longitudinal LSPR can be efficiently tuned in a wide range of the near-infrared region by simply varying the NR aspect ratio; that is, beyond the

critical 600 nm threshold where the EM enhancing properties of gold approach that of silver (Figure 1.14). AuNRs of controlled size and aspect ratios are usually synthesized by anisotropic growth of gold nanosphere seeds in the presence of the surfactant cetyl trimethyl-ammonium bromide (CTAB) as a shape-directing agent.[68]

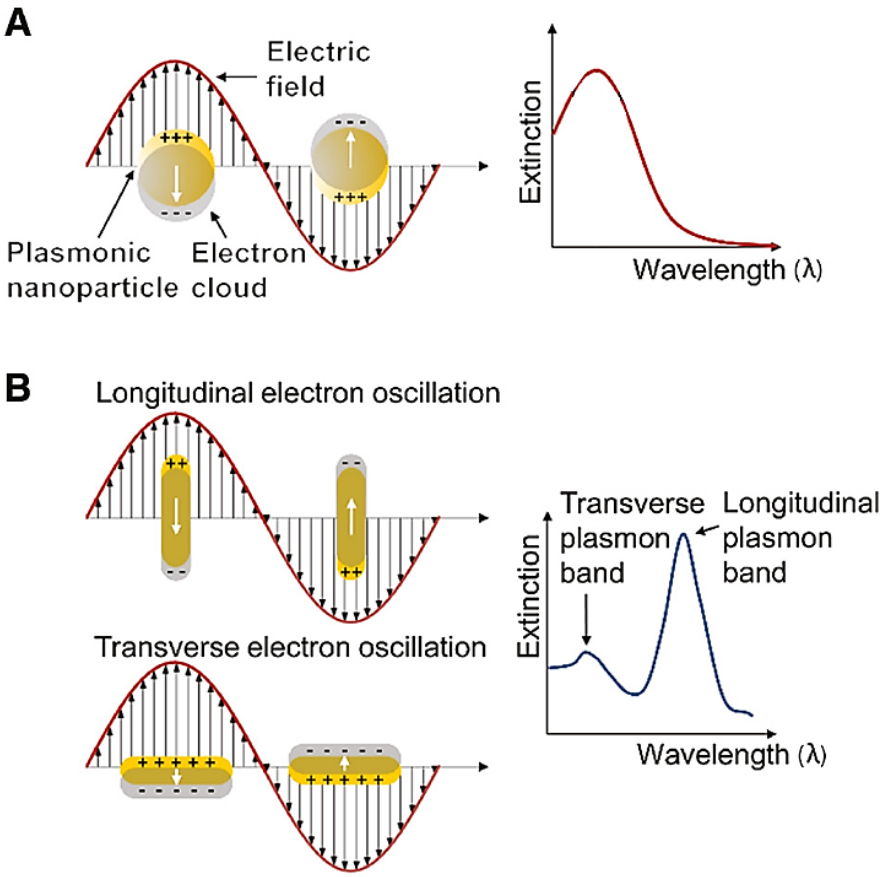

Figure 1.13. Schematic representation of LSPRS in (A) nanospheres and (B) nanorods with corresponding extinction spectra. Adapted with permission from ref. [66]

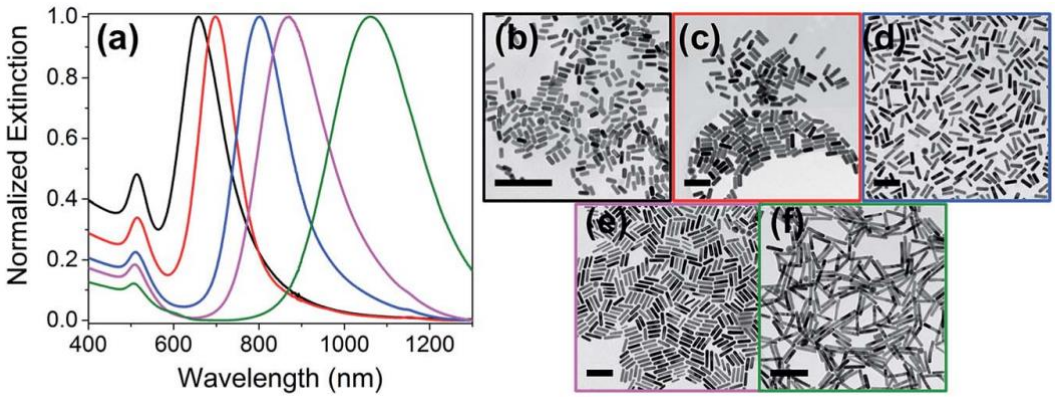

Figure 1.14. (A) Normalized extinction spectra of AuNRs with different aspect ratios and (B-F) corresponding TEM images. Figure from ref. [69]

An additional route to tailor the plasmonic properties of the substrates is represented by the combination of Au and Ag into bimetallic nanomaterials.[70, 71, 72] Several approaches have been developed to the fabrication of such Ag/Au materials, which are mostly based on chemical reductions in solution.[70, 71, 72] Figure 1.15 illustrates an example of a synthetic pathway to obtain a bimetallic structure via a surfactant-mediated seeded-growth approach. In this method, Ag is overgrowth on a Au core to yield Au@Ag cuboids through a three-step mechanism: (1) the formation of micelles surfactant-stabilized Ag^+ ions that diffuse in bulk solution, (2) the transport of ions across the surfactant bilayer deposited on the gold core surface, and (3) the reduction of Ag^+ ions at the metal surface.[72]

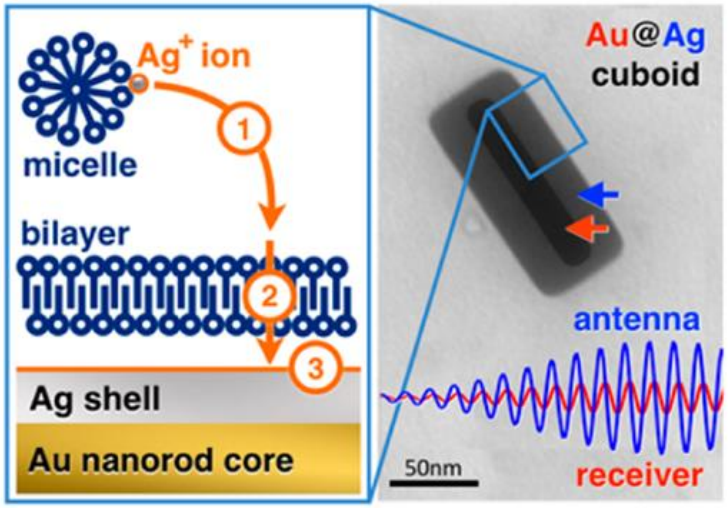

Figure 1.15. Representative sketch of the three-step silver overgrowth mechanism. Adapted with permission from ref. [72]

Methods based on chemical reductions, while being relatively simple and low-cost, do suffer from some limitations. In particular, for a controlled overgrowth on top of another metallic colloidal structure, it is required that the surface free energy of the metal to be reduced must be lower than the metallic colloids otherwise a galvanic replacement will occur instead.[73, 74] The surface free energy of Ag (0.923 Jm^{-2}) is lower than for Au (1.128 Jm^{-2}) [75] and, therefore, a layer of Ag can then be easily grown onto AuNPs by redox reactions.[76, 77] However, such growth is selective for specific crystallographic planes.[78] This implies that the heterogeneous distribution of crystallographic planes on the nanoparticles causes asymmetric growth of the coating metal, which hinders the possibility of retaining the original particle morphology (see for instance the different thickness of the Ag coating on the lateral sides and tips of the AuNR in figure 1.15).[79] On the other hand, it is known that when two metallic NPs come into contact, they spontaneously coalesce. This solid-state process, known as cold-welding, occurs by the

transport of atoms via atomic diffusion and surface relaxation to reduce the surface free energy. Indeed, at the nanoscale, the diffusion barrier for a single metal atom on a clean metal surface is very low (ca. 1.0 eV),[80] thus permitting the nanowelding process to proceed at room temperature.[81, 82] During this process, the fusion of NPs is thermodynamically driven (i.e., spontaneous) and represents a common phenomenon observed in colloidal systems (referred to as Ostwald ripening) in which smaller particles coalesce to form larger ones.[83] Such phenomenon has emerged as an attractive way for bottom-up assembly at the nanoscale.[84, 85, 86, 87, 88] For example, Calderon et al. [88] exploited the controlled Ostwald ripening of small gold nanoparticles on the surfaces of larger silver particles to fabricate colloids composed of a segregated alloy of silver coated with gold (Figure 1.16). The prepared segregated nanoalloys provide optical efficiencies which are superior to those of silver with the chemical resistance and biocompatibility of gold.

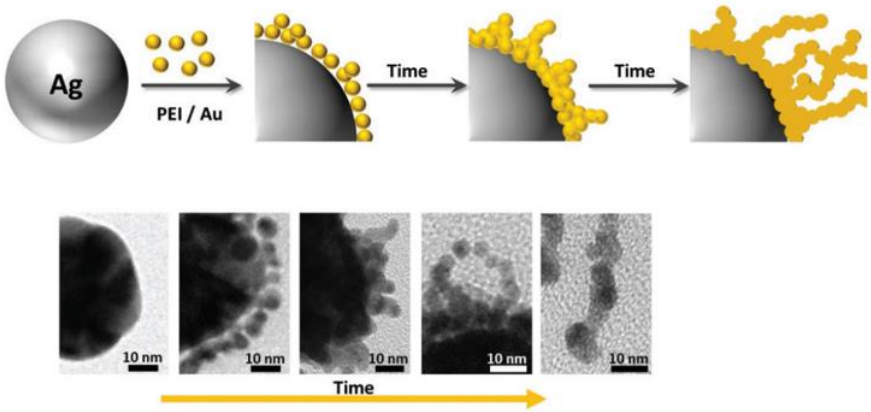

Figure 1.16. Scheme of growth mechanism during the nanowelding process of Au nanoparticles onto Ag core. Adapted with permission from ref. [88].

1.4.2 Interparticle Coupling in Nanoparticles assemblies: generation of hot spots

In addition to the impact of size, shape, and composition of single nanoobjects onto the plasmon resonances, extremely relevant phenomena for SERS arise when two individual nanoparticles are brought in close contact with each other. In the simplest case of a dimer formed by two identical spheres, the electromagnetic interaction (plasmon coupling) between the two objects causes a major change in the extinction profile of the spheres (Figure 1.17, black curve) which now exhibit two well-separated features (Figure 1.17, red curve), as similarly observed for gold nanorods. When the polarization of the incident beam is perpendicular to the dimer axis, the extinction spectrum resembles that of individual nanoparticles (single-particle-like resonance, Figure 1.17, blue line). On the other hand, excitation with incident polarization

along the dimer axis maximizes the interparticle plasmon coupling, leading to a weak blueshifted feature associated with quadrupole modes and a second intense red-shifted band arising from the dipolar coupling of the individual LSPRs of the two spheres (Figure 1.17, green curve).[121, 122]

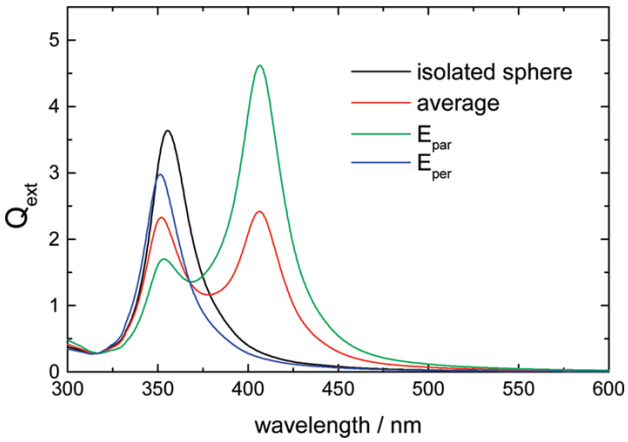

Figure 1.17. Theoretical UV-Vis spectra for parallel (E_{par}) and perpendicular (E_{per}) incident polarization with respect to the dimer axis on the absorption spectrum in vacuum of a Ag dimer with a particle diameter of 30 nm. For comparison, the average extinction spectrum for both polarizations is also reported. Figure from ref. [89]

The reshifted feature is associated with the maximum plasmon coupling and, as for NRs, is the most relevant for SERS. However, while for NRs the largest EM enhancements were localized at the tips of the particle, in the case of the dimer are concentrated at the interparticle gap (Figure 1.18).

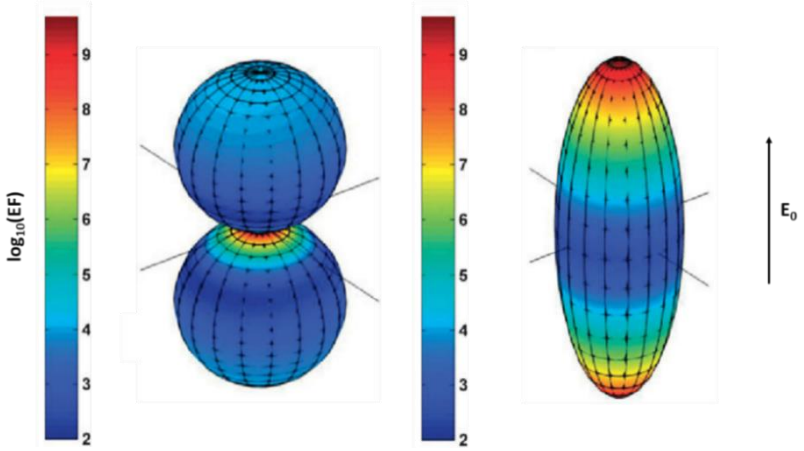

Figure 1.18. Electromagnetic field enhancement as a consequence of hot spot generation in nanospheres (left) and tip hot spot in elongated nanoparticles (right). Adapted with permission from ref. [90]

The intertwined connection between the coupling of LSPRs at the particle junctions and the unique features of the resulting SERS enhancements can be qualitatively described by

considering dimers formed by two identical Ag or Au spheres of 25 nm radius (*a*), immersed in water and illuminated by an incident beam polarized along the dimer axis (i.e. maximum coupling of the LSPRs of each nanoparticle) (Figure 1.19).

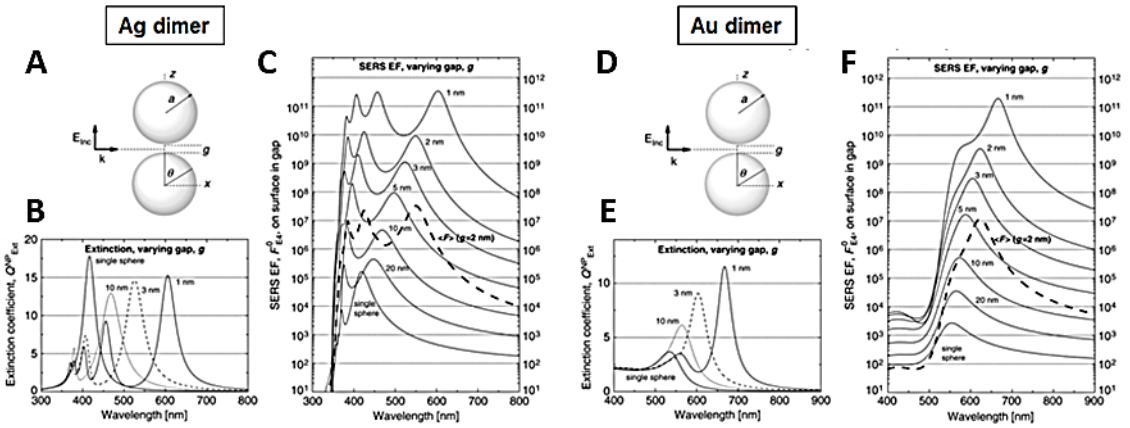

Figure 1.19. (A, D) Schemes represented dimers constituted by two Ag (A) or Au (D) nanospheres displaying a radius *a* of 25 nm and separated by a gap *g*. The incoming light is polarized along the axis of the dimer (*z*) and with wave-vector *k* along *x*. (B, E) Extinction coefficients, Q_{ext}, for gaps with different sizes as functions of incident wavelength for Ag (B) and Au (E) dimers. (C, F) SERS EF at the hot spot for Ag (C) and Au (F) dimers. The thick dashed line is the average SERS EF in the case of a gap *g* = 2 nm. Notably, the resonances in the SERS EF have their counterparts in the extinction spectra, although their respective magnitudes are very different. Figure from ref. [64]

As previously mentioned, the red-shifted resonances, are the most relevant to SERS applications as they are responsible for the largest local EM enhancements. These resonances are highly dependent on the interparticle distance (*d*): as the gap is shortened, the LSPR progressively red-shifts and the local enhancement at the junctions increases rapidly. It is worth stressing the long-tail nature of the SERS enhancements which extends significantly outside the spectral region of the main plasmon resonance (Figure 1.19C and D).[91] The dramatic increase of local EM enhancements for smaller gap distances occurs at increasing levels of spatial localization (i.e., higher local EFs are concentrated within a smaller volume around the hot spot). Moreover, as similarly observed for asymmetric-shaped nanoparticles, the red-shift of the LSPRs beyond ca. 600 nm becomes extremely important for Au nanomaterials. In fact, for single spheres, the maximum SERS EFs of Ag nanoparticles exceed that of Au by ca. 2 orders of magnitude while for 1 nm-gap homometallic dimers, the local EFs at the junctions are similar (Figure 1.19).

A large variety of experimental protocols have been developed to promote nanoparticle aggregation in suspension being the desired features of the final assembled materials (e.g., gap

distances, cluster geometry, stability, reversibility etc.) dictated by the specific use envisaged by the experimentalist. The simplest approach to promote colloidal clustering relies on increasing the ionic strength of the media by the addition of an electrolyte (e.g., KNO_3 and $MgSO_4$ solutions) which reduces the extent of the Coulombic repulsions ensuring the NP stability.[92] However, such an approach typically results in the formation of poorly homogenous assemblies while, for most practical SERS applications, it would be desirable to have a stable dispersion of small colloidal clusters with well-defined structural features to simultaneously guarantee high SERS activity and signal reproducibility.

Alternatively, various controlled electrostatic assembly methods mediated by positively-charged polymers have been reported in the literature. In fact, nanoparticle surfaces are, for most colloids, negatively charged and, then, can be electrostatically assembled using cationic molecules such as cationic poly(ethylene imine) (PEI).[93]

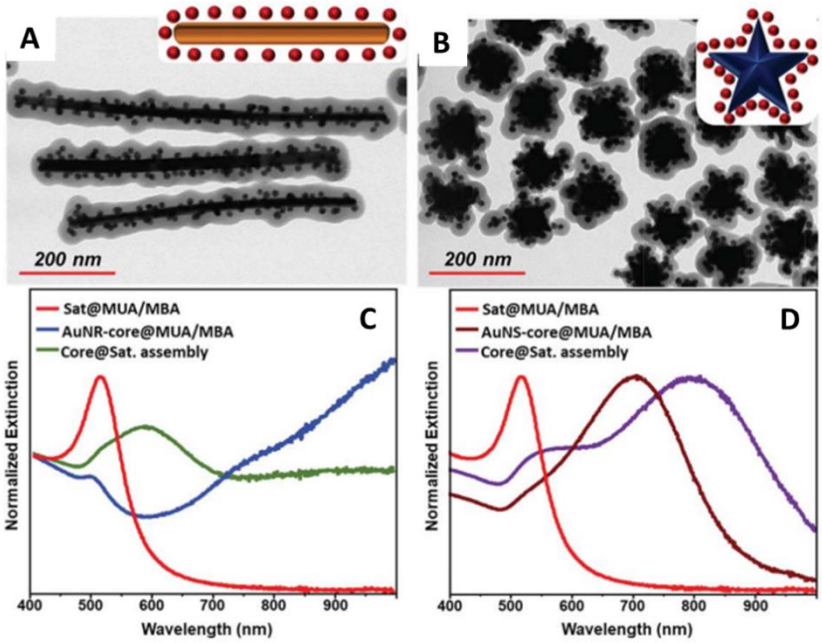

Figure 1.20. (A-B) TEM images of core-satellite assemblies comprising gold satellites (12 nm diameter) and, as the core particle, (A) long gold nanorods or (B) gold nanostars. (C-D) Normalized extinction spectra of individual particles and core-satellite assemblies. Adapted with permission from ref. [94]

For instance, Pazos-Perez et al. [94] devised a simple approach to fabricate homogeneous core-satellites assemblies with minimal interparticle gaps (< 2–3 nm) and maximum particle loading. Integration of plasmonic building blocks of different sizes, shapes, compositions, surface chemistries, or encoding agents is achieved in a modular fashion with minimal modification of the general synthetic protocol. Briefly, the protocol relies on the functionalization of the colloidal cores with mercaptoundecanoic acid (MUA) which strongly

bind the metallic surface via its mercapto group while imparting steric and electrostatic repulsions thanks to the long aliphatic chain and the negatively charged terminal COO^- moiety. These particles were then wrapped with a single layer of positively charged branched PEI which subsequently mediates the electrostatic adhesion of the negatively charged satellites (Figure 1.20).[94]

Using a similar electrostatic-based approach, the polyelectrolyte-assisted layer-by-layer assembly,[95] discrete particles consisting of an inorganic micrometric or sub-micrometric core (e.g., silica, polystyrene) homogeneously coated with a dense collection of plasmonic nanoparticles were also produced (Figure 1.21).[96, 77] This strategy, largely employed in the assembly of metal nanoparticles, [88, 97, 98] leads to a relatively uniform particle deposition derived from the establishment of strong electrostatic interactions between polyelectrolytes and nanoparticles. Thus, the key point for the successful multilayered assembly of metallic nanoparticles on inorganic beads is strongly related to the minute control of the surface charge. The resulting hybrid materials act as robust microscopic carriers of large ensembles of interparticle hot spots concentrated in their external shell which simultaneously retain the positive features of simple metal colloids (e.g., simple fabrication method, ease of surface-functionalization, high SERS activity in their aggregated forms, etc.) while introducing dramatic improvements in terms of colloidal stability, signal reproducibility and ease of manipulation.[99] With these substrates, SERS measurements in suspension can be performed at very low bead concentration,[100, 96] while single-bead analysis can be easily performed by deposition onto a solid surface (micro set-up) since the microparticles can be rapidly visualized with a low magnification objective.[99]

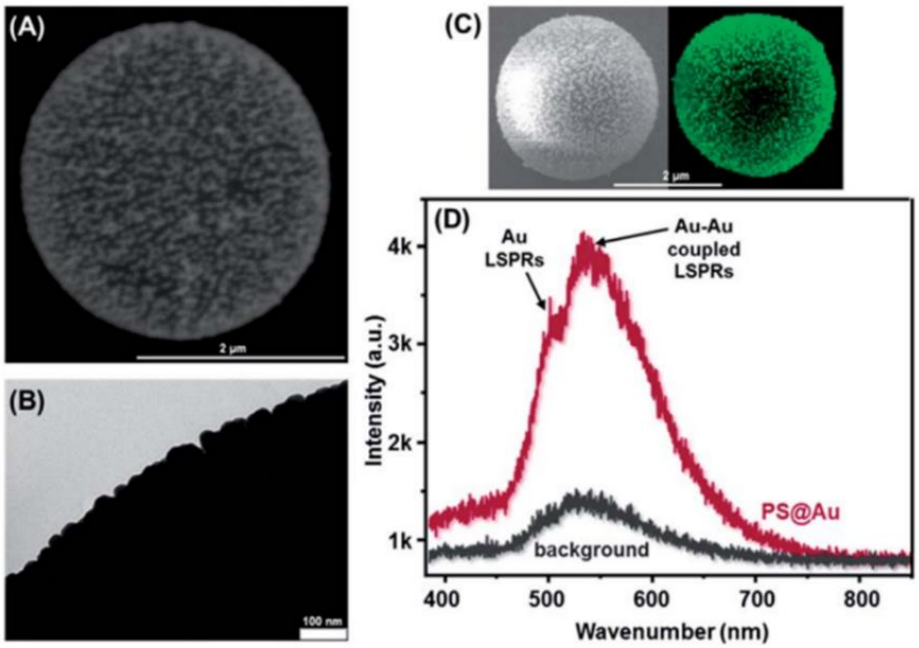

Figure 1.21. (A) ESEM and (B) TEM images of gold-coated polystyrene beads (PS@Au beads). (C) SEM image and photon map centered at 550 nm of a single PS@Au bead. (D) corresponding cathodoluminescence (CL) spectrum. Figure from ref. [96].

1.5 SERS SENSING: DIRECT AND INDIRECT APPROACHES

As previously outlined, the SERS technique combines the inherent structural specificity and high experimental flexibility of Raman spectroscopy with the extremely high sensitivity provided by the plasmonic-mediated enhancement. As a result, SERS spectroscopy emerged as an ultrasensitive analytical tool that has been continuously expanding its range of applications in several fields, including sensing and biosensing, biology, medicine, environmental monitoring, food safety or catalysis, among others.[101] As the magnification of the Raman scattering primarily depends on the excitation of LSPRs to generate intense electric fields at the metallic surfaces (mostly silver or gold), the design of the plasmonic substrate is central to SERS analysis. Besides the intrinsic optical response of the nanomaterial, the fine-tuning of its surface physicochemical properties is key to maximizing the sensing performances as well as to guiding, when desired, its potential assembly into more complex architectures.[47, 102]

Broadly speaking, SERS sensing strategies are generally classified based on two general principles: direct and indirect approaches. The direct methodologies rely on the acquisition of the intrinsic SERS spectra of the target species to detect its presence and, possibly, quantify its content in the sample.[103] In this context, the analyte must exhibit sufficient affinity for adsorbing onto the metallic surface, typically via covalent attachment (e.g., via sulfur-metal bonds) or electrostatic attractions.[47, 104] Alternatively, the indirect sensing scheme relies on monitoring the alteration of the SERS signal (e.g., absolute intensity, reshaping of the spectral) yielded by an extrinsic SERS label (i.e., indirect SERS) and caused by the interaction with the target molecule.

A representative example of the adoption of direct SERS analysis in biosensing is provided by the detection of small thiolated biomolecules in bodily fluids.[105, 106] Low molecular weight thiols play a key role in human physiology, most notably in the maintenance of cellular redox homeostasis.[107] Abnormal levels, such as those of the most abundant biothiols (e.g., glutathione (GSH) and cysteine (Cys)) have been associated with cancer,[108] neurodegenerative disorders,[109] and cardiovascular diseases,[110] among others. Moreover, the overall dysregulation of the dynamic thiol-disulfide homeostasis has been also related to multiple diseases.[111] Due to the clinical relevance of biothiols in human health, the development of methods for their rapid determination in biological fluids is essential for early diagnosis and disease monitoring, as well as for acquiring a better understanding of biothiol-related pathophysiological processes.[112] Direct SERS detection of this class of molecules is facilitated by the strong affinity of the mercapto group which covalently binds the surface of Au and Ag nanoparticles.[105, 113] For instance, Sánchez-Illana et al.[113] developed an on-capillary SERS method for the fast and direct

quantification of GSH in whole blood. Small volumes of appropriately pretreated blood samples (Figure 1.22) were combined with silver colloids yielding SERS spectra exhibiting characteristic vibrational features of GSH attached onto the metallic surface via Ag-S bond, such as the intense bands at 647 cm^{-1}, associated with C-S stretching mode, 793 cm^{-1}, ascribed to C=N amide V band vibration, 1414 cm^{-1}, related to COO^- symmetric stretching, 1567 cm^{-1}, and 1738 cm^{-1}, assigned to C=N amide II band and C=O stretching mode respectively.[113, 114, 115, 116] The SERS measurements were performed in a microvolume capillary measurement cell, facilitating the rapid analysis of small sample volumes.

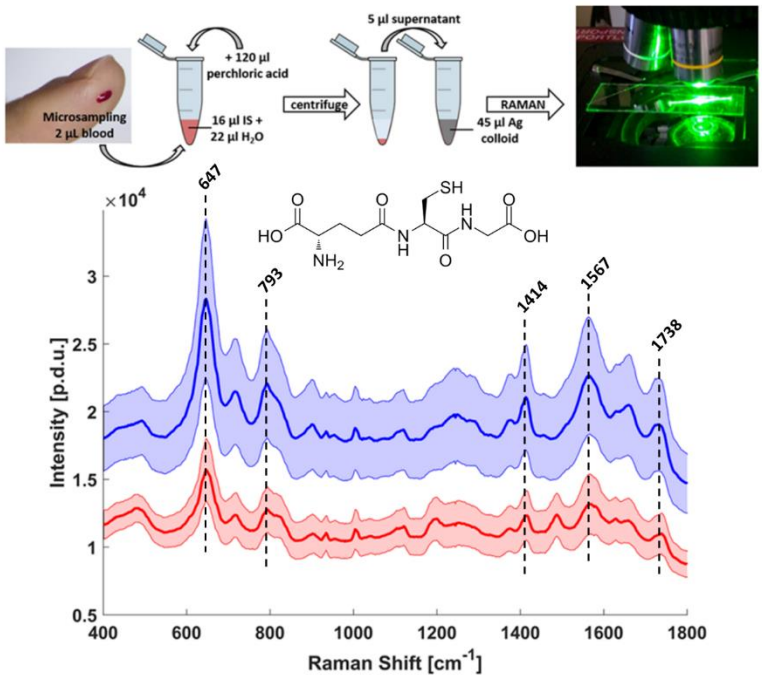

Figure 1.22. (top) Scheme of the sample processing steps. (bottom) SERS spectra of a GSH standard solution (blue) and a blood sample (red). Adapted with permission from ref. [113]

Beyond the specific case of GSH, the intrinsic nature of the direct approach poses some general limitations, most notably the need of targeting analytes with high affinity for the plasmonic surfaces and, typically, performing pre-purification steps to reduce the complexity of the medium. In fact, in complex media, other molecules can compete with the target species for absorption on the metal, which can hamper the attachment of the analyte and/or produce unintelligible SERS spectra resulting from a multitude of different scatterers. Conversely, indirect SERS approaches, despite missing the rich structural information contained in the intrinsic SERS fingerprint of the analyte, are intrinsically more suited for designing sensing platforms capable of performing SERS analysis directly in the complex media with minimal or null pre-treatment, while simultaneously favoring multiplex and quantitative responses.

Notably, the most common implementation of indirect SERS is by using SERS encoded nanoparticles (also referred to as SERS tags) which function similarly to fluorescent labels but with improved multiplexing, photostability, and quantitative response.[106] SERS encoded nanoparticles (SEPs) typically comprise a plasmonic core as the optical enhancer, surface elements as selective receptors for target molecules, and a SERS label (or reporter) that firmly attaches the metallic surface to provide a unique SERS fingerprint (Figure 1.23A).[117] An additional coating layer (e.g., silica) is also often included in the nanomaterial design to simultaneously provide high colloidal stability, a convenient surface for further chemical functionalization, and protection of the SERS-labelled metallic surface from the media components. For instance, Pazos-Perez and coworkers[118] exploited SEPs to devise a microorganism optical detection system for real-time, multiplexed pathogen identification and quantification via rapid screening of large bodily-fluid volumes (Figure 1.23B-C). SEPs were conjugated with selective antibodies targeting different receptors of distinct pathogens. In other words, for each targeted pathogen receptor, SEPs exhibit a unique combination of SERS label and selective antibody. Thus, the mixing of bacteria-containing fluids with antibody-functionalized SERS-encoded nanoparticles caused the SEP accumulation at the bacteria membrane producing a spike of the corresponding SERS intensity which is registered as a positive event (i.e., recognition of a bacteria colony-forming unit).

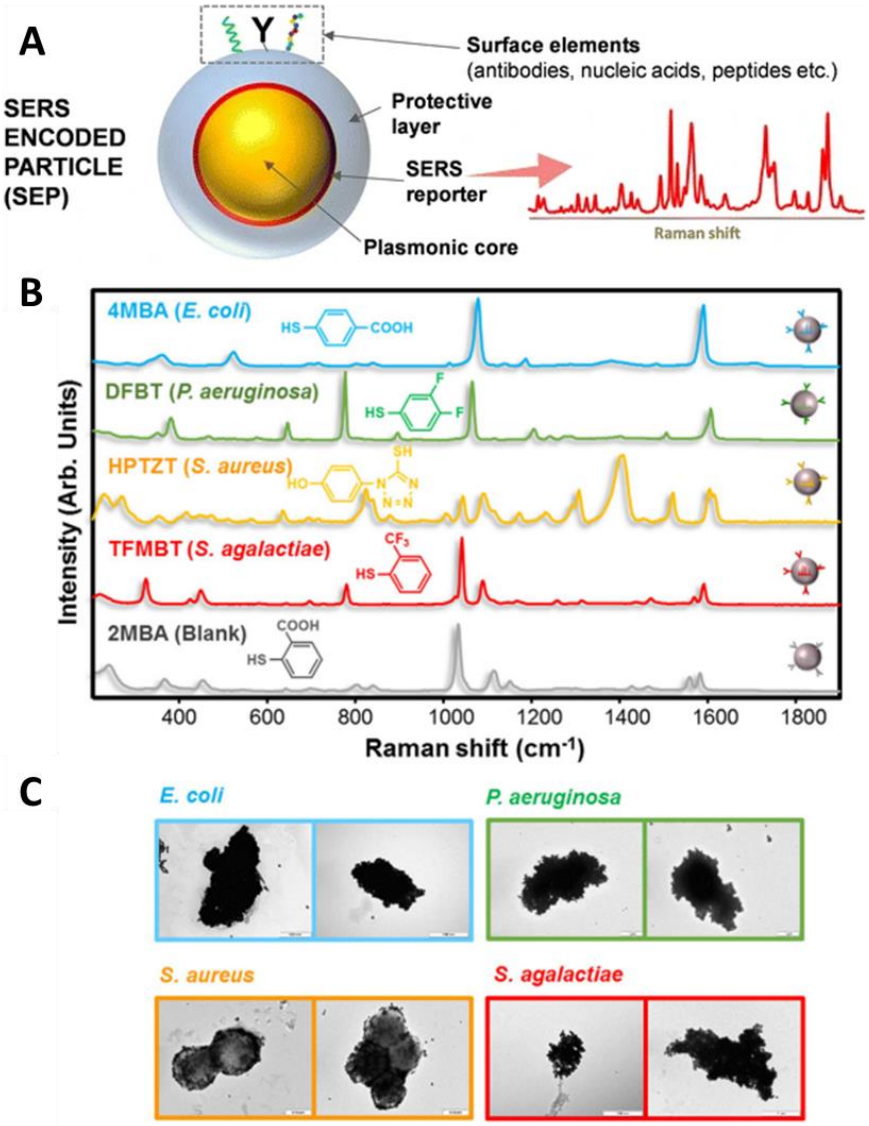

Figure 1.23. (A) Schematic representation of a typical SERS-encoded particle. Adapted with permission from ref. [117] (B) SERS spectra of the different encoded particles used for each targeted pathogen together with their corresponding labeling molecules. (C) TEM images of the targeted bacteria coated with their respective matching particles. Adapted with permission from ref. [118]

Alternatively, a rather advantageous indirect sensing approach is to combine within the same surface element both the selective receptor and the SERS label. In this scenario, the resulting "chemoreceptor" molecule acts as a SERS transducer by converting the receptor/target complex formation into measurable alterations of its spectral profile which, in turn, can be quantitatively correlated with the number of binding events.[119] In this sensing scheme, the chemoreceptor can also be used as an internal standard for ratiometric SERS analysis, which further improves the reproducibility and robustness of the sensing response as compared to methods that solely rely on the acquisition of absolute intensities for quantification.[119] A

paradigmatic example is presented by the work of Guerrini et al.,[120] which developed a SERS-based sensor for the detection of the oncoprotein c-Jun at nanomolar levels. Here, the authors synthesized a chemoreceptor comprising a peptide sequence with a high affinity and selectivity for the oncoprotein c-Jun which was orthogonally modified with a 4-mercapto benzoyl unit (MB) at a terminal amino acid residue. A monolayer of the peptide chemoreceptor (MB-Fos) was deposited on a silver island film via metal-sulfur bonding of the MB extremity (Figure 1.24A), yielding intense SERS features of the mercaptophenyl group (Figure 1.24B).[121] Among others, it is possible to recognize the in-plane modes such as those centered at 1585 cm^{-1} (C=C stretching), 1075 cm^{-1}, (ring breathing mode coupled with ν(C-S)), 1022 cm^{-1} (CCH deformation), 998 cm^{-1} (ring breathing mode) and 417 cm^{-1} (C-S stretching coupled to in-plane ring bending). c-Jun binding to the chemoreceptor causes the folding of the loosely structured peptide sequence into a relatively rigid α-helix conformation (Figure 1.24A) which, in turn, generates a broad set of spectral changes. This includes the blueshift of the 1075 cm^{-1} band (Figure 1.24C) and the drastic change in relative intensity between the shoulder at ca. 1574 cm^{-1}, ascribed to the non-totally symmetric ν(C=C) vibration, vs the totally symmetric ν(C=C) mode centered at 1585 cm^{-1} (Figure 1.24D). [122] These spectral alterations have been associated with the perturbation of the benzene ring symmetry in the surface complex.[122] The c-Jun content was quantitatively correlated with ratiometric peak intensities, I_{1574}/I_{1585} (Figure 1.24E), which shows a linear response over a broad range of oncoprotein concentration in cell lysates and a detection limit of 5 nM.[122]

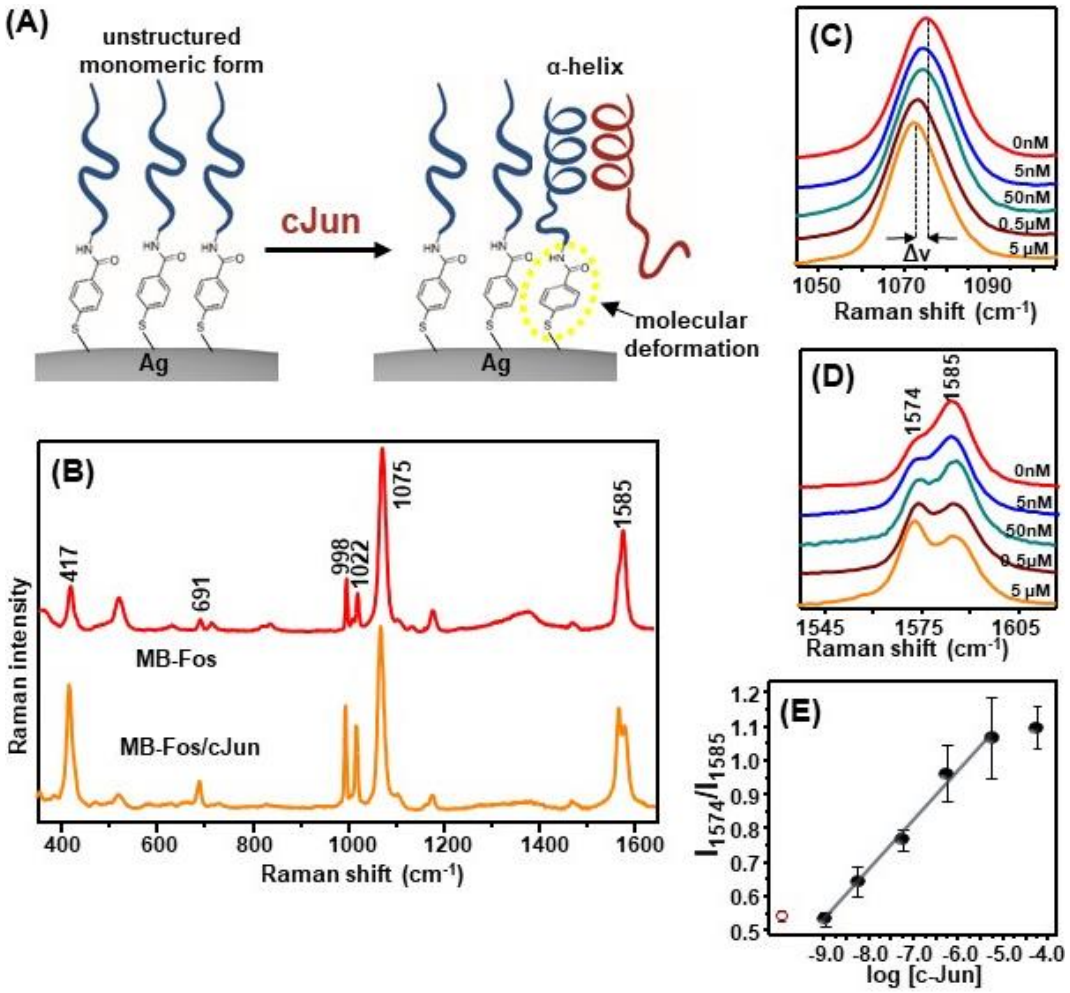

Figure 1.24. (A) Representative scheme of the MB-Fos/c-Jun dimerization on the metal surface and the resulting SERS transducer structural deformation. (B) SERS spectra of MB-Fos and MB-Fos/c-Jun on the Ag film. In detail, (C) 1000-1100 cm^{-1} and (D) 1540-1620 cm^{-1} spectral regions of the MB-Fos SERS spectra after exposure to c-Jun solution in HEPES buffer at increasing concentrations. (E) Intensity ratio I_{1574}/I_{1585} as a function of c-Jun concentration (logarithmic scale). Adapted with permission from ref. [120]

Hybrid indirect methodologies have been also reported. For instance, Chenbiao et al. [123] devised a method for biothiols detection in which nanoparticles were functionalized with oligo sequences of DNA equipped with Cy5 (a SERS reporter) and a disulfide bond (Figure 1.25A). In the presence of low molecular weight thiols, such as GSH, the disulfide bond is cleaved producing the release of the DNA segment carrying the Cy5 label. This, in turn, leads to a drop of SERS intensity (Figure 1.25B) which is proportional to the GSH concentration.[123]

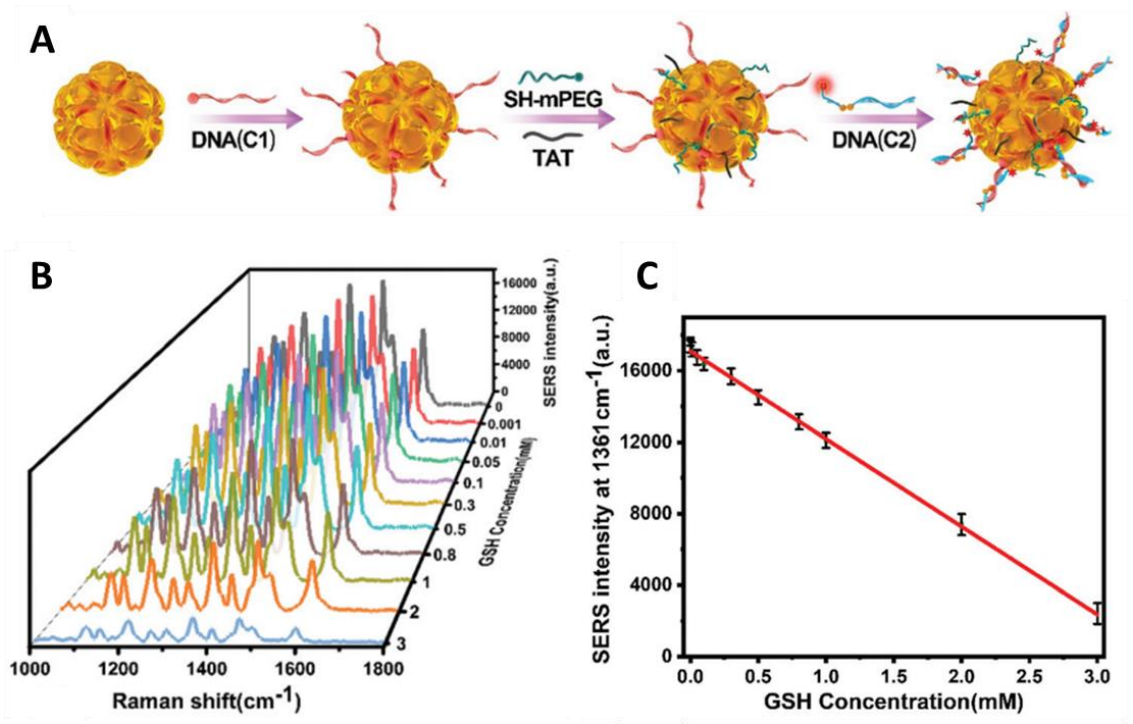

Figure 1.25. (A) Schematic overview of the biothiols nanosensor. (B) In vitro SERS spectra. (C) Linearly correlation of SERS intensity decrement plotted against increasing GSH concentration. Adapted with permission from ref. [123]

1.6 METAMATERIALS

Metamaterials constitute a new frontier for sciences such as physic, material science, engineering, and chemistry for the unique properties of these materials.[124, 125, 126] Metamaterials can be described as artificially structured units composed of arrangements of two or more conventional materials, typically noble metals, periodically repeated in packed arrays (Figure 1.26).[30, 127, 128] This peculiar architecture enables exotic optical properties which are strongly dependent on the structure itself rather than their individual components.[124, 129, 130] In the regularly arrayed unit composing the 3D crystal lattice metamaterial (Figure 1.26 bottom), the induced electric dipoles couple with each other. The incoming electric field can be efficiently concentrated and maximized when it is parallelly aligned with metaunits as a result of the strong interparticle coupling. On the contrary, when is perpendicularly aligned along the direction of the metaunits, the electric field is fully quenched (Figure 1.26 top).[131, 132, 133]

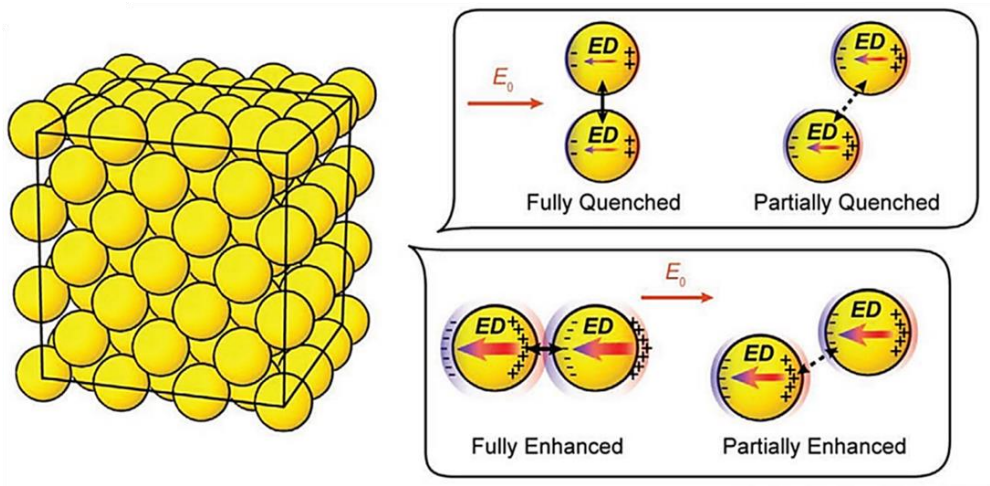

Figure 1.26. Representation of regularly arrayed metaunits. Quenching (top) and enhancement (bottom) of the incoming field via induced electric dipoles (EDs) interaction (incoming field perpendicular and parallel to the units, respectively). Adapted with permission of ref. [131]

Early metamaterials realized by Kock in 1948[134] were constituted of centimeter-scale arrays of metallic nanoparticles. These structures, indicated as *artificial dielectrics,* were able to focus radio waves as a dielectric and, at such frequencies, the metallic nanoparticles forming the arrays behaved as perfect conductors (i.e., no electromagnetic field can penetrate and be absorbed). As the losses among particles were inappreciable, metallic arrays were highly transparent to radio waves.[126, 30, 135]

Silver and gold are widely employed as building blocks in the production of metamaterials.[136, 137] However, the resulting metamaterials are usually dominated by the

resonant behavior of their constituents with high losses at optical frequencies associated with the corresponding excitation of LSPRs. This hampers their applicability to the frequency of their characteristic resonances.[138] Nonetheless, it has been demonstrated that, though metals are highly opaque, metamaterials composed of densely packed metallic nanoparticle arrays behave as an effective dielectric.[139] Thus, despite the abovementioned issue, increasingly studies have been devoted to the design of achromatic optical devices composed of compact metallic arrays with high transparency and able to manipulate wavelength in the desired spectrum region.[131, 140] For example, Figure 1.27 illustrates the periodic arrays of perpendicularly oriented gold nanorods (AuNRs). In these metamaterials, the optical properties are determined by the strong near-field interparticle coupling in the NR assembly which can be tuned throughout the visible and near-infrared spectral ranges by adjusting diameter, length, and spacing among the individual nanoparticles. Indeed, as shown in the extinction spectra (Figure 1.27 D), polarized light exhibits two pronounced resonances: the short-wavelength peak, which is associated with the light polarized perpendicularly to the NRs, and the long-wavelength peak with a strong angle of incidence dependence, which is observed for the light polarized along the long nanorod axis.[124]

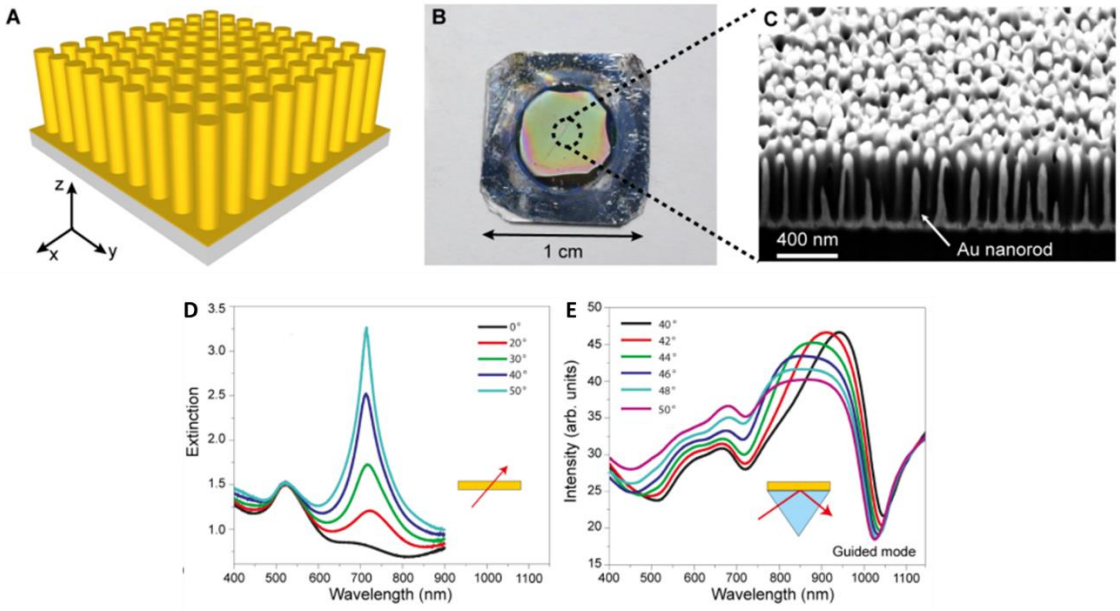

Figure 1.27. (A) Structure of the plasmonic metamaterial composed of gold nanorods. (B) Image of a nanorod metamaterial chip. (C) Cross-sectional view of the metamaterial. (D) Extinction spectra obtained in the direct-transmission geometry with transverse magnetic polarized light and (E) reflection spectra of a gold nanorod metamaterial. Adapted with permission from ref.[124]

REFERENCES

1. Hulla, J.; Sahu, S.; Hayes, A., Nanotechnology: History and future. *Human & experimental toxicology* **2015,** *34* (12), 1318-1321.
2. Ozin, G. A.; Arsenault, A., *Nanochemistry: a chemical approach to nanomaterials*. Royal Society of Chemistry: **2015**.
3. Ohno, H.; Akamine, S.; Saito, H., RNA nanostructures and scaffolds for biotechnology applications. *Current opinion in biotechnology* **2019,** *58*, 53-61.
4. Dupas, C.; Lahmani, M., *Nanoscience: Nanotechnologies and nanophysics*. Springer Science & Business Media: **2007**.
5. Taheri, A.; Jafari, S. M., Gum-based nanocarriers for the protection and delivery of food bioactive compounds. *Advances in colloid and interface science* **2019,** *269*, 277-295.
6. Kim, J.; Ahn, S. I.; Kim, Y., Nanotherapeutics engineered to cross the blood-brain barrier for advanced drug delivery to the central nervous system. *Journal of Industrial and Engineering Chemistry* **2019,** *73*, 8-18.
7. Feynman, R., *There's plenty of room at the bottom*. CRC Press: **2018**.
8. Taniguchi, N., On the basic concept of nanotechnology. *Proceeding of the ICPE* **1974**.
9. Drexler, K. E., *Engines of creation*. Anchor books: **1986**.
10. Kunicki-Goldfinger, J. J.; Freestone, I. C.; McDonald, I.; Hobot, J. A.; Gilderdale-Scott, H.; Ayers, T., Technology, production and chronology of red window glass in the medieval period–rediscovery of a lost technology. *Journal of Archaeological Science* **2014,** *41*, 89-105.
11. Heiligtag, F. J.; Niederberger, M., The fascinating world of nanoparticle research. *Materials Today* **2013,** *16* (7-8), 262-271.
12. Jeevanandam, J.; Barhoum, A.; Chan, Y. S.; Dufresne, A.; Danquah, M. K., Review on nanoparticles and nanostructured materials: history, sources, toxicity and regulations. *Beilstein journal of nanotechnology* **2018,** *9* (1), 1050-1074.
13. Freestone, I.; Meeks, N.; Sax, M.; Higgitt, C., The Lycurgus cup—a roman nanotechnology. *Gold bulletin* **2007,** *40* (4), 270-277.
14. Giannini, V.; Fernández-Domínguez, A. I.; Heck, S. C.; Maier, S. A., Plasmonic nanoantennas: fundamentals and their use in controlling the radiative properties of nanoemitters. *Chemical reviews* **2011,** *111* (6), 3888-3912.
15. Krishnan, R.; Shankar, R., Raman effect: History of the discovery. *Journal of Raman Spectroscopy* **1981,** *10* (1), 1-8.
16. Chalmers, J. M.; Griffiths, P. R., *Handbook of vibrational spectroscopy*. Wiley: 2002.
17. Ember, K. J.; Hoeve, M. A.; McAughtrie, S. L.; Bergholt, M. S.; Dwyer, B. J.; Stevens, M. M.; Faulds, K.; Forbes, S. J.; Campbell, C. J., Raman spectroscopy and regenerative medicine: a review. *NPJ Regenerative medicine* **2017,** *2* (1), 1-10.
18. LeRu, E.; Etchegoin, P., Principles of Surface Enhanced Raman Spectroscopy Elsevier. Oxford University Press: **2009**.
19. Guimbretière, G.; Duraipandian, S.; Ricci, T., Field remote Stokes/anti-Stokes Raman characterization of sulfur in hydrothermal vents. *Journal of Raman Spectroscopy* **2018,** *49* (8), 1385-1394.
20. Aroca, R., Theory of molecular vibrations. The origin of infrared and raman spectra. *Surface-Enhanced Vibrational Spectroscopy* **2007**, 1-33.
21. Le Ru, E.; Etchegoin, P., *Principles of Surface-Enhanced Raman Spectroscopy: and related plasmonic effects*. Elsevier: **2008**; p 76-77.
22. Aroca, R., *Surface-enhanced vibrational spectroscopy*. John Wiley & Sons: **2006**.
23. Le Ru, E. C.; Etchegoin, P. G., *Principles of Surface-Enhanced Raman Spectroscopy*. Elsevier: Amsterdam, The Netherlands, **2009**.
24. Matousek, P.; Morris, M., *Emerging Raman applications and techniques in biomedical and pharmaceutical fields*. Springer Science & Business Media: **2010**.
25. Li-Chan, E. C., The applications of Raman spectroscopy in food science. *Trends in Food Science & Technology* **1996,** *11* (7), 361-370.
26. Gouda, A. M.; Allam, N. K.; Swillam, M. A., Efficient fabrication methodology of wide angle black silicon for energy harvesting applications. *RSC advances* **2017,** *7* (43), 26974-26982.
27. Yang, S.; Chen, Q.; Shi, M.; Zhang, Q.; Lan, S.; Maimaiti, T.; Li, Q.; Ouyang, P.; Tang, K.; Yang, S.-T., Fast identification and quantification of graphene oxide in aqueous environment by Raman spectroscopy. *Nanomaterials* **2020,** *10* (4), 770.

28. Le Ru, E.; Etchegoin, P., *Principles of Surface-Enhanced Raman Spectroscopy: and related plasmonic effects*. Elsevier: **2008**; p 123-124.
29. Rodrigues, M. S.; Borges, J.; Lopes, C.; Pereira, R. M. S.; Vasilevskiy, M. I.; Vaz, F., Gas Sensors Based on Localized Surface Plasmon Resonances: Synthesis of Oxide Films with Embedded Metal Nanoparticles, Theory and Simulation, and Sensitivity Enhancement Strategies. *Applied Sciences* **2021,** *11* (12), 5388.
30. Palmer, S. J.; Xiao, X.; Pazos-Perez, N.; Guerrini, L.; Correa-Duarte, M. A.; Maier, S. A.; Craster, R. V.; Alvarez-Puebla, R. A.; Giannini, V., Extraordinarily transparent compact metallic metamaterials. *Nature communications* **2019,** *10* (1), 1-7.
31. Born, M.; Wolf, E., *Principles of optics: electromagnetic theory of propagation, interference and diffraction of light*. Elsevier: **2013**.
32. Etchegoin, P. G.; Le Ru, E. C., Basic electromagnetic theory of SERS. *Surface Enhanced Raman Spectroscopy* **2010**, 1-37.
33. Platzman, P. M.; Wolff, P. A., *Waves and interactions in solid state plasmas*. Academic Press New York: **1973**; Vol. 13.
34. Dressel, M.; Grüner, G., Electrodynamics of solids: optical properties of electrons in matter. American Association of Physics Teachers: **2002**.
35. Le Ru, E.; Etchegoin, P., *Principles of Surface-Enhanced Raman Spectroscopy: and related plasmonic effects*. Elsevier: **2008**; p 123-131.
36. Morton, S. M.; Silverstein, D. W.; Jensen, L., Theoretical studies of plasmonics using electronic structure methods. *Chemical reviews* **2011,** *111* (6), 3962-3994.
37. Le Ru, E.; Etchegoin, P., *Principles of Surface-Enhanced Raman Spectroscopy: and related plasmonic effects*. Elsevier: **2008**; p 128-131.
38. Le Ru, E.; Etchegoin, P., *Principles of Surface-Enhanced Raman Spectroscopy: and related plasmonic effects*. Elsevier: **2008**; p 282-310.
39. Radziuk, D.; Moehwald, H., Prospects for plasmonic hot spots in single molecule SERS towards the chemical imaging of live cells. *Physical Chemistry Chemical Physics* **2015,** *17* (33), 21072-21093.
40. Aroca, R. F., Plasmon enhanced spectroscopy. *Physical Chemistry Chemical Physics* **2013,** *15* (15), 5355-5363.
41. Kang, H.; Buchman, J. T.; Rodriguez, R. S.; Ring, H. L.; He, J.; Bantz, K. C.; Haynes, C. L., Stabilization of silver and gold nanoparticles: preservation and improvement of plasmonic functionalities. *Chemical reviews* **2018,** *119* (1), 664-699.
42. Etchegoin, P. G.; Le Ru, E.; Meyer, M., An analytic model for the optical properties of gold. *The Journal of chemical physics* **2006,** *125* (16), 164705.
43. Frederix, F.; Friedt, J.-M.; Choi, K.-H.; Laureyn, W.; Campitelli, A.; Mondelaers, D.; Maes, G.; Borghs, G., Biosensing based on light absorption of nanoscaled gold and silver particles. *Analytical chemistry* **2003,** *75* (24), 6894-6900.
44. Alvarez-Puebla, R. A.; Aroca, R. F., Synthesis of silver nanoparticles with controllable surface charge and their application to surface-enhanced Raman scattering. *Analytical chemistry* **2009,** *81* (6), 2280-2285.
45. Guentherodt, A. O. e. b. M. C. a. G., Light Scattering in Solids. *Springer, Berlin, 1984* **1984**.
46. Moskovits, M., Surface-enhanced spectroscopy. *Reviews of Modern Physics* **1985,** *57* (3), 783-826.
47. Guerrini, L.; Graham, D., Molecularly-mediated assemblies of plasmonic nanoparticles for Surface-Enhanced Raman Spectroscopy applications. *Chem. Soc. Rev.* **2012,** *41* (21), 7085-7107.
48. Le Ru, E.; Etchegoin, P., *Principles of Surface-Enhanced Raman Spectroscopy: and related plasmonic effects*. Elsevier: **2008**; p 202-204.
49. Le Ru, E.; Etchegoin, P., *Principles of Surface-Enhanced Raman Spectroscopy: and related plasmonic effects*. Elsevier: **2008**; p 217-219.
50. Moskovits, M.; Suh, J., Surface selection rules for surface-enhanced Raman spectroscopy: calculations and application to the surface-enhanced Raman spectrum of phthalazine on silver. *The Journal of Physical Chemistry* **1984,** *88* (23), 5526-5530.
51. Kneipp, K.; Wang, Y.; Kneipp, H.; Perelman, L. T.; Itzkan, I.; Dasari, R. R.; Feld, M. S., Single molecule detection using surface-enhanced Raman scattering (SERS). *Physical review letters* **1997,** *78* (9), 1667.
52. Zhang, L.; Zhao, Q.; Jiang, Z.; Shen, J.; Wu, W.; Liu, X.; Fan, Q.; Huang, W., Recent Progress of SERS Nanoprobe for pH Detecting and Its Application in Biological Imaging. *Biosensors* **2021,** *11* (8), 282.

53. Nie, S.; Emory, S. R., Probing Single Molecules and Single Nanoparticles by Surface-Enhanced Raman Scattering. *Science* **1997,** *275* (5303), 1102-1106.
54. Le Ru, E.; Etchegoin, P., Rigorous justification of the| E| 4 enhancement factor in surface enhanced Raman spectroscopy. *Chemical Physics Letters* **2006,** *423* (1-3), 63-66.
55. Le Ru, E.; Etchegoin, P., *Principles of Surface-Enhanced Raman Spectroscopy: and related plasmonic effects*. Elsevier: **2008**; p 185-192.
56. Moskovits, M., Persistent misconceptions regarding SERS. *Physical Chemistry Chemical Physics* **2013,** *15* (15), 5301-5311.
57. Ko, H.; Singamaneni, S.; Tsukruk, V. V., Nanostructured surfaces and assemblies as SERS media. *Small* **2008,** *4* (10), 1576-1599.
58. Tessier, P. M.; Velev, O. D.; Kalambur, A. T.; Lenhoff, A. M.; Rabolt, J. F.; Kaler, E. W., Structured metallic films for optical and spectroscopic applications via colloidal crystal templating. *Advanced Materials* **2001,** *13* (6), 396-400.
59. Wang, H.; Levin, C. S.; Halas, N. J., Nanosphere arrays with controlled sub-10-nm gaps as surface-enhanced Raman spectroscopy substrates. *Journal of the American Chemical Society* **2005,** *127* (43), 14992-14993.
60. LeRu, E.; Etchegoin, P., Principles of Surface Enhanced Raman Spectroscopy Elsevier. Oxford University Press: **2009**; pp 5-13.
61. Lee, P. C.; Meisel, D., Adsorption and Surface-Enhanced Raman of Dyes on Silver and Gold Sols. *J. Phys. Chem.* **1982,** *86* (17), 3391-3395.
62. Sun, Y.; Gray, S. K.; Peng, S., Surface chemistry: a non-negligible parameter in determining optical properties of small colloidal metal nanoparticles. *Physical Chemistry Chemical Physics* **2011,** *13* (25), 11814-11826.
63. Blanco-Formoso, M.; Turino, M.; Rivas-Murias, B.; Guerrini, L.; Shavel, A.; de la Rica, R.; Correa-Duarte, M.; Salgueiriño, V.; Pazos-Perez, N.; Alvarez-Puebla, R. A., Iron-Assisted Synthesis of Highly Monodispersed and Magnetic Citrate-Stabilized Small Silver Nanoparticles. *The Journal of Physical Chemistry C* **2020,** *124* (5), 3270-3276.
64. Le Ru, E. C.; Etchegoin, P. G., *Principles of Surface-Enhanced Raman Spectroscopy*. Elsevier: Amsterdam, **2009**.
65. Attia, Y. A.; Buceta, D.; Requejo, F. G.; Giovanetti, L. J.; López-Quintela, M. A., Photostability of gold nanoparticles with different shapes: the role of Ag clusters. *Nanoscale* **2015,** *7* (26), 11273-11279.
66. Xavier, J.; Vincent, S.; Meder, F.; Vollmer, F., Advances in optoplasmonic sensors – combining optical nano/microcavities and photonic crystals with plasmonic nanostructures and nanoparticles. *Nanophotonics* **2018,** *7* (1), 1-38.
67. (a) Giannini, V.; Fernandez-Dominguez, A. I.; Sonnefraud, Y.; Roschuk, T.; Fernandez-Garcia, R.; Maier, S. A., Controlling light localization and light-matter interactions with nanoplasmonics. *Small* **2010,** *6* (22), 2498-2507; (b) Giannini, V.; Fernandez-Dominguez, A. I.; Heck, S. C.; Maier, S. A., Plasmonic Nanoantennas: Fundamentals and Their Use in Controlling the Radiative Properties of Nanoemitters. *Chem. Rev.* **2011,** *111* (6), 3888-3912.
68. Huang, X. H.; Neretina, S.; El-Sayed, M. A., Gold Nanorods: From Synthesis and Properties to Biological and Biomedical Applications. *Adv. Mater.* **2009,** *21* (48), 4880-4910.
69. Hinman, J. G.; Stork, A. J.; Varnell, J. A.; Gewirth, A. A.; Murphy, C. J., Seed mediated growth of gold nanorods: towards nanorod matryoshkas. *Faraday Discussions* **2016,** *191* (0), 9-33.
70. Sánchez-Iglesias, A.; Carbó-Argibay, E.; Glaria, A.; Rodríguez-González, B.; Pérez-Juste, J.; Pastoriza-Santos, I.; Liz-Marzán, L. M., Rapid epitaxial growth of Ag on Au nanoparticles: from Au nanorods to core–shell Au@ Ag octahedrons. *Chemistry–A European Journal* **2010,** *16* (19), 5558-5563.
71. Liu, M.; Guyot-Sionnest, P., Synthesis and optical characterization of Au/Ag core/shell nanorods. *The Journal of Physical Chemistry B* **2004,** *108* (19), 5882-5888.
72. Tebbe, M.; Kuttner, C.; Mayer, M.; Maennel, M.; Pazos-Perez, N.; König, T. A.; Fery, A., Silver-overgrowth-induced changes in intrinsic optical properties of gold nanorods: From noninvasive monitoring of growth kinetics to tailoring internal mirror charges. *The Journal of Physical Chemistry C* **2015,** *119* (17), 9513-9523.
73. Sun, Y.; Mayers, B. T.; Xia, Y., Template-engaged replacement reaction: a one-step approach to the large-scale synthesis of metal nanostructures with hollow interiors. *Nano Letters* **2002,** *2* (5), 481-485.
74. Sun, Y.; Xia, Y., Shape-controlled synthesis of gold and silver nanoparticles. *science* **2002,** *298* (5601), 2176-2179.

75. Guisbiers, G.; Mendoza-Cruz, R. n.; Bazán-Díaz, L.; Velázquez-Salazar, J. J. s.; Mendoza-Perez, R.; Robledo-Torres, J. A.; Rodriguez-Lopez, J.-L.; Montejano-Carrizales, J. M.; Whetten, R. L.; José-Yacamán, M., Electrum, the gold–silver alloy, from the bulk scale to the nanoscale: synthesis, properties, and segregation rules. *ACS nano* **2016,** *10* (1), 188-198.
76. Fernanda Cardinal, M.; Rodríguez-González, B.; Alvarez-Puebla, R. A.; Pérez-Juste, J.; Liz-Marzán, L. M., Modulation of localized surface plasmons and SERS response in gold dumbbells through silver coating. *The Journal of Physical Chemistry C* **2010,** *114* (23), 10417-10423.
77. Tsoutsi, D.; Montenegro, J. M.; Dommershausen, F.; Koert, U.; Liz-Marzan, L. M.; Parak, W. J.; Alvarez-Puebla, R. A., Quantitative surface-enhanced Raman scattering ultradetection of atomic inorganic ions: the case of chloride. *Acs Nano* **2011,** *5* (9), 7539-7546.
78. Mayer, M.; Scarabelli, L.; March, K.; Altantzis, T.; Tebbe, M.; Kociak, M.; Bals, S.; García de Abajo, F. J.; Fery, A.; Liz-Marzán, L. M., Controlled living nanowire growth: precise control over the morphology and optical properties of AgAuAg bimetallic nanowires. *Nano letters* **2015,** *15* (8), 5427-5437.
79. Gómez-Graña, S.; Goris, B.; Altantzis, T.; Fernández-López, C.; Carbó-Argibay, E.; Guerrero-Martínez, A. s.; Almora-Barrios, N.; López, N.; Pastoriza-Santos, I.; Pérez-Juste, J., Au@ Ag nanoparticles: Halides stabilize {100} facets. *The journal of physical chemistry letters* **2013,** *4* (13), 2209-2216.
80. Sanders, D. E.; DePristo, A. E., Predicted diffusion rates on fcc (001) metal surfaces for adsorbate/substrate combinations of Ni, Cu, Rh, Pd, Ag, Pt, Au. *Surface science* **1992,** *260* (1-3), 116-128.
81. Ferguson, G. S.; Chaudhury, M. K.; Sigal, G. B.; Whitesides, G. M., Contact adhesion of thin gold films on elastomeric supports: cold welding under ambient conditions. *Science* **1991,** *253* (5021), 776-778.
82. Ji, C.; Searson, P. C., Synthesis and characterization of nanoporous gold nanowires. *The Journal of Physical Chemistry B* **2003,** *107* (19), 4494-4499.
83. Ostwald, W., Studien über die Bildung und Umwandlung fester Körper. *Z. Phys. Chem.* **1897,** (22), 289–330.
84. Grouchko, M.; Roitman, P.; Zhu, X.; Popov, I.; Kamyshny, A.; Su, H.; Magdassi, S., Merging of metal nanoparticles driven by selective wettability of silver nanostructures. *Nature communications* **2014,** *5* (1), 1-6.
85. Pereira, Z.; Da Silva, E., Cold welding of gold and silver nanowires: a molecular dynamics study. *The Journal of Physical Chemistry C* **2011,** *115* (46), 22870-22876.
86. Lu, Y.; Huang, J. Y.; Wang, C.; Sun, S.; Lou, J., Cold welding of ultrathin gold nanowires. *Nat. Nanotechnol.* **2010,** *5* (3), 218-224.
87. Wagle, D. V.; Baker, G. A., Cold welding: a phenomenon for spontaneous self-healing and shape genesis at the nanoscale. *Materials Horizons* **2015,** *2* (2), 157-167.
88. Calderon, I.; Alvarez-Puebla, R. A.; Pazos-Perez, N., Gold-spiked coating of silver particles through cold nanowelding. *Nanoscale* **2021,** *13* (8), 4530-4536.
89. Encina, E. R.; Coronado, E. A., Plasmon Coupling in Silver Nanosphere Pairs. *J. Phys. Chem. C* **2010,** *114* (9), 3918-3923.
90. Le Ru, E. C.; Etchegoin, P. G., Quantifying SERS enhancements. *MRS bulletin* **2013,** *38* (8), 631-640.
91. Le Ru, E. C.; Galloway, C.; Etchegoin, P. G., On the connection between optical absorption/extinction and SERS enhancements. *Phys. Chem. Chem. Phys.* **2006,** *8* (26), 3083-3087.
92. Bell, S. E. J.; Sirimuthu, N. M. S., Surface-enhanced Raman spectroscopy (SERS) for sub-micromolar detection of DNA/RNA mononucleotides. *J. Am. Chem. Soc.* **2006,** *128* (49), 15580-15581.
93. Turino, M.; Pazos-Perez, N.; Guerrini, L.; Alvarez-Puebla, R. A., Positively-charged plasmonic nanostructures for SERS sensing applications. *RSC Adv.* **2022,** *12* (2), 845-859.
94. Pazos-Perez, N.; Fitzgerald, J. M.; Giannini, V.; Guerrini, L.; Alvarez-Puebla, R. A., Modular assembly of plasmonic core–satellite structures as highly brilliant SERS-encoded nanoparticles. *Nanoscale Advances* **2019,** *1* (1), 122-131.
95. Kotov, N. A.; Dekany, I.; Fendler, J. H., Layer-by-layer self-assembly of polyelectrolyte-semiconductor nanoparticle composite films. *The Journal of Physical Chemistry* **1995,** *99* (35), 13065-13069.
96. Guerrini, L.; Rodriguez-Loureiro, I.; Correa-Duarte, M. A.; Lee, Y. H.; Ling, X. Y.; De Abajo, F. J. G.; Alvarez-Puebla, R. A., Chemical speciation of heavy metals by surface-enhanced Raman scattering spectroscopy: identification and quantification of inorganic-and methyl-mercury in water. *Nanoscale* **2014,** *6* (14), 8368-8375.

97. Hu, X.; Cheng, W.; Wang, T.; Wang, Y.; Wang, E.; Dong, S., Fabrication, characterization, and application in SERS of self-assembled polyelectrolyte− gold nanorod multilayered films. *The Journal of Physical Chemistry B* **2005,** *109* (41), 19385-19389.
98. Ung, T.; Liz-Marzán, L. M.; Mulvaney, P., Optical properties of thin films of Au@ SiO2 particles. *The Journal of Physical Chemistry B* **2001,** *105* (17), 3441-3452.
99. Mir-Simon, B.; Morla-Folch, J.; Gisbert-Quilis, P.; Pazos-Perez, N.; Xie, H.-n.; Bastús, N. G.; Puntes, V.; Alvarez-Puebla, R., A. ; Guerrini, L., SERS efficiencies of micrometric polystyrene beads coated with gold and silver nanoparticles: the effect of nanoparticle size. *J. Optics* **2015,** *17* (11), 114012.
100. Spuch-Calvar, M.; Rodriguez-Lorenzo, L.; Morales, M. P.; Alvarez-Puebla, R. A.; Liz-Marzan, L. M., Bifunctional nanocomposites with long-term stability as SERS optical accumulators for ultrasensitive analysis. *The Journal of Physical Chemistry C* **2009,** *113* (9), 3373-3377.
101. Guerrini, L.; Alvarez-Puebla, R. A., Surface-enhanced Raman scattering sensing of transition metal ions in waters. *ACS omega* **2021,** *6* (2), 1054-1063.
102. Howes, B. D.; Guerrini, L.; Sanchez-Cortes, S.; Marzocchi, M. P.; Garcia-Ramos, J. V.; Smulevich, G., The influence of pH and anions on the adsorption mechanism of rifampicin on silver colloids. *Journal of Raman Spectroscopy: An International Journal for Original Work in all Aspects of Raman Spectroscopy, Including Higher Order Processes, and also Brillouin and Rayleigh Scattering* **2007,** *38* (7), 859-864.
103. Garcia-Rico, E.; Alvarez-Puebla, R. A.; Guerrini, L., Direct surface-enhanced Raman scattering (SERS) spectroscopy of nucleic acids: from fundamental studies to real-life applications. *Chemical Society Reviews* **2018,** *47* (13), 4909-4923.
104. Cotton, T. M.; Schultz, S. G.; Van Duyne, R. P., Surface-enhanced resonance Raman scattering from cytochrome c and myoglobin adsorbed on a silver electrode. *Journal of the American Chemical Society* **1980,** *102* (27), 7960-7962.
105. Kuligowski, J.; El-Zahry, M. R.; Sánchez-Illana, Á.; Quintás, G.; Vento, M.; Lendl, B., Surface enhanced Raman spectroscopic direct determination of low molecular weight biothiols in umbilical cord whole blood. *Analyst* **2016,** *141* (7), 2165-2174.
106. Fabris, L., SERS tags: the next promising tool for personalized cancer detection? *ChemNanoMat* **2016,** *2* (4), 249-258.
107. Giles, N. M.; Watts, A. B.; Giles, G. I.; Fry, F. H.; Littlechild, J. A.; Jacob, C., Metal and Redox Modulation of Cysteine Protein Function. *Chem. Biol.* **2003,** *10* (8), 677-693.
108. Estrela, J. M.; Ortega, A.; Obrador, E., Glutathione in cancer biology and therapy. *Critical Reviews in Clinical Laboratory Sciences* **2006,** *43* (2), 143-181.
109. Saharan, S.; Mandal, P. K., The Emerging Role of Glutathione in Alzheimer's Disease. *Journal of Alzheimers Disease* **2014,** *40* (3), 519-529.
110. Bajic, V. P.; Van Neste, C.; Obradovic, M.; Zafirovic, S.; Radak, D.; Bajic, V. B.; Essack, M.; Isenovic, E. R., Glutathione "redox homeostasis" and its relation to cardiovascular disease. *Oxidative medicine and cellular longevity* **2019,** *2019*.
111. Ozben, S.; Kucuksayan, E.; Koseoglu, M.; Erel, O.; Neselioglu, S.; Ozben, T., Plasma thiol/disulphide homeostasis changes in patients with relapsing-remitting multiple sclerosis. *International Journal of Clinical Practice* **2021,** *75* (7), e14241.
112. Vural, G.; Gumusyayla, S.; Bektas, H.; Deniz, O.; Alisik, M.; Erel, O., Impairment of dynamic thiol–disulphide homeostasis in patients with idiopathic Parkinson's disease and its relationship with clinical stage of disease. *Clinical neurology and neurosurgery* **2017,** *153*, 50-55.
113. Sánchez-Illana, A. n.; Mayr, F.; Cuesta-García, D.; Piñeiro-Ramos, J. D.; Cantarero, A. s.; Guardia, M. d. l.; Vento, M. x.; Lendl, B.; Quintás, G.; Kuligowski, J., On-capillary surface-enhanced Raman spectroscopy: determination of glutathione in whole blood microsamples. *Analytical chemistry* **2018,** *90* (15), 9093-9100.
114. Lv, M.; Gu, H.; Yuan, X.; Gao, J.; Cai, T., Investigation of 3D silvernanodendrite@glass as surface-enhanced Raman scattering substrate for the detection of Sildenafil and GSH. *Journal of Molecular Structure* **2012,** *1029*, 75-80.
115. Picquart, M.; Grajcar, L.; Baron, M. H.; Abedinzadeh, Z., Vibrational spectroscopic study of glutathione complexation in aqueous solutions. *Biospectroscopy* **1999,** *5* (6), 328-337.
116. Kong, J.; Yu, S., Fourier transform infrared spectroscopic analysis of protein secondary structures. *Acta biochimica et biophysica Sinica* **2007,** *39* (8), 549-59.
117. Guerrini, L.; Pazos-Perez, N.; Garcia-Rico, E.; Alvarez-Puebla, R., Cancer characterization and diagnosis with SERS-encoded particles. *Cancer Nanotechnol.* **2017,** *8* (1), 5.

118. Pazos-Perez, N.; Pazos, E.; Catala, C.; Mir-Simon, B.; Gómez-de Pedro, S.; Sagales, J.; Villanueva, C.; Vila, J.; Soriano, A.; García de Abajo, F. J., Ultrasensitive multiplex optical quantification of bacteria in large samples of biofluids. *Scientific reports* **2016,** *6* (1), 1-10.
119. Guerrini, L.; Alvarez-Puebla, R. A., Surface-enhanced Raman scattering chemosensing of proteins. In *Vibrational Spectroscopy in Protein Research*, Ozaki, Y.; Baranska, M.; Lednev, I. K.; Wood, B. R., Eds. Academic Press: **2020**; pp 553-567.
120. Guerrini, L.; Pazos, E.; Penas, C.; Vázquez, M. E.; Mascareñas, J. L.; Alvarez-Puebla, R. A., Highly Sensitive SERS Quantification of the Oncogenic Protein c-Jun in Cellular Extracts. *J. Am. Chem. Soc.* **2013,** *135* (28), 10314-10317.
121. Joo, T. H.; Kim, M. S.; Kim, K., SURFACE-ENHANCED RAMAN-SCATTERING OF BENZENETHIOL IN SILVER SOL. *J. Raman Spectrosc.* **1987,** *18* (1), 57-60.
122. Saikin, S. K.; Olivares-Amaya, R.; Rappoport, D.; Stopa, M.; Aspuru-Guzik, A., On the chemical bonding effects in the Raman response: Benzenethiol adsorbed on silver clusters. *Phys Chem Chem Phys* **2009,** *11* (41), 9401-11.
123. Li, C.; Chen, P.; Khan, I. M.; Wang, Z.; Zhang, Y.; Ma, X., Fluorescence–Raman dual-mode quantitative detection and imaging of small-molecule thiols in cell apoptosis with DNA-modified gold nanoflowers. *Journal of Materials Chemistry B* **2022,** *10* (4), 571-581.
124. Wang, P.; Nasir, M. E.; Krasavin, A. V.; Dickson, W.; Jiang, Y.; Zayats, A. V., Plasmonic metamaterials for nanochemistry and sensing. *Accounts of chemical research* **2019,** *52* (11), 3018-3028.
125. Cai, W.; Shalaev, V., Optical properties of metal-dielectric composites. In *Optical Metamaterials*, Springer: **2010**; pp 11-37.
126. Hedayati, M. K.; Faupel, F.; Elbahri, M., Review of Plasmonic Nanocomposite Metamaterial Absorber. *Materials* **2014,** *7* (2), 1221-1248.
127. Smith, D. R.; Pendry, J. B.; Wiltshire, M. C., Metamaterials and negative refractive index. *Science* **2004,** *305* (5685), 788-792.
128. Kabashin, A. V.; Evans, P.; Pastkovsky, S.; Hendren, W.; Wurtz, G. A.; Atkinson, R.; Pollard, R.; Podolskiy, V. A.; Zayats, A. V., Plasmonic nanorod metamaterials for biosensing. *Nature materials* **2009,** *8* (11), 867-871.
129. Wang, P.; Krasavin, A. V.; Nasir, M. E.; Dickson, W.; Zayats, A. V., Reactive tunnel junctions in electrically driven plasmonic nanorod metamaterials. *Nature nanotechnology* **2018,** *13* (2), 159-164.
130. Yao, K.; Liu, Y., Plasmonic metamaterials. *Nanotechnology Reviews* **2014,** *3* (2), 177-210.
131. Huh, J. H.; Kim, K.; Im, E.; Lee, J.; Cho, Y.; Lee, S., Exploiting colloidal metamaterials for achieving unnatural optical refractions. *Advanced Materials* **2020,** *32* (51), 2001806.
132. Kim, K.; Yoo, S.; Huh, J.-H.; Park, Q. H.; Lee, S., Limitations and Opportunities for Optical Metafluids To Achieve an Unnatural Refractive Index. *ACS Photonics* **2017,** *4* (9), 2298-2311.
133. Yoo, S.; Park, Q.-H., Effective permittivity for resonant plasmonic nanoparticle systems via dressed polarizability. *Optics Express* **2012,** *20* (15), 16480-16489.
134. Kock, W. E., Metallic delay lenses. *Bell System Technical Journal* **1948,** *27* (1), 58-82.
135. Faupel, F.; Zaporojtchenko, V.; Strunskus, T.; Elbahri, M., Metal-polymer nanocomposites for functional applications. *Advanced engineering materials* **2010,** *12* (12), 1177-1190.
136. Zou, S.; Janel, N.; Schatz, G. C., Silver nanoparticle array structures that produce remarkably narrow plasmon lineshapes. *The Journal of chemical physics* **2004,** *120* (23), 10871-10875.
137. Gansel, J. K.; Thiel, M.; Rill, M. S.; Decker, M.; Bade, K.; Saile, V.; von Freymann, G.; Linden, S.; Wegener, M., Gold helix photonic metamaterial as broadband circular polarizer. *Science* **2009,** *325* (5947), 1513-1515.
138. Ross, M. B.; Mirkin, C. A.; Schatz, G. C., Optical properties of one-, two-, and three-dimensional arrays of plasmonic nanostructures. *The journal of physical chemistry C* **2016,** *120* (2), 816-830.
139. Lee, S., Colloidal superlattices for unnaturally high-index metamaterials at broadband optical frequencies. *Optics Express* **2015,** *23* (22), 28170-28181.
140. Lauri, A.; Velleman, L.; Xiao, X.; Cortés, E.; Edel, J. B.; Giannini, V.; Rakovich, A.; Maier, S. A., 3D confocal Raman tomography to probe field enhancements inside supercluster metamaterials. *ACS Photonics* **2017,** *4* (8), 2070-2077.

Chapter 2

Design and Fabrication of Bimetallic Plasmonic Colloids through Cold Nanowelding

Design and Fabrication of Bimetallic Plasmonic Colloids through Cold Nanowelding

Here, a thorough study on the cold-welding process of silver nanoparticles onto gold substrates is performed to gain a better understanding of the role of different parameters in enabling the formation of well-defined bimetallic structures that retain the original gold substrate morphology. To this end, some variables such as the silver nanoparticles size, gold substrate dimensions and geometries, solvent polarity and structural nature of the polymeric coating were systematically varied. A wide range of optical and microscopy techniques have been used to provide a complementary and detailed description of the nanowelding process. This extensive study will provide valuable insights into the optimal design and engineering of bimetallic plasmonic Ag/Au structures for application in nanodevices.

This work has been published in:

Nanoscale, 14, 9439-9447, 2022 (DOI: 10.1039/D2NR02092K)
"Design and fabrication of bimetallic plasmonic colloids through cold nanowelding"
Mariacristina Turino; Enrique Carbó-Argibay; Miguel Correa-Duarte; Luca Guerrini; Nicolas Pazos-Perez and Ramon A. Alvarez-Puebla

2.1 Introduction

As previously discussed in Chapter 1, section 1.4, the integration of Au and Ag into nanoalloys has emerged as an intriguing strategy to further tailor and boost the plasmonic properties of optical substrates.[1, 2, 3] Conventional approaches to fabricate these materials via chemical reductions of metal salts in solution suffer from some limitations, such as the possibility of retaining the original morphology of the monometallic substrate.[1, 2, 3] Spontaneous nanowelding at room temperature has emerged as an alternative route to tailor Au/Ag nanomaterials.[4, 5, 6, 7]

In this chapter, it is presented a thorough study on the cold-welding of small spherical AgNPs (diameter size < ca. 40 nm) over a diverse range of gold nanomaterials of various dimensions and shapes to yield bimetallic structures retaining the original gold substrate morphologies. This was achieved independently of the gold substrate initial features via a homogeneous silver coating. Importantly, key parameters that affect the evolution of the nanowelding process, such as AgNPs diameter, AgNPs surface density, solvent polarity, and Au nanostructure geometrical characteristics (e.g., surface curvature) were investigated. SERS was also used as an efficient characterization tool for monitoring nanowelding, an application of this technique that has been largely underexploited so far.[8, 9] This work is intended to gain a better understanding of the role of different variables in enabling the formation of well-defined bimetallic structures that retain the original gold substrate morphology.

2.2 Experimental section

2.2.1 Materials

Tetrachloroauric acid (≥99%, $HAuCl_4 \cdot 3H_2O$), trisodium citrate dihydrate (≥99.5%, $C_6H_5Na_3O_7 \cdot 2H_2O$), ascorbic acid (99%, $C_6H_8O_6$), silver nitrate (99,8%, $AgNO_3$), n-hexane (≥99.5%, C_6H_{14}), chloroform (≥99%, $CHCl_3$), and oleylamine (90%, OA) were acquired from Acros Organics. Triisopropylsilane (98%, TIPS) was purchased from Alfa Aesar. Branched polyethyleneimine (≥99.5%, PEI), iron nitrate nonahydrate (≥99.5%, $FeN_3O_9 \cdot 9H_2O$), cetyltrimethylammonium bromide (99.72%, CTAB), and sodium borohydride (99%, $NaBH_4$), poly(allylamine hydrochloride) (PAH, molecular weight = 17.5 k), poly(diallyldimethylammonium chloride) solution 20 wt. % in H_2O (PDDA, medium molecular weight = 200-350 k), were purchased from Sigma-Aldrich. Ethanol was acquired from Scharlab (≥99%, C_2H_5OH). All reactants were used without further purification. Milli-Q water (18 MΩ cm^{-1}) was used in all aqueous solutions. All glassware was cleaned with aqua regia before use.

2.2.2 Synthesis of ultrathin gold nanowires

To synthesize 10 mL of ultrathin gold nanowires, 0.4 mL of OA were mixed with 12 mg of $HAuCl_4$ in 10 mL of hexane. Followed by the addition of 0.6 mL TIPS, the solution turns from transparent to yellow. The mixture was left reacting overnight at room temperature. No stirring is required. The reaction turns into brownish color suggesting the formation of thin nanowires structures. After that, 20 mL of ethanol were added and the mixture was centrifugated one time (4000 rpm, 4 min). The final precipitate was redispersed in 10 mL of chloroform.[10, 11]

2.2.3 Assembly of nanowires in bundles and PEI wrapping

The obtained nanowires were mixed with 8 mL of a PEI solution in chloroform (0.01g/10mL). The mixture was left flocculating overnight and then centrifuged twice (4000 rpm, 4 min). The pellet constituted by nanowires assembled into bundles was redispersed in 20 mL of ethanol for further characterization and storage. 500 µL of the so-obtained bundles were added drop by drop to an ethanol solution of PEI (0.02g/10 mL). After two hours in the wheel, the sample was centrifuged twice (4000 rpm, 4 min) and the so obtained positively charged bundles were redispersed in 500 µL of H_2O.

2.2.4 Synthesis of spherical silver nanoparticles (ca. 33 and 43 nm diameter)

To synthesize spherical AgNPs of ca. 30 nm, 100 mL of H_2O, were heated. Once boiling, a mixture containing AA (100 µL, 0.1 M) and $C_6H_5Na_3O_7 \cdot 2H_2O$ (600 µL, 0.1 M) was added under

vigorous stirring. 1 minute later, a solution of $AgNO_3$ (198 µL, 0.1 M) and $FeN_3O_9 \cdot 9H_2O$ (22 µL, 0.001 M), previously incubated for 5 minutes, was also added.[12] Upon the addition, the color of the solution quickly turns yellow and gradually stabilizes into orange-greenish. Boiling and stirring were continued for 1 h. The samples were concentrated until reaching a final Ag^0 concentration of 10^{-3} M (ø 33 ± 3 nm). To produce AgNPs of ca. 43 nm in diameter, the same synthesis was followed adjusting the amounts of the reagents. A mixture containing 100 µL of AA 0.1 M and 908 µL $C_6H_5Na_3O_7 \cdot 2H_2O$ 0.1 M were added to 100 mL of boiling H_2O. After 1 minute, $AgNO_3$ (298 µL, 0.1 M) was also injected. The reaction turns from colorless to white-greenish. The solution was left for 1h under energetically stirring and heated until reaching a Ag^0 concentration of 10^{-3} M (ø 43 ± 4 nm).

2.2.5 Synthesis of CTAB-stabilized gold nanorods and PEI wrapping

Gold nanorods of high aspect ratios were produced by adapting a previously published seed-mediated method.[13, 14, 15] Briefly, gold seeds were synthesized by adding to 5 mL of H_2O, 12,75 µL of $C_6H_5Na_3O_7 \cdot 2H_2O$ 0.1 M. Then 12.18 µL of $HAuCl_4$ 0.1 M were also added under vigorous stirring. Next, a freshly prepared solution of $NaBH_4$ (150 µL, 0.1 M) was quickly injected. The color of the solution immediately changes from light yellow to red. The mixture was let under vigorous stirring for 1h in an open atmosphere to ensure complete decomposition of unreacted $NaBH_4$. Then, a growth solution was prepared by dissolving 9.1112 g of CTBA in 250 mL of H_2O. To the latter, 1.218 mL of $HAuCl_4$ 0.1 M were mixed and gently shaken until complete dissolution. The solution color turned from orange to transparent upon injection of 1.837 mL of AA 0.1 M. After that, 500 µL of seeds were carefully added into the foam of the growth solution. The mixture was left undisturbed for 24 h at 27 °C. Sediment made by high aspect ratio nanorods slowly set in the bottom of the flask and thus can be easily separated from the supernatant containing mainly spheres. The collected pellet was washed several times by sedimentation to ensure the removal of spherical NPs and finally redispersed in 40 mL of CTAB 0.1M. With the final aim to increase the particle size, a second seeding-growth step was carried out using the obtained nanorods as seeds. A new growth solution was prepared by adding 20 mL of CTAB 0.1 M, 24.36 µL of $HAuCl_4$ 0.1 M. Once completely dissolution of the gold salt, 73.5 µL of AA 0.1 M were injected and 100 µL of nanorods previously synthesized were introduced in the foam of the solution. After vigorously shaking, the growth mixture was left undisturbed overnight. The, grown nanorods were washed twice by centrifugation and stored in CTAB 0.1 M for further use (length: 1085 ± 114 nm; width: 94 ± 15 nm). To wrap the nanorods with PEI, 500 µL of the overgrown nanorods, were added dropwise to 5 mL of a PEI solution (2 mg/mL) under vigorous stirring. After 3 hours, the mixture was washed once, the pellet was redispersed in 500 µL of

water and added again drop by drop to 5 mL of PEI solution (2 mg/mL). The mixture was left overnight under stirring to ensure the complete surfactant-polymer exchange. After that, particles were washed five times and finally redispersed in 1 mL of water.

2.2.6 Growth of CTAB-stabilized gold nanospheres and PEI wrapping

Gold nanospheres of 100 and 200 nm approximately were obtained using gold nanospheres of Ø 70 nm as seeds. To a solution of CTAB 0.1 M (10 mL), 49 µL of $HAuCl_4$ 0.1 M were added. Once completely dissolved, 74 µL of AA 0.1 M were fastly injected. Then, 600 µL and 4.8 mL of gold nanospheres of 70 nm were added to the foam of the mixtures. The solutions were vigorously shaken and left undisturbed overnight at room temperature. Upon sedimentation, pellets were recollected, washed twice, and finally redispersed in 10 mL of CTAB 0.1 M. Highly monodisperse spheroidal gold particles of 107 ± 6 nm and 200 ± 10 nm respectively were obtained.[15] 1 mL of the so-fabricated nanospheres of both diameters, were washed twice and wrapped with 5 mL of PEI solution (2 mg/mL) under vigorous stirring. The mixtures were let with positively charged polymer overnight under stirring. Nanospheres were then washed five times and redispersed in 1 mL of water.

2.2.7 Synthesis of small spherical silver nanoparticles (ca. 15 nm diameter)

Spherical Ag nanoparticles of approx. 15 nm diameter were synthesized by adding to 100 mL of boiling water, a mixture containing AA (100 µL, 0.1 M) and sodium citrate (600 µL, 0.1 M) under vigorous magnetic stirring. After 1 min, a solution incubated for 5 minutes containing 198 µL of $AgNO_3$ 0.1 M and 79 µL of $Fe(NO_3)_3$ 0.01 M was also added. The color turns from transparent to dark red and finally to bright yellow.[12] After 1 h, the samples were concentrated by solvent evaporation until reaching a final Ag^0 concentration of 10^{-3} M. The NPs size was 15 ± 2 nm.

2.2.8 Assembly of spherical Ag nanoparticles onto PEI coated NPs

Au bundles were coated with Ag nanoparticles (ca. 33 and 43 nm diameters) by the dropwise addition of 500 µL of the PEI-covered nanowires to 5 mL of Ag colloids. Nanoparticle suspensions were previously washed once. The mixtures were left overnight and washed one time with water to remove the excess of unbound AgNPs. Finally, the core-satellites assemblies were redispersed in 1.5 mL of water or 1.5 mL of ethanol for TEM and UV-Vis characterization. Small AgNPs were assembled onto gold nanorods and gold spheres in a similar manner. 1 mL of PEI wrapped gold NPs were added dropwise and under sonication to 5 mL of 15 nm size AgNPs solutions (previously washed once). The core-satellites nanostructures were left to sediment and the

recovered pellet was washed once with water and finally redisperse in 1 mL of water for storage and further characterization.[14]

2.2.9 Characterization

Microscopy. Transmission electron microscope (TEM) micrographs were acquired using JEOL 1011 scanning transmission electron microscope operating at 80 kV. The elemental composition of samples was analyzed employing a FEI Titan Themis Cubed (Probe- and Image-corrected TEM) operating at 200 kV mapped by energy-dispersive X-ray (EDX) spectroscopy. Samples were prepared by drying water suspensions on carbon−Formvar-coated 200 mesh copper grid.

UV-Visible spectroscopy. UV-Vis characterization was carried out using a Thermo Scientific Evolution 201 UV-visible spectrophotometer.

SERS spectroscopy. SERS measurements were performed using a Renishaw InVia Reflex confocal microscope equipped with a 2D-CCD detector and a Leica confocal microscope. 514, 633, and 785 nm laser lines were focused on the sample through a ×50 objective with an acquisition time of 10 s and the power at the sample of about 2.6 mW. The provided spatial resolution was ca. 1 µm obtaining SERS maps under the same conditions in an area of 50 × 50 µm. Samples were prepared using 50 µL of colloidal suspensions (i.e., individual Au cores and Ag satellites, or the assembled core-satellite composites at different stages of the welding process) deposited onto a previously RCA cleaned glass slide and spin-coated ((1st ramp) 500 rpm, 10 s; (2nd ramp) 3000 rpm, 30 s, with an acceleration rate of 500 rpm s^{-1} for both ramps) to assure individual structures SERS measurements. Finally, the materials were exposed to benzenethiol in the gas phase (overnight incubation).

2.3 Results and discussion

Cold-welding involving ultrathin metallic nanowires (NWs) has been intensively investigated in recent years as a valuable tool to promote nanojoining processes for designing nanodevices.[6, 16, 17, 18] Thus, the present study was initiated using this class of materials by fabricating ca. 1.6 nm diameter Au nanowires (NWs) according to a previously described protocol.[11] Subsequently, the ultrathin structures (Figure 2.1 (top) and Figure 2.3A) were functionalized with PEI promoting the extensive formation of heterogeneous bundles of wires as illustrated in Figure 2.1 (bottom) and 2.3B. NWs self-assembly into close-packed bundles is commonly used to prevent structural fragmentation.[19]

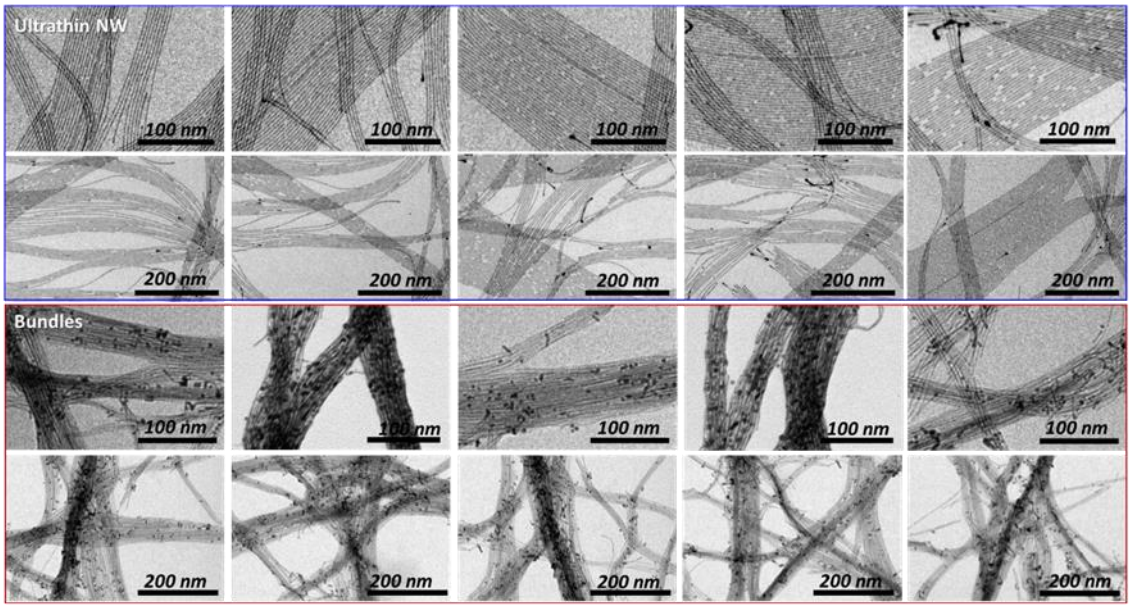

Figure 2.1. TEM images of the as-synthesized ultrathin Au nanowires (top). TEM images of the Au bundles formed after PEI coating (bottom).

The PEI functionalization also allows the transfer of the wires to an aqueous solution while imparting an overall positive charge. Such positive charge is further exploited to promote the following adhesion of negatively charged citrate-capped silver nanoparticles of 33 ± 3 nm ($AgNP_{33}$, Figure 2.2 and Figure 2.3C) to yield the corresponding bundle@$AgNP_{33}$ composite materials (Figure 2.3D).

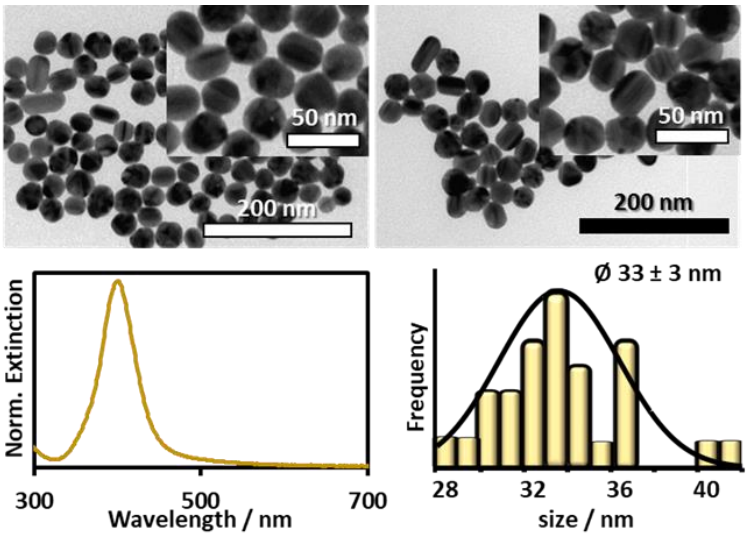

Figure 2.2. Representative TEM images, extinction spectrum, and size histogram distribution of the negatively charged citrate-capped silver nanoparticles of 33 ± 3 nm diameter ($AgNP_{33}$).

After 1 day upon the assembly, bundles and NPs appear as well-separated independent units (Figure 2.3D and Figure 2.4A). After 4 days, however, nanoparticles appear to begin merging with the Au bundles (Figure 2.3E and Figure 2.4B). The fusion becomes more prominent on day 7 (Figure 2.3F) and, after 11 days, the silver structures are almost completely integrated into the wire support, although their semispherical shapes can still be distinguished (Figure 2.3G). Three days later (Figure 2.3H and Figure 2.4C), metallic Ag has been completely embedded within the bundles, leading to the formation of a thicker wire as a result of the atomic diffusion of silver along the gold surfaces. After this period, the structure does not show any further visible alteration (Figure 2.3I and Figure 2.4D).

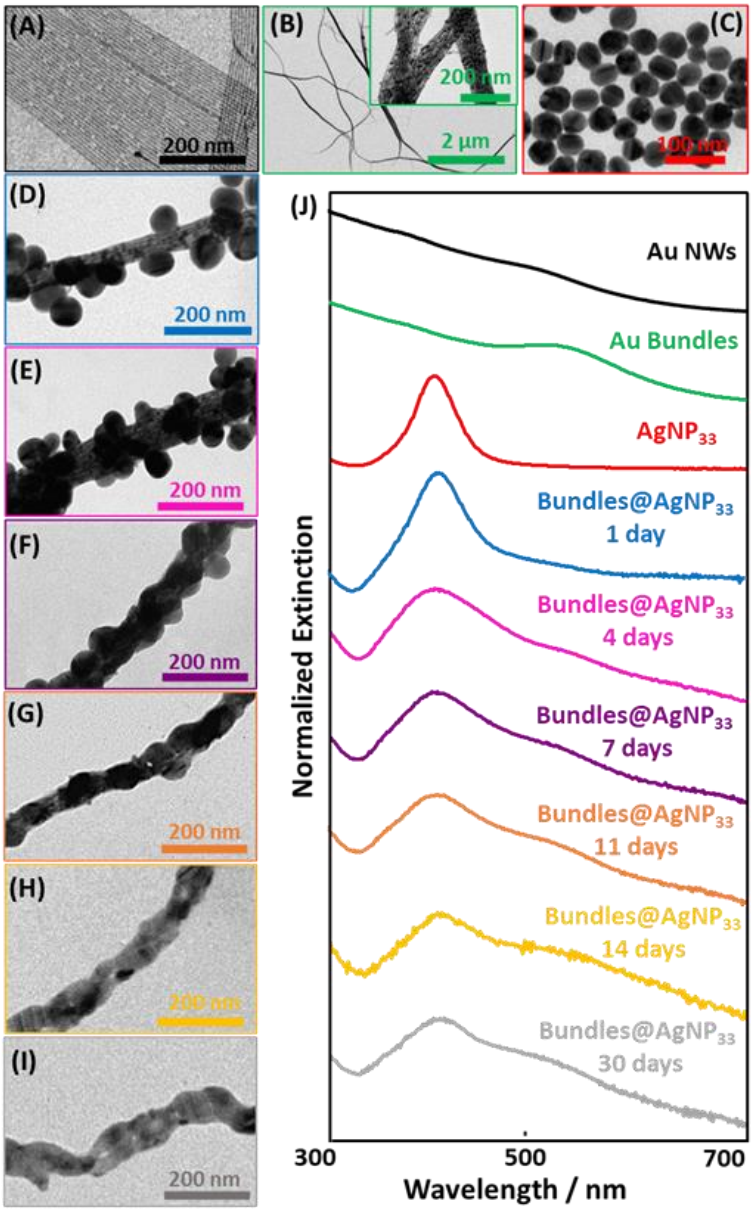

Figure 2.3. (A-C) Representative TEM images of the initial components of the assemblies (A) ultrathin gold nanowires (AuNWs), (B) bundles of gold nanowires, and (C) silver nanoparticles of 33 ± 3 nm diameter ($AgNP_{33}$). (D-I) Representative TEM images of the bundle@$AgNP_{33}$ assemblies at different stages of the welding process (1, 4, 7, 11, 14 and 30 days, from D to I, respectively). (J) Extinction spectra of individual AuNWs, Au bundles and $AgNP_{33}$ suspensions, and the bundle@$AgNP_{33}$ assemblies over time. The intensity of the stacked extinction spectra was adjusted for better visualization.

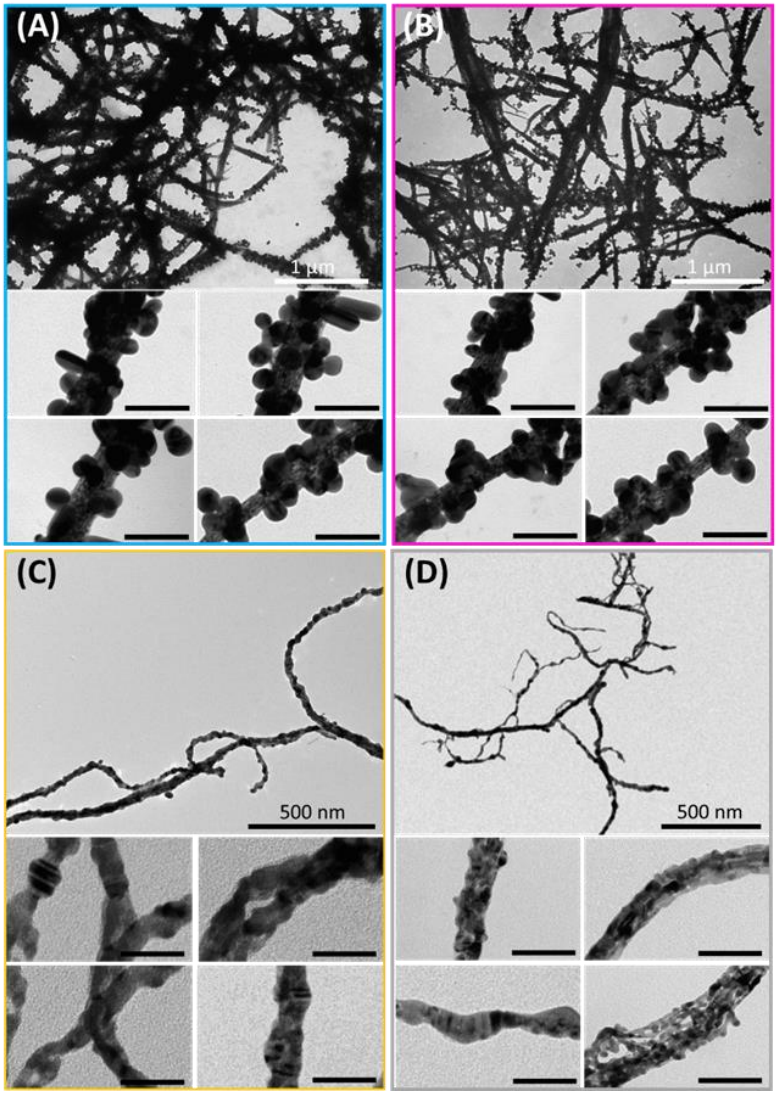

Figure 2.4. Additional TEM images of bundle@AgNP$_{33}$ at different stages of the welding process: (A) 1 day, (B) 4 days, (C) 14 days, and (D) 30 days. When otherwise indicated, scale bar = 100 nm.

Scanning transmission electron microscopy (STEM) combined with spectroscopic mapping by energy-dispersive X-ray (EDX) spectroscopy was also performed on representative bundle@AgNP$_{33}$ to monitor the elemental distribution during the cold-welding process (Figure 2.5). The elemental maps show the distribution of protruding spherical-like areas of Ag along a linear Au backbone (day 4). As the process continues (from day 7 onward), the bulging areas of high Ag density, as well as the residual interparticle gaps, progressively disappear, as the Ag incorporation into the bundle structure advances. Upon 14 days of the initial assembly, Ag and Au are homogeneously distributed over the whole structure which exhibits a core/shell structure (Au@Ag) with segregation of both elements (depicted from the line scan analysis shown in Figure 2.6).

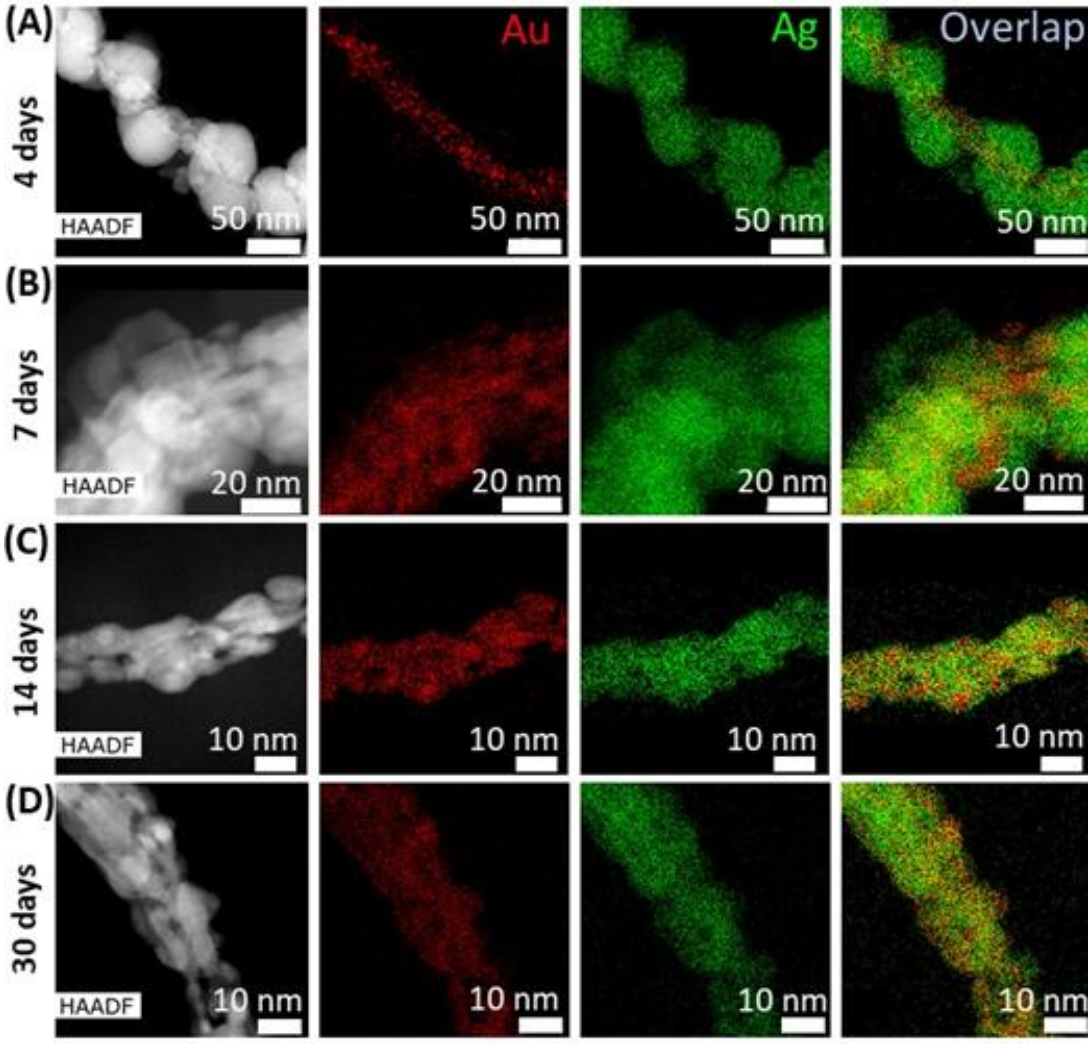

Figure 2.5. (A-D) Representative high-angle annular dark-field scanning transmission electron microscopy (HAADF-STEM) images of the bundle@$AgNP_{33}$ welding process at different stages (4, 7, 14 and 30 days). The images shown on the right of the figure are the corresponding elemental maps for Au and Ag (individual and overlapped) obtained via EDX analysis of the STEM images (A-D).

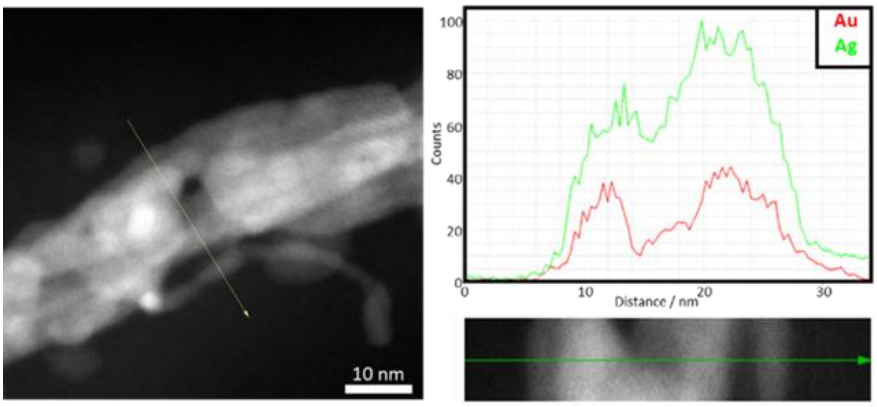

Figure 2.6. STEM image and EDX line scan analysis bundle@$AgNP_{33}$ after 14 days of welding showing how Ag and Au are homogeneously along the bundles in a core-shell configuration.

The qualitative information extracted from the TEM images and STEM-EDX characterization is mirrored by the optical interrogation of the whole ensemble of bundle@$AgNP_{33}$ in suspension. The normalized extinction spectra displayed in Figure 2.3J show that, after the initial assembly, the optical response is dominated by the feature at ca. 405 nm, assigned to the contribution of individual nanoparticle LSPRs with minimal interparticle coupling. After 4 days, this plasmonic feature undergoes significant broadening and drop in intensity, consistently with the reshaping of the surface-bound AgNPs. As a result, the weak contribution at 520 nm, associated with the LSPRs of the Au bundles, gains prominence in the spectral profile. The optical changes after day 4 are, however, very subtle, which can be related to the complex and heterogeneous bundle geometries which, in turn, difficult the discrimination of cold-welded induced structural changes.

Overall, these data demonstrate that AgNPs act as a soft matter that "wets" the hard gold core surface by the movement of Ag atoms over the bundle surface at room temperature.[4] This is also the reason why the gold structure retains its original morphology upon merging. On the other hand, it has been previously reported that welding of two NPs of similar size and shape that came into physical contact selectively occurs through a common lattice plane, which is an indication of an oriented attachment.[6, 20] Indeed, nanoparticles, differently from nanowires and nanofilms, can freely rotate to adjust the lattice structure which, in turn, paves the way for the natural cold welding process to occur. [21] In the specific case of cold welding between the NWs bundles and AgNPs, both materials have similar face center cubic lattice (FCC) arrangements with lattice parameters of 4.08 Å for Au and 4.09 Å for Ag,[5] showing inter-fringe distances of 0.23 nm and 0.24 nm. This corresponds to the (111) lattice spacing for both types of materials.[6] Therefore, the joint between Au bundles and AgNPs takes place via an oriented attachment mechanism as previously described,[6] where the AgNPs align through an atom-by-atom rearrangement of their crystallographic planes.

Remarkably, when transferred to ethanol, bundles@$AgNP_{33}$ assemblies exhibit minimal signs of AgNPs welding onto the gold surfaces even after 14 days (Figure 2.7). This phenomenon may be correlated to the reduction in solvent polarity when using ethanol in place of water. In fact, lowering the solvent polarity has been associated with a decrease in diffusion and solvation.[22]

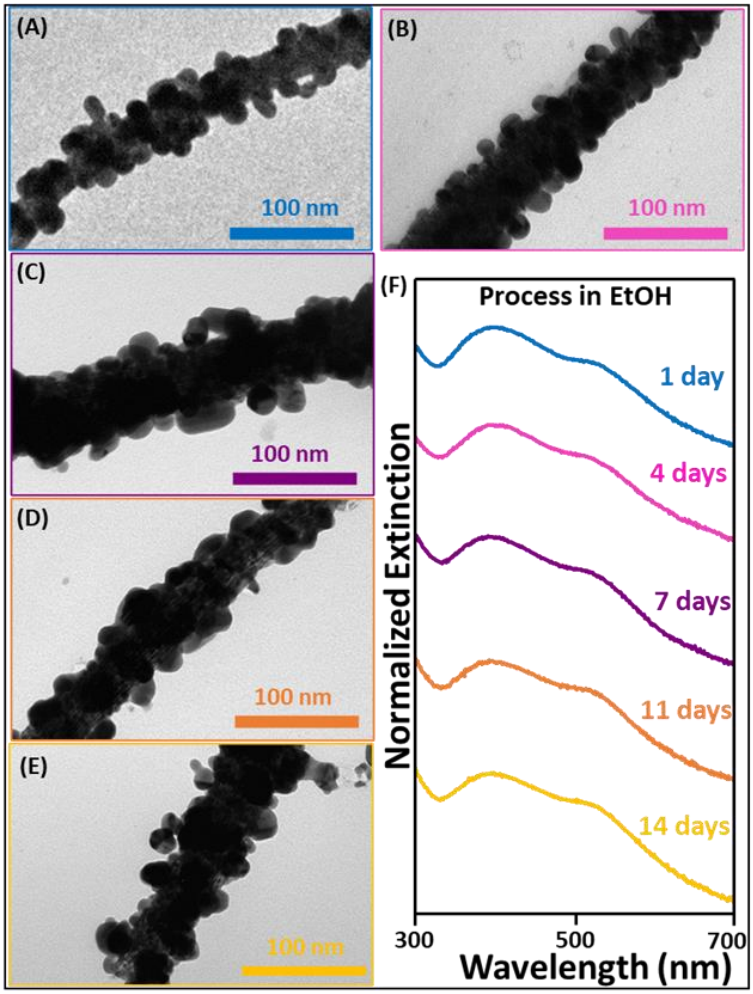

Figure 2.7. (A-E) Representative TEM images of the bundle@AgNP$_{33}$ assemblies at different stages of the welding process in ethanol (1, 4, 7, 11 and 14 days, from A to E, respectively). (F) Extinction spectra of the bundle@AgNP$_{33}$ assemblies over time. The intensity of the stacked extinction spectra was adjusted for better visualization.

In order to investigate the role of particle size in nanowelding process, nanoparticles of larger diameter (43 ± 4 nm, Figure 2.8) were synthesized and assembled onto Au bundles to obtain the corresponding bundle@AgNP$_{43}$. Surprisingly, it was observed that such an apparently small increase in nanoparticle size has a tremendous impact on the kinetic of the welding process. Indeed, even after 30 days, the 43 nm size AgNPs, while interconnected, still maintained a pseudo spherical shape resembling “pearls necklaces” (Figure 2.9) with no smoothing along the bundles of Au wires. This result clearly highlights the key role of AgNPs size in controlling the evolution of the welding and, thus, the homogeneous coating of the gold counterpart.

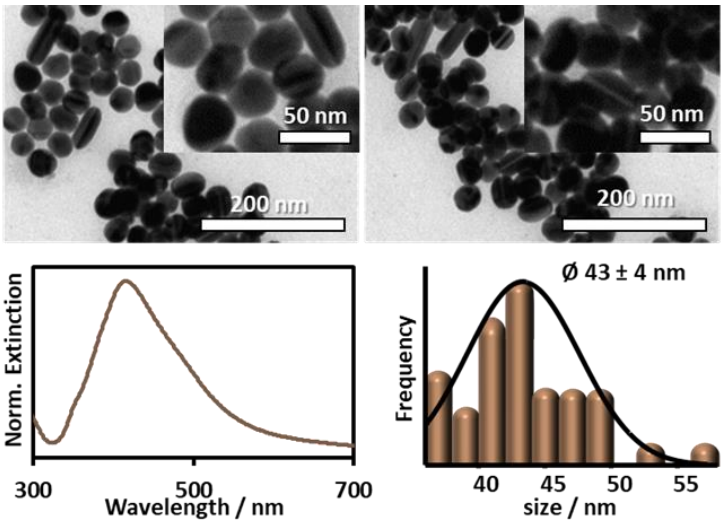

Figure 2.8. TEM images, extinction spectrum, and size histogram distribution of the negatively charged citrate-capped silver nanoparticles of 43 ± 4 nm ($AgNP_{43}$).

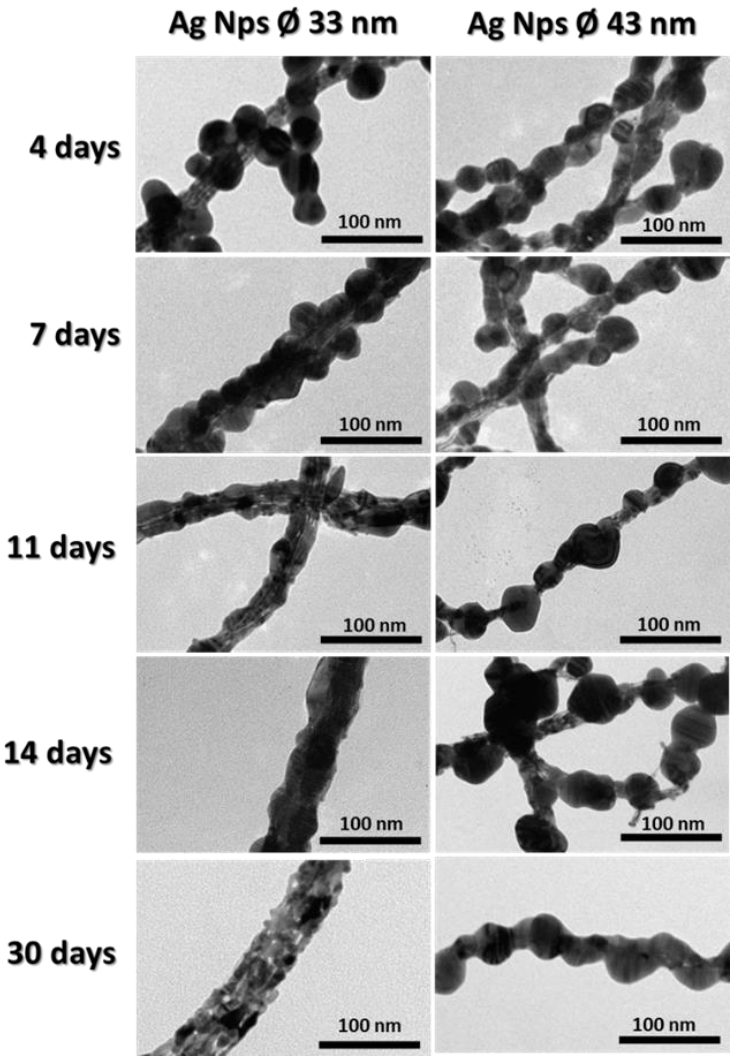

Figure 2.9. TEM images showing the comparison over time (4, 7, 11, 14, and 30 days) of bundle@AgNP assemblies using two different sizes (33 and 43 nm, left and right respectively) of AgNPs.

Based on these results, the study was subsequently focused on the welding process of AgNPs onto gold nanostructures by using (i) 15 ± 2 nm diameter silver nanoparticles ($AgNP_{15}$, Figure 2.10) as the smallest, colloidally stable, and homogeneous citrate-capped AgNPs currently available,[12] and (ii) uniform long Au nanorods (AuNRs, Figure 2.11). On the one hand, reducing the AgNPs size is expected to significantly fasten the merging process. On the other, a structurally heterogeneous gold material such as the bundles, was replaced with uniform penta-twined long AuNRs of ca. 94 nm width and ca. 1 µm in length to acquire a clearer view of the process.

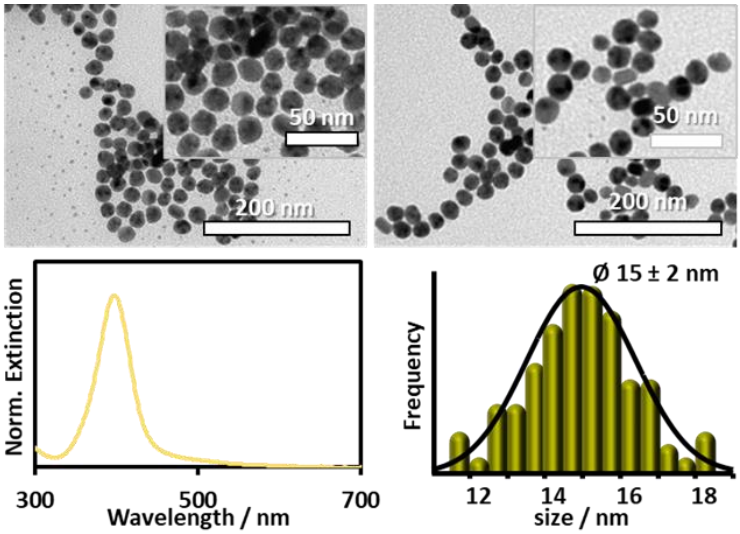

Figure 2.10. TEM images, extinction spectrum, and size histogram distribution of the negatively charged citrate-capped silver nanoparticles of 15 ± 2 nm ($AgNP_{15}$).

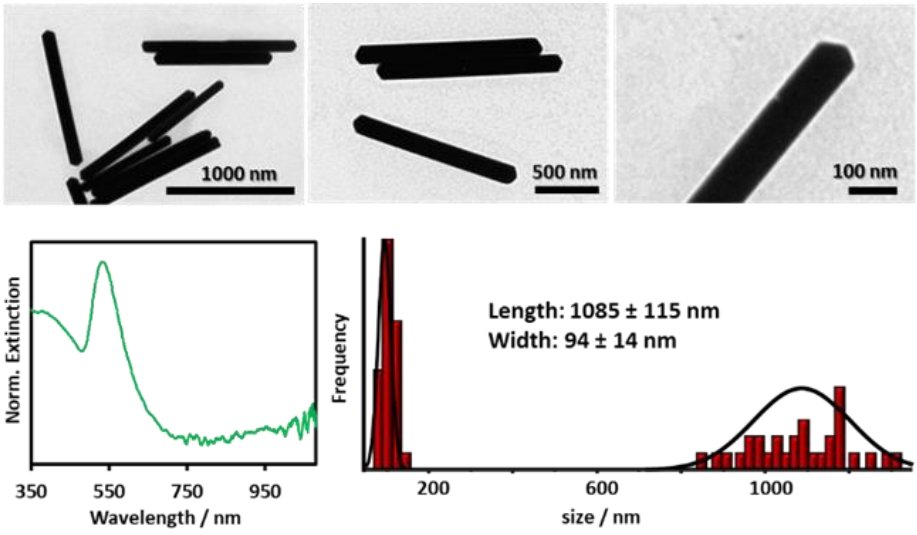

Figure 2.11. TEM images, extinction spectrum, and size histogram distribution of the as-synthesized AuNRs of 1085 ± 115 nm long and 94 ± 14 nm thick (AuNRs).

AuNRs were also wrapped with a PEI layer to trigger the electrostatic accumulation of $AgNP_{15}$ onto nanorods yielding $NR@AgNP_{15}$ materials. Representative TEM images acquired at different moments after the initial assembling (30 min, 1h, 3h, 6h,1 day, 2 days, and 6 days) are reported in Figure 2.12A-G and Figure 2.13A-D.

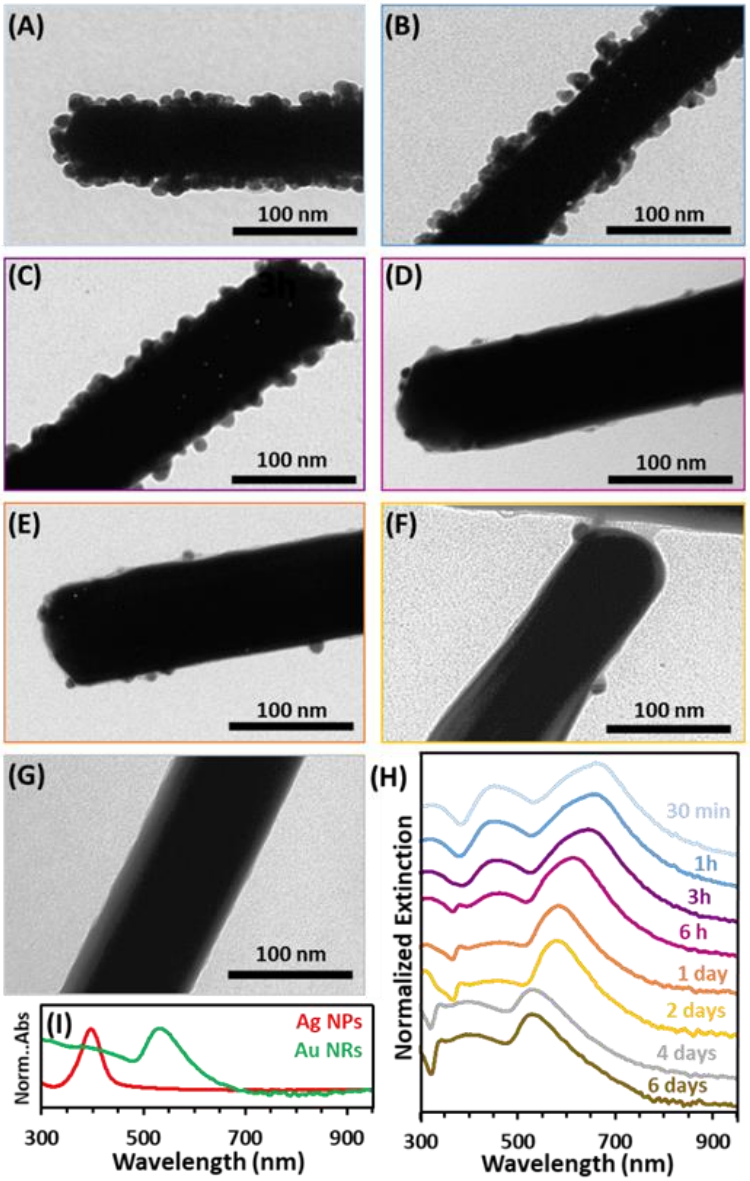

Figure 2.12. (A-G) Representative TEM images of $NR@AgNP_{15}$ assemblies at 7 different stages of the welding process (30 min, 1 h, 3 h, 6 h, 1 day, 2 days, and 4 days). (H) Extinction spectra of the assemblies over 6 days. (I) Extinction spectra of the individual AuNRs and $AgNP_{15}$ colloids. The stacked extinction spectra were normalized to their maxima for better visualization.

The dense collection of $AgNP_{15}$ on AuNRs begins to display indications of nanoparticle reshaping after just 1h (Figure 2.12B). At 3h total time (Figure 2.12C), the extension of the

welding process becomes more evident, as nanoparticles start merging and forming a continuous layer on the NR surfaces. At this stage, the welding process is largely completed although a flat and smooth silver coating is only achieved after approximately 4 days (Figure 2.12F,G and Figure 2.13D). This second stage of the process, driven by atomic diffusion along the side of the rods, exhibits lower kinetics as compared to the initial NPs merging. In this case, the monitoring of the optical properties of the well-defined NR@$AgNP_{15}$ materials during the welding process provides a clearer picture of the structural reshaping (Figure 2.12H) as compared to the bundle@AgNPs composites. At 30 min, the NR@$AgNP_{15}$ assemblies display two distinct peaks centered at ca. 400 nm and 660 nm. The first one is ascribed to the LSPR of AgNPs (Figure 2.12I) while the latter is assigned to the transversal mode of the NRs which is, however, redshifted as compared to the original AuNRs (535 nm) due to the plasmon coupling with AgNPs. As expected, as the welding proceeds, it was observed the progressive redshift and intensity decrease of Ag contribution until its full disappearance on day 1, due to NP merging. This is mirrored by the transversal NR contribution undergoing a continuous blueshift until ca. 525 nm (day 4), when the formation of a smooth Ag layer is completed. It is worth noticing that such transversal plasmon mode does not reach the value of the pristine AuNRs, in agreement with what was observed for shorter silver-coated gold nanorods obtained via chemical reduction of silver salts.[3]

NRs exhibit two different crystallographic planes at their surface: a five-fold cross-section made up of (111) facets and five (100) facets that run the length of the NRs.[13, 23, 24] Meanwhile, the AgNPs are multi-twinned particles with (111) facets facing the NRs surface. As seen from the TEM images in Figure 2.12 and Figure 2.13, welding occurs at both crystallographic planes of the NRs. At the tips, the AgNPs and AuNRs bound mainly through (111) facets whereas the welding along the rod length takes place between the (100) facets of the rods and the (111) facets of the AgNPs. The fact that any appreciable difference in the welding between the tips and the sides of the NRs it has been observed suggests that a non-crystallographic selective process has occurred.

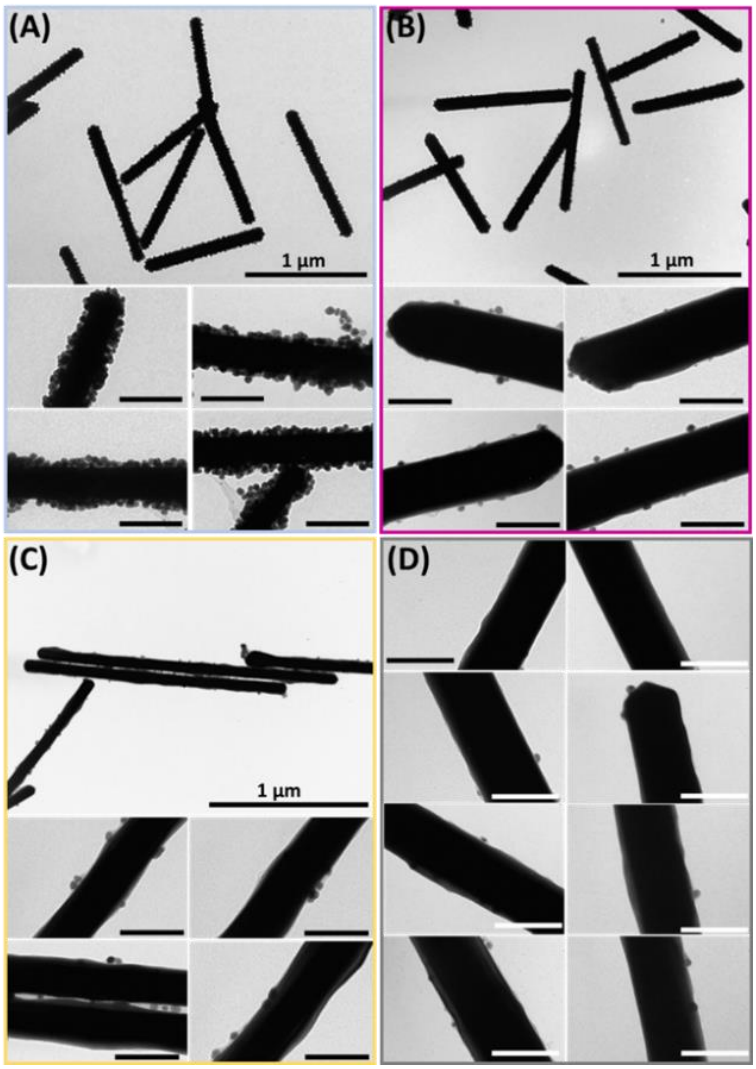

Figure 2.13. Additional TEM images of NR@AgNP$_{15}$ assemblies at different stages of the welding process: (A) 30 min, (B) 6 h, (C) 2 days, and (D) 4 days. When otherwise indicated, scale bar = 100 nm.

Both bundle@AgNPs and NR@AgNP$_{15}$ assemblies were fabricated using branched PEI as polymeric coating for gold substrates. Different positively charged polyelectrolytes (poly(allylamine hydrochloride), PAH; and poly(diallyldimethylammonium chloride), PDDA, were also tested. However, the resulting NR@AgNP$_{15}$ exhibited a lower surface density of silver nanoparticles (Figure 2.14). In these cases, though a welding phenomenon did occur, it developed into an inhomogeneous silver distribution along the NRs surfaces via an apparently slower process. This is most likely associated with the increased separation between surface-bound AgNPs that hampers the fast atomic diffusion.

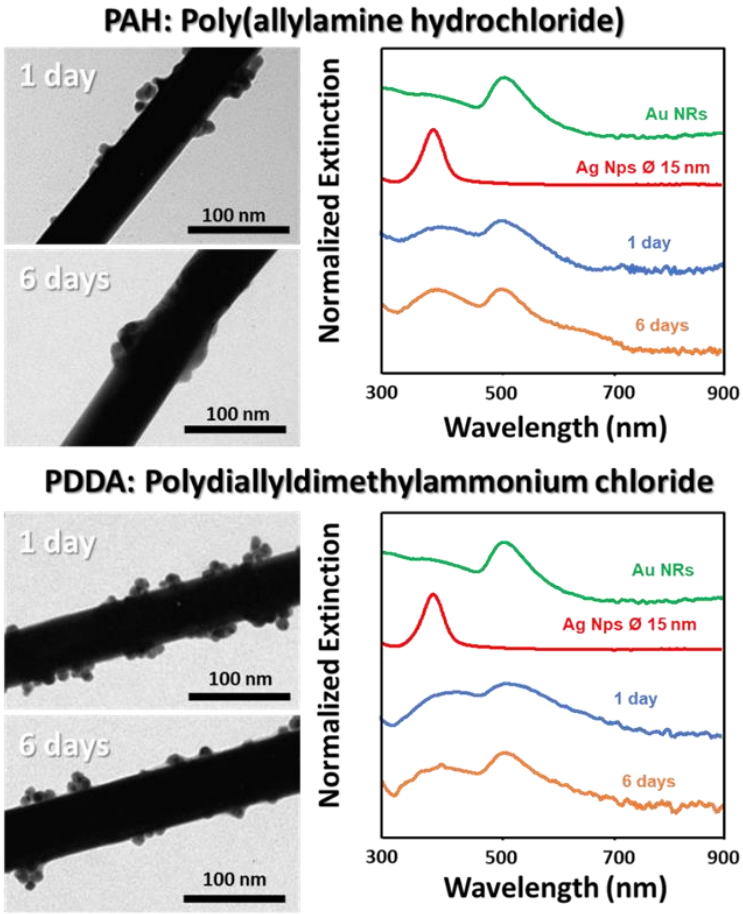

Figure 2.14. TEM images and extinction spectra of NR@$AgNP_{15}$ assemblies produced with two different polyelectrolytes (PAH, top; and, PDDA, bottom)) at two different stages of the welding process (1 and 6 days). The extinction spectra of the individual NPs components are also included for comparison.

Another examined variable is related to the geometrical features of the Au substrate. In this regard, long Au rods were replaced with spherical AuNPs of a diameter size approximately equal to the NRs thickness (i.e., the dimensions of the gold substrate were maintained in the *xz* plane with the reduction of the NR length to match the sphere diameter). Thus, 107 ± 6 nm size AuNPs (Figure 2.15 and Figure 2.16A) were first coated with PEI and then combined with $AgNP_{15}$ to yield the corresponding $AuNP_{107}$@$AgNP_{15}$ core-satellites.

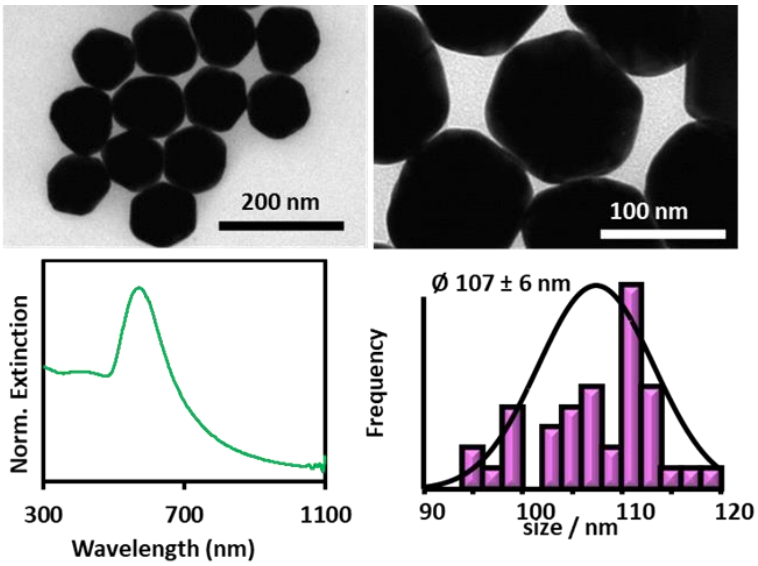

Figure 2.15. TEM images, extinction spectrum, and size histogram distribution of 107 ± 6 nm Au nanoparticles ($AuNP_{107}$).

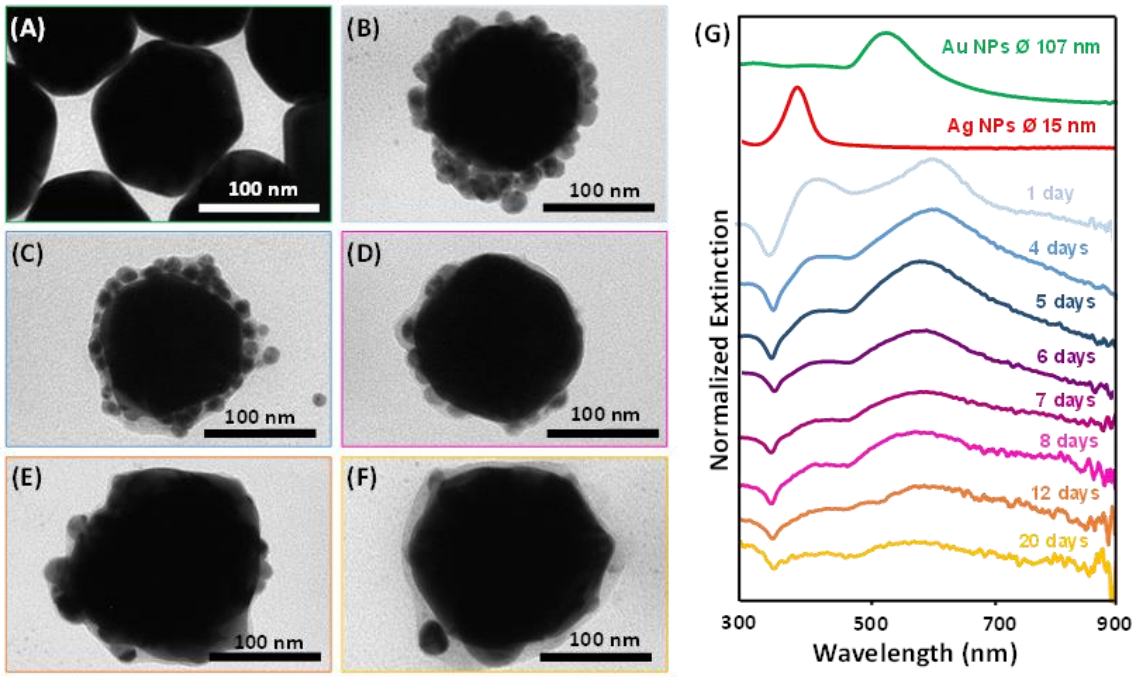

Figure 2.16. (A) Representative TEM image of approx. 107 nm Au nanoparticles ($AuNP_{107}$). (B-F) Representative TEM images the $AuNP_{107}$@$AgNP_{15}$ assemblies at 5 different stages of the welding process (1, 4, 8, 12, and 20 days, from (B) to (F) respectively). (G) Extinction spectra of the $AuNP_{107}$@$AgNP_{15}$ assemblies over a period of 20 days. The initial spectra of the individual Au and Ag colloids were also included. The stacked extinction spectra were normalized to their maxima for better visualization.

Representative TEM images of the $AuNP_{107}$ and the corresponding assemblies at different aging times (1, 4, 8, 12, and 20 days) are illustrated in Figure 2.16A-F and Figure 2.17.

Different from NRs, after 4 days most of the AgNPs on Au spheres still retain a spherical morphology, and the welding process remains far to be complete (Figure 2.16C). Approximately 8 days are necessary to discern a plain loss of Ag nanoparticles geometry (Figure 2.16D and Figure 2.17B) and ca. 20 days to observe the almost complete fusion onto the Au substrate, though bulging Ag spots can be still distinguished (Figure 2.16F and Figure 2.17C). These results agree with the time evolution UV-Vis spectral analysis reported in Figure 2.16G. On day 1, the LSPRs of individual Au and AgNPs shift from ca. 580 nm and 400 nm to ca. 670 nm and 430 nm, respectively, due to plasmon coupling. After 4 days, the two plasmon resonances become broader but remain mainly centered at the same positions, revealing that the welding process has been taking place at a relatively low rate. The blueshift of the Au feature as well as the overall drop in intensity and spectral broadening of both Ag and Au contributions are far more pronounced in the later days.

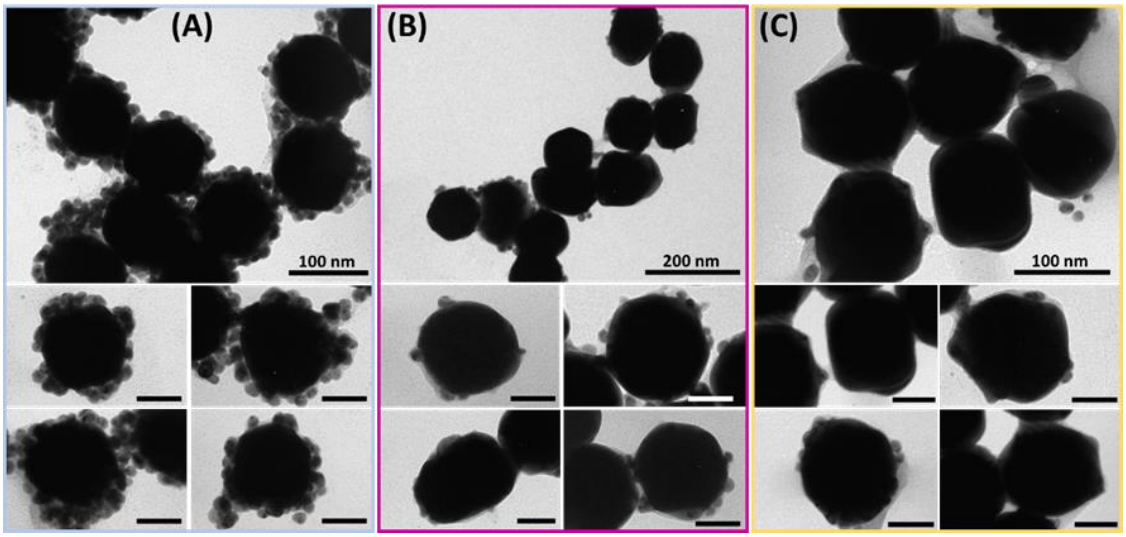

Figure 2.17. Additional TEM images of $AuNP_{107}$@$AgNP_{15}$ at different stages of the welding process: (A) 1 day, (B) 8 days, and (C) 20 days. When otherwise indicated, scale bar = 50 nm.

The welding process of $AuNP_{107}$@$AgNP_{15}$ assemblies was also monitored using SERS as a characterization tool. To this end, benzenethiol (BT) was selected as a probe molecule. The nanostructures, previously spin-coated on a glass slide, were exposed to a saturated atmosphere of BT in the gas phase to guarantee a full monolayer coating. SERS maps were recorded by interrogating the samples using three different lasers with excitation wavelengths of 514, 633 and 785 nm. Notably, only when illuminated with the NIR source, the samples provide intense SERS signals. The acquired SERS spectra reveal the characteristic spectral bands of BT centered at ca. 999 cm^{-1}, ascribed to ring stretching, and 1020 and 1070 cm^{-1}, assigned to C–C–H in-plane deformations (Figure 2.18A).[25] The detected intensity of the 1070 cm^{-1} band is

represented at different stages of the welding process (Figure 2.18B). For comparison, BT-coated $AuNP_{100}$ and $AgNP_{15}$ were also separately interrogated, but silver nanoparticles did not provide any detectable signal due to the weak enhancing capabilities of such small colloids. As it can be seen, SERS intensity undergoes an initial increase when AgNPs are assembled onto the Au core, which is associated with the formation of interparticle Ag-Ag and Au-Ag gaps. Based on previous studies on similar structures,[14] the larger electromagnetic contribution to the SERS signal resides at the core-satellite gaps rather than emerging from the plasmon coupling between adjacent small satellite particles. This is consistent with the subsequent drop in intensity observed from day 1 to ca. day 7 (i.e., when Ag nanoparticles progressively weld on top of the Au core). After day 8, there is a sudden rise in SERS intensity, reaching a plateau on day 9. This can be associated with the formation of a continuous silver layer on the gold core yielding nanoparticles analogous to conventional Au-core/Ag-shell obtained via chemical reduction, which has shown to display higher SERS activities as compared to the corresponding monometallic counterparts.[26, 27.]

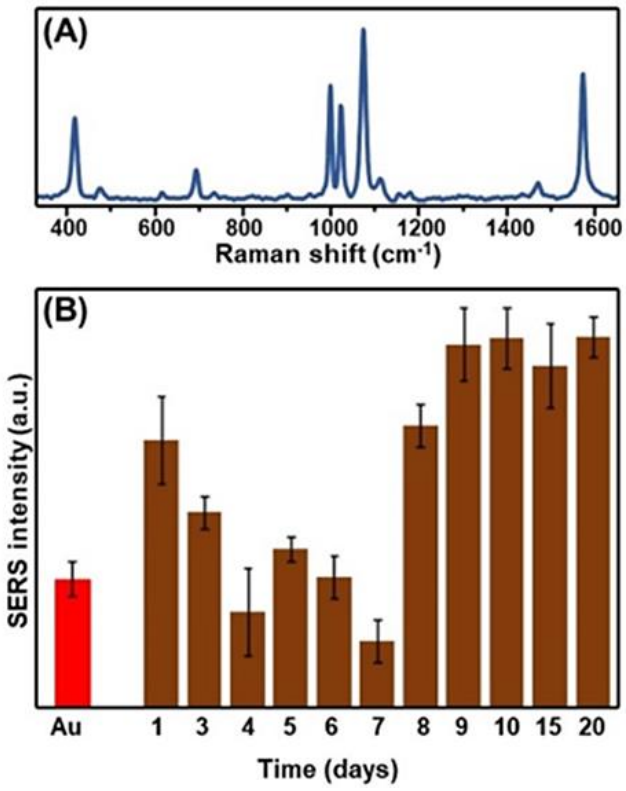

Figure 2.18. (A) SERS spectrum of benzenethiol (BT) on $AuNP_{107}$@$AgNP_{15}$ assemblies (day 1, 785 nm laser). (B) SERS intensities of the 1070 cm^{-1} BT bands acquired at different stages of the welding process (N = 20). The SERS intensity of $AuNP_{100}$ alone was also included. $AgNP_{15}$ particles did not provide any distinguishable signal.

These results highlight the central role of the Au substrate geometrical features in shaping the evolution of the welding process. This seems to be directly correlated with the level

of AgNPs surface density that, in turn, would increases as the gold support is progressively "flattened". To further corroborate this hypothesis, $AuNP_{107}$ were replaced with nanospheres of smaller curvatures (i.e., larger nanoparticles with 199 ± 9 nm diameter, $AuNP_{199}$, Figure 2.19 and Figure 2.20A).

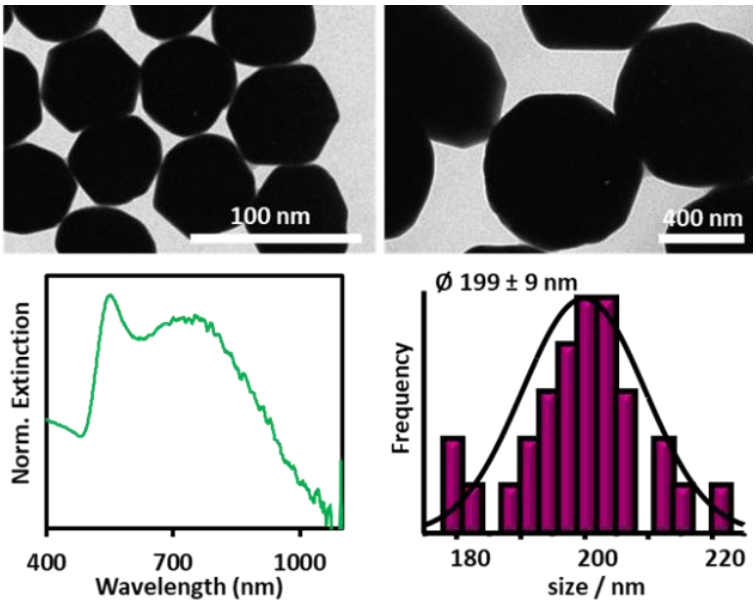

Figure 2.19. TEM images, extinction spectrum, and size histogram distribution of 199 ± 9 nm Au nanoparticles ($AuNP_{199}$).

Figure 2.20B-D and Figure 2.21A-C show representative TEM images and extinction spectra, respectively, of the $AuNP_{199}$@$AgNP_{15}$ composites after different days upon the initial assembling. The results demonstrate that much faster kinetics can be achieved by enlarging the gold nanoparticle diameter. Indeed, representative TEM images show that a smooth and homogeneous Ag layer is obtained on day 6, indicating the full completion of the welding process (Figure 2.20D and Figure 2.21C). At this stage, the optical analysis reveals an extinction spectrum where the feature associated with $AgNP_{15}$, initially centered at 400 nm, has largely disappeared due to nanoparticle merging. On the other hand, the quadrupolar and dipolar contributions of AuNPs, respectively located at ca. 560 nm and 760 nm, remain visible although redshifted as compared to those of pristine gold particles (Figure 2.20E).

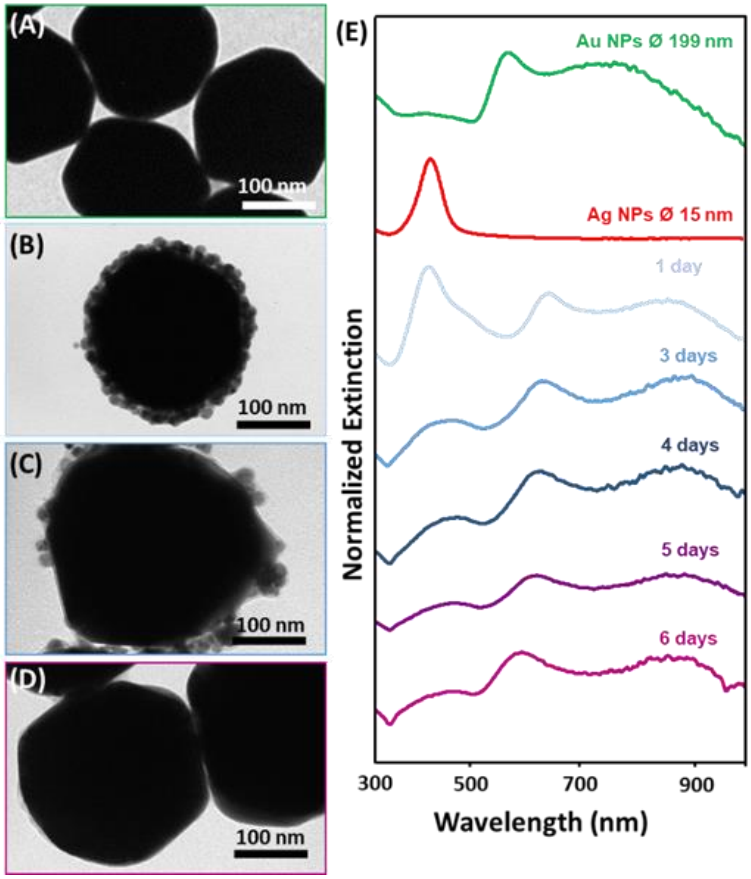

Figure 2.20. (A) Representative TEM image of ca. 199 nm AuNPs. (B-D) TEM images the AuNPs shown in (A) coated with 15 nm AgNPs at 3 stages during the welding process (1, 3, and 6 days from (B) to (D) respectively). (E) Extinction spectra corresponding to 5 different stages of welding. The spectra of the initial Au and AgNPs before the assembling are also included.

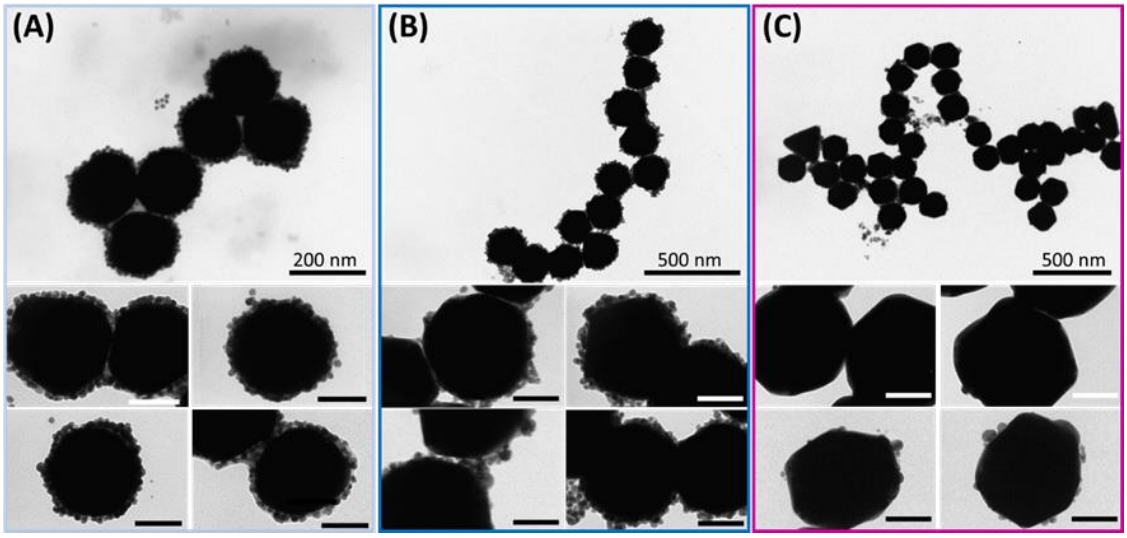

Figure 2.21. Additional TEM images of $AuNP_{199}@AgNP_{15}$ at different stages of the welding process: (A) 1 day, (B) 3 days, and (C) 6 days. When otherwise indicated, scale bar = 100 nm.

2.4 Conclusions

Herein, it is reported an extensive study on the nanowelding process of silver nanoparticles of increasing diameters onto gold substrates of diverse geometrical features. A wide array of techniques were employed, including SERS spectroscopy as a powerful surface characterization tool. The formation of homogenous and smooth silver coating is favored by decreasing the silver nanoparticles size while maximizing their surface loading. This latter factor is strictly related to the nature of the polymeric coating of gold substrates, with PEI showing the best result, which is possibly related to its branched structure. On the other hand, a decrease in gold substrate dimensions (i.e., higher surface curvature) significantly slows the nanowelding process. This extensive study provides valuable insights into the optimal design and engineering of bimetallic plasmonic Ag/Au structures for application in nanodevices.

REFERENCES

1. Sánchez-Iglesias, A.; Carbó-Argibay, E.; Glaria, A.; Rodríguez-González, B.; Pérez-Juste, J.; Pastoriza-Santos, I.; Liz-Marzán, L. M., Rapid epitaxial growth of Ag on Au nanoparticles: from Au nanorods to core–shell Au@ Ag octahedrons. *Chemistry–A European Journal* **2010,** *16* (19), 5558-5563.
2. Liu, M.; Guyot-Sionnest, P., Synthesis and optical characterization of Au/Ag core/shell nanorods. *The Journal of Physical Chemistry B* **2004,** *108* (19), 5882-5888.
3. Tebbe, M.; Kuttner, C.; Mayer, M.; Maennel, M.; Pazos-Perez, N.; König, T. A.; Fery, A., Silver-overgrowth-induced changes in intrinsic optical properties of gold nanorods: From noninvasive monitoring of growth kinetics to tailoring internal mirror charges. *The Journal of Physical Chemistry C* **2015,** *119* (17), 9513-9523.
4. Grouchko, M.; Roitman, P.; Zhu, X.; Popov, I.; Kamyshny, A.; Su, H.; Magdassi, S., Merging of metal nanoparticles driven by selective wettability of silver nanostructures. *Nature communications* **2014,** *5* (1), 1-6.
5. Pereira, Z.; Da Silva, E., Cold welding of gold and silver nanowires: a molecular dynamics study. *The Journal of Physical Chemistry C* **2011,** *115* (46), 22870-22876.
6. Lu, Y.; Huang, J. Y.; Wang, C.; Sun, S.; Lou, J., Cold welding of ultrathin gold nanowires. *Nat. Nanotechnol.* **2010,** *5* (3), 218-224.
7. Wagle, D. V.; Baker, G. A., Cold welding: a phenomenon for spontaneous self-healing and shape genesis at the nanoscale. *Materials Horizons* **2015,** *2* (2), 157-167.
8. Calderon, I.; Alvarez-Puebla, R. A.; Pazos-Perez, N., Gold-spiked coating of silver particles through cold nanowelding. *Nanoscale* **2021,** *13* (8), 4530-4536.
9. Mariño-López, A.; Blanco-Formoso, M.; Furini, L. N.; Sousa-Castillo, A.; Tiryaki, E.; Pérez-Lorenzo, M. s.; Testa-Anta, M.; Salgueiriño, V. n.; Kotov, N. A.; Alvarez-Puebla, R. A., Spontaneous Formation of Cold-Welded Plasmonic Nanoassemblies with Refracted Shapes for Intense Raman Scattering. *Langmuir* **2019,** *35* (11), 4110-4116.
10. Feng, H.; Yang, Y.; You, Y.; Li, G.; Guo, J.; Yu, T.; Shen, Z.; Wu, T.; Xing, B., Simple and rapid synthesis of ultrathin gold nanowires, their self-assembly and application in surface-enhanced Raman scattering. *Chemical Communications* **2009,** (15), 1984-1986.
11. Pazos-Pérez, N.; Baranov, D.; Irsen, S.; Hilgendorff, M.; Liz-Marzán, L. M.; Giersig, M., Synthesis of Flexible, Ultrathin Gold Nanowires in Organic Media. *Langmuir* **2008,** *24* (17), 9855-9860.
12. Blanco-Formoso, M.; Turino, M.; Rivas-Murias, B.; Guerrini, L.; Shavel, A.; de la Rica, R.; Correa-Duarte, M.; Salgueiriño, V.; Pazos-Perez, N.; Alvarez-Puebla, R. A., Iron-Assisted Synthesis of Highly Monodispersed and Magnetic Citrate-Stabilized Small Silver Nanoparticles. *The Journal of Physical Chemistry C* **2020,** *124* (5), 3270-3276.
13. Jessl, S.; Tebbe, M.; Guerrini, L.; Fery, A.; Alvarez-Puebla, R. A.; Pazos-Perez, N., Silver-Assisted Synthesis of Gold Nanorods: the Relation between Silver Additive and Iodide Impurities. *Small* **2018,** *14* (20), 1703879.
14. Pazos-Perez, N.; Fitzgerald, J. M.; Giannini, V.; Guerrini, L.; Alvarez-Puebla, R. A., Modular assembly of plasmonic core–satellite structures as highly brilliant SERS-encoded nanoparticles. *Nanoscale Advances* **2019,** *1* (1), 122-131.
15. Pazos-Perez, N.; Garcia de Abajo, F. J.; Fery, A.; Alvarez-Puebla, R. A., From nano to micro: synthesis and optical properties of homogeneous spheroidal gold particles and their superlattices. *Langmuir* **2012,** *28* (24), 8909-8914.
16. Fang, R.-R.; Guo, L.-J.; Wang, W.; Hou, C.-F.; Li, H., Atomic-scale simulation of nanojoining of Cu-Ag core-shell nanowires. *Physics Letters A* **2021,** *405*, 127425.
17. Alian, A. R.; Mahdi, E.; Meguid, S. A., Coupled molecular dynamics-Monte Carlo modeling of gold nanowire surface fasteners. *Applied Surface Science* **2020,** *507*, 145183.
18. Liu, Y.; Zhang, J.; Gao, H.; Wang, Y.; Liu, Q.; Huang, S.; Guo, C. F.; Ren, Z., Capillary-Force-Induced Cold Welding in Silver-Nanowire-Based Flexible Transparent Electrodes. *Nano Letters* **2017,** *17* (2), 1090-1096.
19. Bettscheider, S.; Kraus, T.; Fleck, N. A., Stabilization of ultrathin nanowires by self-assembly into bundles. *Acta Mater.* **2022,** *231*, 117799.
20. Wang, Y. Q.; Liang, W. S.; Geng, C. Y., Coalescence Behavior of Gold Nanoparticles. *Nanoscale Res Lett* **2009,** *4* (7), 684.
21. Cha, S.-H.; Park, Y.; Han, J. W.; Kim, K.; Kim, H.-S.; Jang, H.-L.; Cho, S., Cold welding of gold nanoparticles on mica substrate: Self-adjustment and enhanced diffusion. *Sci. Rep.* **2016,** *6* (1), 32951.

22. Toshihiro, T.; Shigetoshi, M., Diffusion of Polar and Nonpolar Molecules in Water and Ethanol. *Bulletin of the Chemical Society of Japan* **1990,** *63* (2), 533-537.
23. Carbó-Argibay, E.; Rodríguez-González, B.; Pastoriza-Santos, I.; Pérez-Juste, J.; Liz-Marzán, L. M., Growth of pentatwinned gold nanorods into truncated decahedra. *Nanoscale* **2010,** *2* (11), 2377-2383.
24. Johnson, C. J.; Dujardin, E.; Davis, S. A.; Murphy, C. J.; Mann, S., Growth and form of gold nanorods prepared by seed-mediated, surfactant-directed synthesis. *Journal of Materials Chemistry* **2002,** *12* (6), 1765-1770.
25. Holze, R., The adsorption of thiophenol on gold – a spectroelectrochemical study. *Physical Chemistry Chemical Physics* **2015,** *17* (33), 21364-21372.
26. Pande, S.; Ghosh, S. K.; Praharaj, S.; Panigrahi, S.; Basu, S.; Jana, S.; Pal, A.; Tsukuda, T.; Pal, T., Synthesis of Normal and Inverted Gold−Silver Core−Shell Architectures in β-Cyclodextrin and Their Applications in SERS. *The Journal of Physical Chemistry C* **2007,** *111* (29), 10806-10813.
27. Lv, X.-H.; Liao, W.-Q.; Li, P.-F.; Wang, Z.-X.; Mao, C.-Y.; Zhang, Y., Dielectric and photoluminescence properties of a layered perovskite-type organic–inorganic hybrid phase transition compound: NH3(CH2)5NH3MnCl4. *Journal of Materials Chemistry C* **2016,** *4* (9), 1881-1885.

Chapter 3

Plasmonic Azobenzene Chemoreporter for Surface-Enhanced Raman Scattering Detection of Biothiols

Plasmonic Azobenzene Chemoreporter for Surface-enhanced Raman Scattering Detection of Biothiols

Low molecular weight thiols are highly active substances extensively involved in human physiology which abnormal levels have been associated with various diseases. Major efforts have been recently dedicated to develop novel nanosensing methods for the low cost and fast quantification of this class of analytes in minimally pre-treated samples. In this chapter, a novel strategy for engineering a highly efficient surface-enhanced Raman scattering (SERS) spectroscopy platform for the dynamic sensing of biothiols is presented. Colloidally stable silver nanoparticles clusters equipped with a specifically designed azobenzene derivative (AzoProbe) were generated as highly SERS active substrates. In the presence of small biothiols (e.g., glutathione, GSH), breakage of the AzoProbe diazo bond causes drastic spectral changes that can be quantitatively correlated with the biothiol content with a limit of detection of ca. 5 nM for GSH. An identical response was observed for other low molecular weight thiols, while larger macromolecules with free thiol groups (e.g., bovine serum albumin) do not produce distinguishable spectral alterations. This indicates the suitability of the SERS sensing platform for the selective quantification of small biothiols.

This work has been published in:

Biosensors 12-5, pp. 267, 2022 (DOI: 10.3390/bios12050267)

"Plasmonic Azobenzene Chemoreporter for Surface-Enhanced Raman Scattering Detection of Biothiols"

Mariacristina Turino; Ramon A Alvarez-Puebla; Luca Guerrini

3.1 Introduction

It is well-known that low molecular weight thiols play a key role in human homeostasis.[1] Indeed, important variations in the levels of the most abundant biothiols glutathione (GSH) and cysteine (Cys), have been associated with cancer,[2] neurodegenerative disorders,[3] and cardiovascular diseases,[4, 5] among others. Moreover, the overall dysregulation of the dynamic thiol-disulfide homeostasis has been also related to multiple diseases.[6, 7] Thus, the development of methods that rapidly determine their content in biological fluids represents a breakthrough for early diagnosis or monitoring of biothiols-related pathologies.

Conventional approaches such as high-performance liquid chromatography (HPLC), and mass spectrometry (MS), provide a highly sensitive response but are time-consuming, expensive, and not applicable in remote settings.[8] Moreover, biothiols can fastly oxidize, so methods that allow fast quantification with minimal sample pre-treatment are particularly suitable.[9]

To overcome the intrinsic limitations of traditional techniques, new approaches have been developed. Among others, new nanosensors based on surface-enhanced Raman spectroscopy (SERS) have been designed.[9, 10, 11, 12] Under this aspect, the high affinity of biothiols mercapto group for gold and silver can be translated into a strong advantage for direct SERS detection. Unfortunately, the typical low Raman cross-section of this class of molecules represents an important limit so indirect strategies have been investigated. An example is the use of an external Raman probe that bind metallic surface through the pyridinic group. The latter can be displaced by biothiols yielding a drop in the overall intensity.[13, 14] Alternatively, several studies focused on the GSH-mediated disulfide breakage of disulfide molecules or structurally analogous. In this case, the important changes highlighted in the SERS spectrum are attributable to the release of molecule fragments able then to bind the metallic surface via the mercapto group generated by the breakage.[15, 16, 12]

On the other hand, the competition of other molecules, typically present in complex matrices, for their adsorption onto the metallic surface, has a negative impact on the response of the biosensor and, also, on the discrimination of the spectral features of the biothiol from spurious interferences. Recently, Shen et al. developed a background-free SERS method working with particles functionalized with recognition elements that include disulfide bond modified oligonucleotides and additionally, a compact mixed layer of thiolated polyethyleneglycol (PEG-SH) to prevent aggregation. In this case, the breakage of the disulfide bond causes the release of a short DNA chain labeled with Cy5 as the SERS probe.[17] It is worth considering that the

manufacturing cost for chemically modified oligonucleotides remains extremely high limiting the applicability of the latter.[18]

In this chapter, it is proposed a synthesized mercapto-azobenzene probe (AzoProbe) as an efficient low-cost chemoreceptor for the detection of biothiols. This choice is driven by previous studies in which azobenzene and its derivatives make rise to tremendous structural changes upon reduction of the azo bond by thiols.[19] The produced chemoreceptor is then conjugated to silver nanoparticles (AgNPs) inducing the formation of clusters that are in a second moment, encapsulated with PEG-SH to impart high colloidal stability in complex biological media. The SERS efficiency of active substrates was tested against GSH as a representative small thiolated biomolecule.

3.2 Experimental section

3.2.1 Materials

Silver nitrate (99.8%, $AgNO_3$), magnesium sulfate (99%, $MgSO_4$), trisodium citrate dihydrate (≥99.5%, $C_6H_5Na_3O7{\cdot}2H_2O$), and ascorbic acid (99%, $C_6H_8O_6$), were acquired from Acros Organics. 4-aminothiophenol (≥97%, 4-ATP), sodium nitrite (98%, $NaNO_2$), and hydrochloric acid (36.5-38%, HCl), were purchased from Alfa Aesar. Phenol (99%, C_6H_5OH), sodium hydroxide (≥99.5%, NaOH), L-Glutathione reduced (99.72%, $C_{10}H_{17}N_3O_6S$), L-Glutathione oxidized (99.72%, $C_{20}H_{32}N_6O_{12}S_2$), and poly(ethylene glycol) methyl ether thiol (99%, $CH_3O(CH_2CH_2O)nCH_2CH_2SH$, 800 ethylene monomers repetitions, Mw ~ 35 kDa), were purchased from Sigma-Aldrich. Phosphate buffered saline tablets and L-Cysteine hydrochloride monohydrate (98.5%, $C_3H_{10}ClNO_3S$) were purchased from Thermo Fisher. All reactants were used without further purification. Milli-Q water (18 MU cm^{-1}) was used in all aqueous solutions. All glassware was cleaned with aqua regia before the experiments.

3.2.2 Synthesis of spherical silver nanoparticles (AgNPs)

Spherical silver nanoparticles with a diameter of 55 nm approximately were produced as previously reported.[20] To 100 mL of boiling H_2O, a mixture containing AA (100 µL, 0.1 M) and $C_6H_5Na_3O_7{\cdot}2H_2O$ (1.36 mL, 0.1 M) was added under vigorous stirring. After 1 min, a previously 5 minutes incubated solution containing $AgNO_3$ (298 µL, 0.1 M) and $MgSO_4$ (224 µL, 0.1 M), was also added. The reaction is let stirring and heating for 1 h. The obtained colloid was then washed once via centrifugation (4000 rpm, 10 minutes) to remove the excess of citrate, redispersed in Milli-Q water to an estimated concentration of $[Ag^0] = 3{\times}10^{-4}$ M, and further characterized.

3.2.3 Synthesis of the AzoProbe

Synthesis of the AzoProbe was performed based on the report by Kar et al.[21] Diazonium salt is first obtained by the diazotization of 4-ATP with nitrous acid. Briefly, 0.5 g of 4-ATP (4 mmol) were dissolved in 10 mL of HCl 0.001 M. Then 0.27 g of $NaNO_2$ were added to the reaction. The mixture was left under gently stirring for 45 minutes. An ice bath was used to reach a reaction temperature below 5° C. After complete diazotization, the mixture changes from transparent to slightly yellow. Then, 0.46 g of C_6H_5OH (ca. 4.8 mmol) previously dissolved in cooled NaOH (56 µL, 0.5 M), are slowly added to the so-obtained diazonium intermediate. The reaction is left under mild stirring for 45 minutes at a temperature below 5° C. Afterward, the final solution turns from slightly yellow to gold confirming the formation of the desired mercaptophenyl azo phenol (AzoProbe).

3.2.4 Functionalization of the Ag nanoparticles with the AzoProbe (Ag@AzoProbe) and polyethylene glycol (PEG) encapsulation (Ag@AzoProbe@PEG)

2 mL of the AgNPs colloids were first washed one time (4000 rpm, 10 minutes) to remove the excess of citrate and then added dropwise under vigorous stirring to 0.8 mL of the synthesized AzoProbe. The mixture was left incubated overnight and then mildly centrifuged once (1000 rpm, 10 minutes) and the pellet made of AgNPs clusters functionalized with AzoProbe (Ag@AzoProbe) was redispersed in 2 mL of Milli-Q water. 530 µL of poly(ethylene glycol) methyl ether thiol (PEG-SH) 10^{-6} M was added to the solution of Ag@AzoProbe under vigorous agitation and stirred overnight. The excess of the polymer was removed via centrifugation (1000 rpm, 10 minutes) and the encapsulated aggregates Ag@AzoProbe@PEG were collected and resuspended in 100 µL phosphate buffer saline (PBS, pH 7.4). The amount of PEG-SH was calculated to match the one corresponding to a full monolayer coverage of the AgNPs considering a polymer footprint of 2.18 nm^2 ($2.65x10^{-10}$ mol of PEG-SH per 1 mL of Ag colloids containing ca. $3×10^{10}$ NPs).[22]

3.2.5 Characterization

Microscopy. Images were obtained through a transmission electron microscope (TEM). Samples were prepared by drying water suspensions on carbon−Formvar-coated 200 mesh copper grids and using a JEOL 1011 Scanning transmission electron microscope operating at an acceleration voltage of 100 kV.

UV-Visible spectroscopy. UV-Vis spectroscopy (Thermo Scientific Evolution 201), was used to characterize the optical response and the size of NPs.

SERS spectroscopy. Inelastic scattering was collected in backscattering geometry with a Renishaw inVia Reflex system equipped with a 2D-CCD detector and a Leica confocal microscope. Measurements were carried out with a 785 nm laser line at the acquisition time of 1 s and power at the sample of 3 mW. The laser was focused on the colloidal suspension using a macrolens. Samples were prepared by adding 10 µL of Ag@AzoProbe@PEG suspension to 200 µL of GSH solution in PBS (pH 7.4) at different concentrations and left incubating for 1 h. An identical protocol was also applied for other low molecular weight biothiols such as glutathione disulfide (GSSG) and cysteine (Cys), and high molecular weight biothiols (bovine serum albumin, BSA). Silver nanoparticles previously incubated with 4-ATP 10^{-7} M were aggregated by adding 30 µL of a 0.5 M solution of $MgSO_4$ to 1 mL of colloids to acquire an intense SERS fingerprint of 4-ATP on AgNPs.

3.3 Results and discussion

Structural requirements of SERS chemosensors commonly involve the presence of a mercapto group to covalently bind the metallic surface.[23, 24, 25, 26] Thus, a mercapto azobenzene derivative was designed by combining 4-ATP and phenol (PHE) through azo-coupling reaction as depicted in Figure 3.1A. First, to the *in situ* generated nitrous acid by the reaction between sodium nitrite and hydrochloric acid, 4-ATP was added. The corresponding diazonium intermediate was then coupled with phenol in a strong basic medium leading to the formation of the corresponding mercaptophenyl-azo-phenol (AzoProbe) via electrophilic aromatic substitution.[21] Figure 3.1B shows the corresponding UV-Vis spectra at each stage of the synthesis, confirming the successful generation of the AzoProbe. It is worth noting that, in the proposed synthesis, a slight excess of PHE was employed to maximize the 4-ATP conversion. In this way, the reaction mixture can be directly combined with silver nanoparticles without further purification steps, since only AzoProbe is equipped with a mercapto group that firmly binds the metallic surface while other reagents can be easily removed from the medium in subsequent washing cycles.

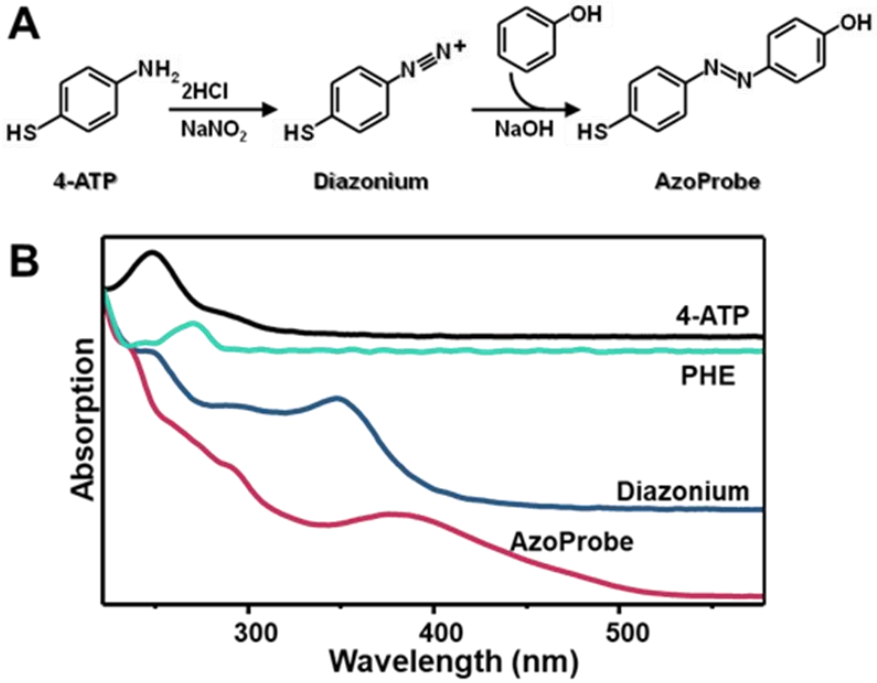

Figure 3.1. (A) Scheme representing the synthetic route for mercaptophenyl azo phenol (AzoProbe) coupling. (B) Extinction spectra of the precursors 4-aminothiophenol (4-ATP) and phenol (PHE), the diazonium intermediate, and the final AzoProbe.

The methodological approach for SERS substrate fabrications is outlined in Figure 3.2A. Citrate-capped silver colloids (AgNPs) of ca. 55 ± 5 nm diameter (Figure 3.2B) were combined with the AzoProbe reaction mixture to a final probe concentration of ca. 0.1 mM. Such AzoProbe content is estimated to be sufficiently high to promote the formation of a full monolayer via direct covalent binding with the pending SH group of the chemosensor. The sample was incubated overnight to maximize the AzoProbe surface density on Ag colloids. Such chemical modification causes the localized surface plasmon resonance (LSRP) of silver colloids, initially centered at 421 nm, to undergo a red-shift to ca. 438 nm and a marked broadening (Figure 3.2D). Moreover, a new contribution emerges at ca. 700 nm, indicating the formation of metastable nanoparticle aggregates (Ag@AzoProbe) in Milli-Q water.

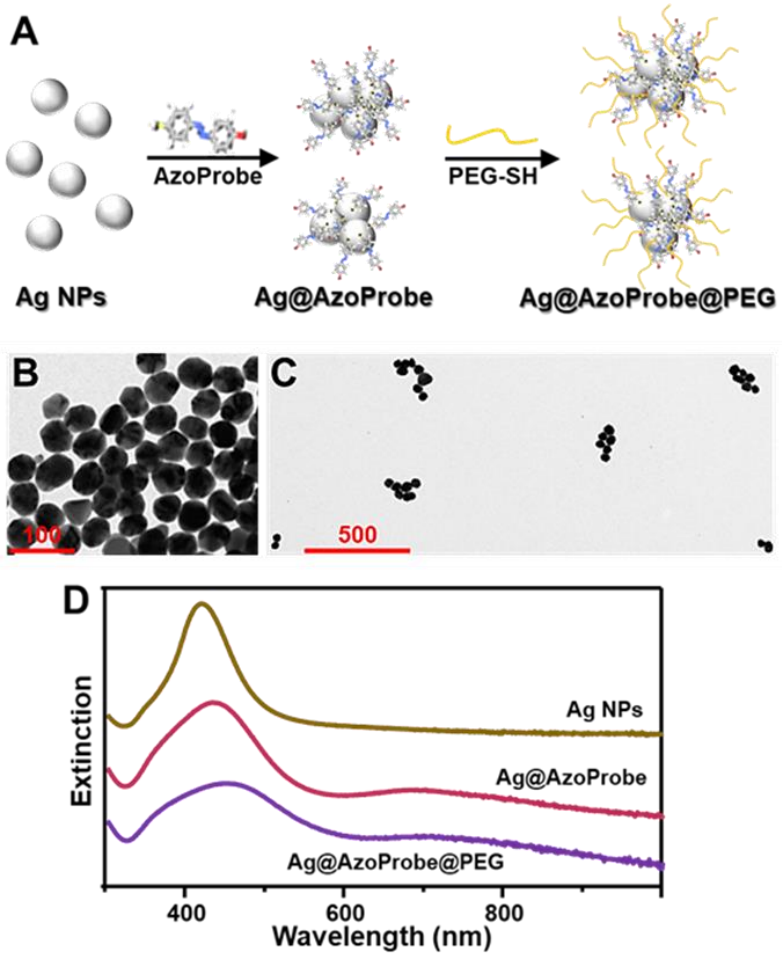

Figure 3.2. (A) Outline of the fabrication of AzoProbe modified Ag clusters stabilized with PEG-SH. (B) TEM images of Ag@AzoProbe and (C) Ag@AzoProbe@PEG clusters, respectively (scale bars = 100 and 500 nm, respectively). (D) Extinction spectra of bare silver colloid (AgNPs), upon azo-compound functionalization (Ag@AzoProbe), and corresponding PEG-SH encapsulated clusters (Ag@AzoProbe@PEG) in PBS buffer (pH 7.4).

To increase the colloidal stability of the Ag@AzoProbe in complex media, such as biological fluids, PEG-SH (35 kDa) was successively added to the colloidal mixture to yield Ag@AzoProbe@PEG clusters.[22] PEG-SH is a neutral, water-soluble, and biocompatible polymer that has been extensively exploited as a surface stabilizer to protect metallic nanoparticles from aggregation against salts.[27] After overnight incubation, the AgNPs solution was submitted to low-speed centrifugation to remove unbound polymer molecules. The pellet was collected and redispersed in PBS (pH = 7.4), while the light-yellow supernatant was discarded. In this way, the residual fraction of individual, non-clustered nanoparticles in the supernatant was largely removed from the medium, as can be also inferred from the weakening of the plasmonic contribution at 421 nm in the extinction spectra (Figure 3.2D). This enabled the separation of highly SERS active Ag@AzoProbe@PEG (Figure 3.2C) clusters from poorly efficient enhancers. On the other hand, non-pegylated clusters redispersed in PBS buffer underwent a slow but irreversible aggregation over time.

Figure 3.3 compares the SERS spectrum of Ag@AzoProbe@PEG clusters with that of silver colloids modified with the AzoProbe precursor 4-aminothiophenol (Ag@4-ATP). Differently from 4-ATP, PHE does not show any affinity for the Ag surface and thus, the normal Raman spectrum of the solid phenol was acquired instead. Neighboring 4-ATP molecules, however, undergo photocatalyzed diazotization onto silver nanostructures yielding the corresponding 4,4'-dimercaptoazobenzene (DMAB) product.[28, 29] To avoid dimerization, 4-ATP was then added at a low concentration (10^{-7} M) to the AgNPs suspension.[28] The so-functionalized nanoparticles were then aggregated using a $MgSO_4$ solution as the aggregating agent to obtain a detectable SERS spectrum of the non-dimerized molecule (Figure 3.3, Ag@4-ATP). The most intense 4-ATP bands are centered at 368, 1008, 1079, 1494, and 1599 cm^{-1}, which have been ascribed to out-of-plane C-C-C modes (368 and 1008 cm^{-1}), ring breathing and C-S stretching (1079 cm^{-1}), N-H bending (1494), and C=C stretching (1599 cm^{-1}).[30] Meanwhile, the SERS spectrum of the synthesized AzoProbe (Figure 3.3, Ag@AzoProbe@PEG) displays new intense features which are informative of the formation of the -N=N- bond between the 4-ATP and PHE precursors. Most notably, bands such as at 1143, 1191, 1310, 1382, 1433, and 1578 cm^{-1}, can be mainly assigned to a combination of N-C stretching and C-H bending (1143, 1191, and 1433 cm^{-1}), N-C and C-H bending (1310 cm^{-1}), and C-C and N-N stretching (1382 and 1578 cm^{-1}).[30] Additionally, the intense band at 1412 cm^{-1} and the weak feature at 1474 cm^{-1} have been previously assigned to the *trans* and *cis* forms, respectively, of the structurally analogous 4-phenylazophenol.[31]

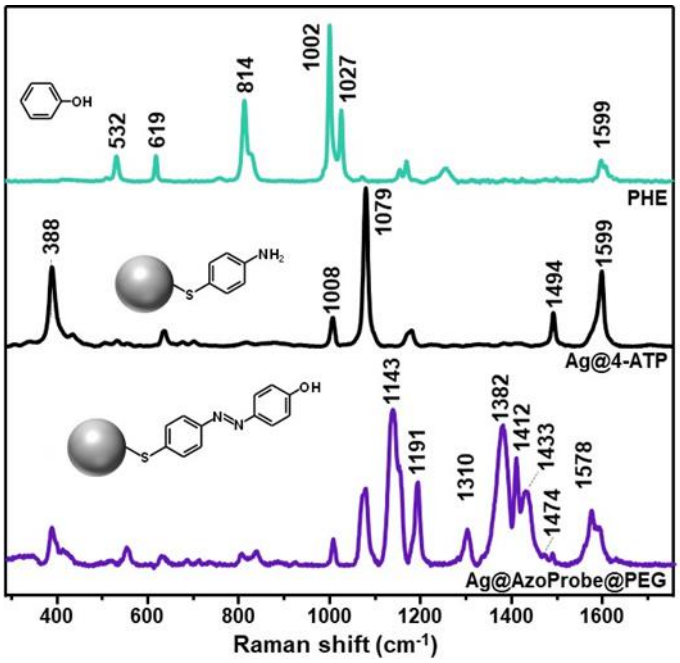

Figure 3.3. Normal Raman spectrum of phenol (PHE) and SERS spectra of 4-ATP on aggregated AgNPs and AzoProbe in Ag@AzoProbe@PEG clusters.

The clinically relevant GSH, the most abundant intracellular nonprotein thiol,[32] was selected as a representative small thiolated biomolecule. The SERS response of the Ag@AzoProbe@PEG material to the presence of GSH was monitored in samples obtained by diluting 10 µL of highly SERS-active clusters into 200 µL of GSH solution in PBS buffer (pH = 7.4). Figure 3.4A shows the SERS spectra of Ag@AzoProbe@PEG before and after the addition to a 100 nM solution of GSH, collected after 1 h incubation at room temperature. The exposure of the substrate to glutathione leads to a major reshaping of the molecular probe spectrum, demonstrating the ability of GSH to diffuse across the external PEG shell and onto the AzoProbe functionalized metallic surface. Remarkably, spectral reshaping involves those bands associated with vibrations of the azo bond that links the two aromatic moieties (see 1110–1520 cm^{-1} spectral range). As it has been reported, in response to GSH, azo dyes undergo reductive cleavage generating the respective amines.[33] This implies the release of the 4-aminophenol moiety from the silver surface while the residual 4-ATP fragment remains anchored via the strong Ag-S bond (Figure 3.4B). However, in this case, dense patches of closely spaced 4-ATP molecules are left behind on Ag surfaces, including at the interparticle gaps, which then triggers their surface catalyzed dimerization upon laser illumination (Figure 3.4B). Indeed, the SERS spectrum of the GSH-treated clusters matches that of the self-diazotization product DMAB on silver colloids.[28, 29]

The evolution of the SERS profile in the spectral range of interest (1110–1520 cm^{-1}) as a function of a decreasing GSH concentration (from 100 nM to 3 nM) is reported in Figure 3.4C. To correlate the spectral reshaping with the analyte content, the SERS intensity ratio between the 1433 and 1382 cm^{-1} bands (I_{1433}/I_{1382}) was calculated. The latter has been selected as the spectral marker due to its extensive variation in the presence of GSH. The resulting intensity ratios are plotted against GSH concentration in Figure 3.4D, showing a good linear relation in the 7–100 nM range (r^2 = 0.978) and an estimated limit of detection of ca. 5 nM.

Figure 3.4. (A) SERS spectra of Ag@AzoProbe@PEG clusters before and after mixing with GSH (100 nM). (B) Outline of the proposed detection mechanism. (C) From bottom to top, SERS spectra of Ag@AzoProbe@PEG clusters at increasing GSH concentration (0, 5, 7, 10, 20, 40, 60, 80, 100, and 200 nM). (D) Intensity ratio I1433/I1382 vs. GSH concentration (logarithmic scale).

It is worth stressing that all SERS experiments were performed by focusing a 785 nm laser onto the colloidal samples using a macrolens. In this way, it is possible to obtain statistically averaged SERS spectra from a relatively high number of clusters in continuous Brownian motions within the scattering volume. At the same time, the Ag@AzoProbe@PEG clusters concentration in the sample was maintained sufficiently high to yield intense SERS spectra with well-defined features adopting an integration time of just 10 s. The intrinsically high sensitivity of the proposed method allows obtaining detection limits that far exceed those required to detect biothiols at biologically relevant concentrations in bodily fluids adopting thus, an experimental set-up that favors rapidity, simplicity, and spectral reproducibility, as required for quantitative applications,[34] although at the expense of the absolute detection sensitivity.

Identical spectral changes as those observed in Figure 3.4 for GSH (100 nM) have also been recorded for other small biothiols such as oxidized glutathione (GSSG) and cysteine (Cys) at the same concentration (Figure 3.5). A similar outcome emerged when the nanoprobes were exposed to a mixture of GSH and Cys at a 2:1 molar ratio (total biothiol content = 100 nM). Notably, when the Cys content is decreased to 8 nM, the intensity ratio I_{1433}/I_{1382} value (ca. 0.95) approaches that of GSH (ca. 1.0) at an analogous concentration. As also previously reported,[35] thiolated PEG coating of nanoparticles allows for small biothiols to approach the metallic surface while blocking large macromolecules. To verify such quality of Ag@AzoProbe@PEG clusters, nanostructures were exposed to a 40 mg/mL solution of bovine serum albumin (BSA), which was selected as a representative example of biomacromolecule furnished with thiol groups. No changes in the AzoProbe spectrum (Figure 3.5) were detected, which confirms the impossibility of large proteins to diffuse at the interparticle gaps within the clusters. Indeed, as it has been discussed in the Introduction section, the SERS signal from aggregates composed of closely-spaced nanoparticles is dominated by the contribution of the fraction of molecules that are entrapped at the interparticle gaps.[36, 37] The response of the sensing platform was also tested in the presence of 1 mM glucose, which was chosen as a representative non-thiolated and ubiquitous reducing chemical in biofluids. No alterations of the AzoProbe SERS spectrum were detected (Figure 3.5). On the contrary, small molecules such as ascorbic acid and hydroxyl radicals, that showed heterogeneous reactivity with azo groups,[38, 39] coexist with low molecular weight thiols in biofluids at concentrations well below the overall biothiol content, a condition that provides the basis for discrimination.

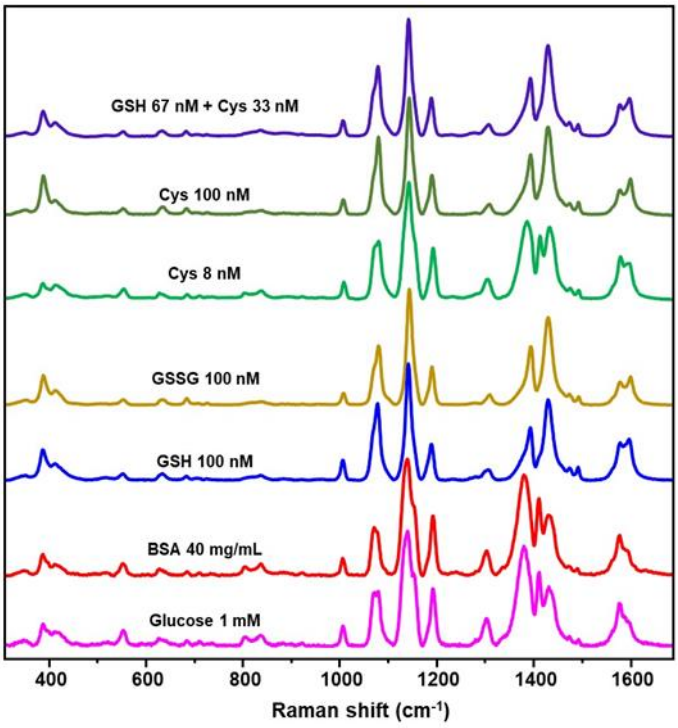

Figure 3.5. SERS spectra of Ag@AzoProbe@PEG clusters in PBS buffer (pH 7.4) containing glucose (1mM), BSA (40 mg/mL), GSH 100 nM, glutathione disulfide (GSSG) 100 nM, cysteine (Cys) 8 and 100 nM, and a mixture of GSH+Cys (6.7×10^{-8} M and 3.3×10^{-8} M, respectively).

3.4 Conclusions

In summary, the present work proposed a novel approach for engineering a highly efficient, low-cost platform for the dynamic SERS sensing of biothiols. An azobenzene derivative equipped with a mercapto group has been designed to firmly bind silver colloids via Ag-S bond while generating metastable and highly SERS active clusters in suspension. Subsequent encapsulation of the so-formed clusters with PEG-SH granted the required colloidal stability to be used in complex media such as biofluids. When exposed to GSH, the SERS spectrum of the AzoProbe displays major spectral changes, which were ascribed to the breakage of the diazo bond, causing the release of the 4-aminophenol moiety from the surface. The residual surface-bound 4-aminothiophenol fragment is then free to undergo metal-catalyzed dimerization with other neighboring molecules. The extent of such spectral alterations was quantitatively correlated with the GSH content in the ca. 7–100 nM range with an excellent limit of detection of ca. 5 nM. It is worth stressing that the linear range for accurate quantification can be simply tuned to different biothiol concentration ranges by merely varying the absolute content of SERS active clusters or via sample dilution. An identical response was observed for other low molecular weight thiols (i.e., oxidized glutathione and cysteine), while larger macromolecules with free thiol groups such as BSA do not produce distinguishable spectral alterations, indicating the suitability of the SERS sensing platform for the selective quantification of small biothiols.

REFERENCES

1. Giles, N. M.; Watts, A. B.; Giles, G. I.; Fry, F. H.; Littlechild, J. A.; Jacob, C., Metal and redox modulation of cysteine protein function. *Chemistry & biology* **2003,** *10* (8), 677-693.
2. Estrela, J. M.; Ortega, A.; Obrador, E., Glutathione in cancer biology and therapy. *Critical reviews in clinical laboratory sciences* **2006,** *43* (2), 143-181.
3. Saharan, S.; Mandal, P. K., The emerging role of glutathione in Alzheimer's disease. *Journal of Alzheimer's Disease* **2014,** *40* (3), 519-529.
4. Bajic, V. P.; Van Neste, C.; Obradovic, M.; Zafirovic, S.; Radak, D.; Bajic, V. B.; Essack, M.; Isenovic, E. R., Glutathione "redox homeostasis" and its relation to cardiovascular disease. *Oxidative Medicine and Cellular Longevity* **2019,** *2019*.
5. Go, Y.-M.; Jones, D. P., Cysteine/cystine redox signaling in cardiovascular disease. *Free Radical Biology and Medicine* **2011,** *50* (4), 495-509.
6. Ozben, S.; Kucuksayan, E.; Koseoglu, M.; Erel, O.; Neselioglu, S.; Ozben, T., Plasma thiol/disulphide homeostasis changes in patients with relapsing-remitting multiple sclerosis. *International journal of clinical practice* **2021,** *75* (7), e14241.
7. Vural, G.; Gumusyayla, S.; Bektas, H.; Deniz, O.; Alisik, M.; Erel, O., Impairment of dynamic thiol–disulphide homeostasis in patients with idiopathic Parkinson's disease and its relationship with clinical stage of disease. *Clinical Neurology and Neurosurgery* **2017,** *153*, 50-55.
8. Hao, Y.; Yin, Q.; Zhang, Y.; Xu, M.; Chen, S., Recent Progress in the Development of Fluorescent Probes for Thiophenol. *Molecules* **2019,** *24* (20), 3716.
9. Kuligowski, J.; El-Zahry, M. R.; Sánchez-Illana, Á.; Quintás, G.; Vento, M.; Lendl, B., Surface enhanced Raman spectroscopic direct determination of low molecular weight biothiols in umbilical cord whole blood. *Analyst* **2016,** *141* (7), 2165-2174.
10. Li, P.; Ge, M.; Yang, L.; Liu, J., Metal coordination-functionalized Au–Ag bimetal SERS nanoprobe for sensitive detection of glutathione. *Analyst* **2019,** *144* (2), 421-425.
11. Sánchez-Illana, A. n.; Mayr, F.; Cuesta-García, D.; Piñeiro-Ramos, J. D.; Cantarero, A. s.; Guardia, M. d. l.; Vento, M. x.; Lendl, B.; Quintás, G.; Kuligowski, J., On-capillary surface-enhanced Raman spectroscopy: determination of glutathione in whole blood microsamples. *Analytical chemistry* **2018,** *90* (15), 9093-9100.
12. Li, Y.; Jiang, L.; Zou, Y.; Song, Z.; Jin, S., Highly reproducible SERS sensor based on self-assembled Au nanocubic monolayer film for sensitive and quantitative detection of glutathione. *Applied Surface Science* **2021,** *540*, 148381.
13. Zhao, J.; Zhang, K.; Ji, J.; Liu, B., Sensitive and label-free quantification of cellular biothiols by competitive surface-enhanced Raman spectroscopy. *Talanta* **2016,** *152*, 196-202.
14. Ouyang, L.; Zhu, L.; Jiang, J.; Tang, H., A surface-enhanced Raman scattering method for detection of trace glutathione on the basis of immobilized silver nanoparticles and crystal violet probe. *Analytica chimica acta* **2014,** *816*, 41-49.
15. Bu, Y.; Zhu, G.; Li, S.; Qi, R.; Bhave, G.; Zhang, D.; Han, R.; Sun, D.; Liu, X.; Hu, Z., Silver-nanoparticle-embedded porous silicon disks enabled SERS signal amplification for selective glutathione detection. *ACS applied nano materials* **2017,** *1* (1), 410-417.
16. Wei, C.; Liu, X.; Gao, Y.; Wu, Y.; Guo, X.; Ying, Y.; Wen, Y.; Yang, H., Thiol–disulfide exchange reaction for cellular glutathione detection with surface-enhanced raman scattering. *Analytical chemistry* **2018,** *90* (19), 11333-11339.
17. Shen, Y.; Yue, J.; Shi, W.; Xu, W.; Xu, S., Target-triggered hot spot dispersion for cellular biothiol detection via background-free surface-enhanced Raman scattering tags. *Biosensors and Bioelectronics* **2020,** *151*, 111957.
18. Macdonald, D.; Smith, E.; Faulds, K.; Graham, D., DNA detection by SERS: hybridisation parameters and the potential for asymmetric PCR. *Analyst* **2020,** *145* (5), 1871-1877.
19. Boulègue, C.; Löweneck, M.; Renner, C.; Moroder, L., Redox potential of azobenzene as an amino acid residue in peptides. *ChemBioChem* **2007,** *8* (6), 591-594.
20. Pazos-Perez, N.; Fitzgerald, J. M.; Giannini, V.; Guerrini, L.; Alvarez-Puebla, R. A., Modular assembly of plasmonic core–satellite structures as highly brilliant SERS-encoded nanoparticles. *Nanoscale Adv.* **2019,** *1* (1), 122-131.
21. Kar, A., *Advanced practical medicinal chemistry*. New Age International: **2007**.

22. Rahme, K.; Chen, L.; Hobbs, R. G.; Morris, M. A.; O'Driscoll, C.; Holmes, J. D., PEGylated gold nanoparticles: polymer quantification as a function of PEG lengths and nanoparticle dimensions. *Rsc Advances* **2013,** *3* (17), 6085-6094.
23. Zhang, Y.; Gallego, I.; Plou, J.; Pedraz, J. L.; Liz-Marzán, L. M.; Ciriza, J.; García, I., SERS monitoring of local pH in encapsulated therapeutic cells. *Nanoscale* **2021,** *13* (34), 14354-14362.
24. Langer, J.; Jimenez de Aberasturi, D.; Aizpurua, J.; Alvarez-Puebla, R. A.; Auguié, B.; Baumberg, J. J.; Bazan, G. C.; Bell, S. E.; Boisen, A.; Brolo, A. G., Present and future of surface-enhanced Raman scattering. *ACS nano* **2019,** *14* (1), 28-117.
25. Pazos, E.; Garcia-Algar, M.; Penas, C.; Nazarenus, M.; Torruella, A.; Pazos-Perez, N.; Guerrini, L.; Vázquez, M. E.; Garcia-Rico, E.; Mascareñas, J. L., Surface-enhanced raman scattering surface selection rules for the proteomic liquid biopsy in real samples: Efficient detection of the oncoprotein c-MYC. *Journal of the American Chemical Society* **2016,** *138* (43), 14206-14209.
26. Guerrini, L.; Alvarez-Puebla, R. A., Surface-Enhanced Raman Scattering Sensing of Transition Metal Ions in Waters. *ACS Omega* **2021,** *6* (2), 1054-1063.
27. Tejamaya, M.; Römer, I.; Merrifield, R. C.; Lead, J. R., Stability of citrate, PVP, and PEG coated silver nanoparticles in ecotoxicology media. *Environmental science & technology* **2012,** *46* (13), 7011-7017.
28. Correa-Duarte, M. A.; Pazos Perez, N.; Guerrini, L.; Giannini, V.; Alvarez-Puebla, R. A., Boosting the quantitative inorganic surface-enhanced Raman scattering sensing to the limit: the case of nitrite/nitrate detection. *The Journal of Physical Chemistry Letters* **2015,** *6* (5), 868-874.
29. Sun, M.; Huang, Y.; Xia, L.; Chen, X.; Xu, H., The pH-controlled plasmon-assisted surface photocatalysis reaction of 4-aminothiophenol to p, p'-dimercaptoazobenzene on Au, Ag, and Cu colloids. *The Journal of Physical Chemistry C* **2011,** *115* (19), 9629-9636.
30. Novák, V. t.; Dendisová, M.; Matějka, P.; Bouř, P., Explanation of surface-enhanced raman scattering intensities of p-aminobenzenethiol by density functional computations. *The Journal of Physical Chemistry C* **2016,** *120* (32), 18275-18280.
31. Liu, W.; Bian, S.; Li, L.; Samuelson, L.; Kumar, J.; Tripathy, S., Enzymatic synthesis of photoactive poly (4-phenylazophenol). *Chemistry of materials* **2000,** *12* (6), 1577-1584.
32. Townsend, D. M.; Tew, K. D.; Tapiero, H., The importance of glutathione in human disease. *Biomedicine & pharmacotherapy* **2003,** *57* (3-4), 145-155.
33. Lei, H.; Mo, M.; He, Y.; Wu, Y.; Zhu, W.; Wu, L., Bioactivatable reductive cleavage of azobenzene for controlling functional dumbbell oligodeoxynucleotides. *Bioorganic Chemistry* **2019,** *91*, 103106.
34. Aroca, R., *Surface-enhanced vibrational spectroscopy*. John Wiley & Sons: 2006.
35. Li, C.; Chen, P.; Khan, I. M.; Wang, Z.; Zhang, Y.; Ma, X., Fluorescence–Raman dual-mode quantitative detection and imaging of small-molecule thiols in cell apoptosis with DNA-modified gold nanoflowers. *Journal of Materials Chemistry B* **2022**.
36. Le Ru, E.; Etchegoin, P.; Meyer, M., Enhancement factor distribution around a single surface-enhanced Raman scattering hot spot and its relation to single molecule detection. *The Journal of chemical physics* **2006,** *125* (20), 204701.
37. Le Ru, E.; Etchegoin, P., *Principles of Surface-Enhanced Raman Spectroscopy: and related plasmonic effects*. Elsevier: 2008.
38. Costas-Costas, U.; Bravo-Diaz, C.; Gonzalez-Romero, E., Kinetics and mechanism of the reaction between ascorbic acid derivatives and an arenediazonium salt: Cationic micellar effects. *Langmuir* **2005,** *21* (24), 10983-10991.
39. Maezono, T.; Tokumura, M.; Sekine, M.; Kawase, Y., Hydroxyl radical concentration profile in photo-Fenton oxidation process: generation and consumption of hydroxyl radicals during the discoloration of azo-dye Orange II. *Chemosphere* **2011,** *82* (10), 1422-1430.

Chapter 4

Fabrication of a graded-index (GRIN) lens metallic metamaterial

Fabrication of a graded-index (GRIN) lens metallic metamaterial

The optical response of gold nanoparticle-based metamaterials is governed by the geometry of these structures (i.e., size, shape, and interparticle spacing) rather than by the refractive indices of their components. Herein, a graded-index (GRIN) lens metallic metamaterial was fabricated via self-assembling of SERS-encoded gold nanoparticles of different sizes onto a micrometric silica spherical core. The presented experimental data are a part of an ongoing study carried out in collaboration with Prof. Vincenzo Giannini aimed at the design of extraordinarily transparent metallic metamaterials for infrared and terahertz applications.

4.1 Introduction

The unique properties arising from densely packed metallic metamaterials (e.g., unnaturally high refractive indexes combined with transparency for specific wavelengths)[1, 2] depend on their artificial dielectric character (i.e., an effective dielectric with a structure made of metallic components). Indeed, metallic particles forming an effective dielectric possess free electrons and act as “meta-molecules” or “meta-atoms”. This is because the electrons are only free to move in the confines defined by the same particles, which effectively mimics a dielectric. Furthermore, the tunability of the optical properties in metamaterials is achieved by altering parameters such as the size, shape, and spacing of the nanoparticle constituting the arrays.[3]

A typical metamaterial is represented by the graded-index (GRIN) lens. These fascinating materials are optical devices generally designed with radially varying refractive indexes that can converge impinging parallel light to a spot at the focal point.[4, 5] Typically, the three most common lenses are the Luneburg lens, Maxwell fish-eye lens, and a light concentrator (GRIN lens). A Luneburg lens (Figure 4.1A) focuses incident parallel radiation on a point on the surface to the opposite side where the incident wavelength impinges on the sphere.[6] On the other hand, the Maxwell fish-eye lens (Figure 4.1B) drives light from one point source and focuses it at the opposite point on a spherical surface.[7] In the concentrator lens (Figure 4.1C), light impinging on the sphere will be concentrated at the center of the sphere.[4] These lenses offer great advantages over conventional materials for the possibility to tune the local refractive indexes and, thus, obtain devices working in broadband ranges of wavelengths, an intriguing property that drives research on these metamaterials in numerous application fields.[8]

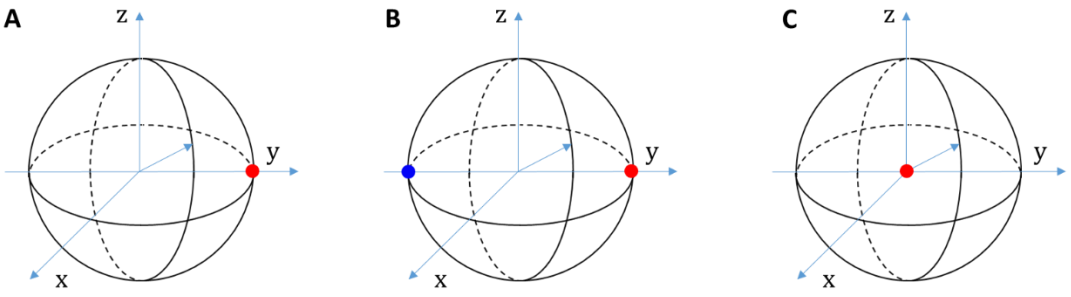

Figure 4.1. Schematic representation of (A) Luneburg, (B) Maxwell fish-eye, and (C) light concentrator Grin lenses.

4.2 Experimental section

4.2.1 Materials

Tetrachloroauric acid (≥99%, $HAuCl_4 \cdot 3H_2O$) and trisodium citrate dihydrate (≥99.5%, $C_6H_5Na_3O_7 \cdot 2H_2O$) were acquired from Acros Organics. 11-Mercaptoundecanoic acid (≥98%, MUA), ammonium hydroxide solution (29%, NH_4OH), branched polyethyleneimine (≥99.5%, PEI), poly(acrylic acid) sodium salt (≥99%, PAA), and sodium chloride (≥99.5%, NaCl) were purchased from Sigma-Aldrich. Benzenethiol (≥98%, BT) was acquired from Fluka. Silica beads (SiO_2 beads, 0.985 ± 0.04 µm) were purchased from Microparticles GMBH. All reactants were used without further purification. Milli-Q water (18 MU cm^{-1}) was used in all aqueous solutions, and all glassware was cleaned with aqua regia before the experiments.

4.2.2 Synthesis of citrate-stabilized spherical gold nanoparticles (AuNPs)

The whole set of AuNps with a diameter of ca. 47, 41, 25, 18, 14, and 12 nm approximately was prepared using the well-known seed growth method.[9] Gold seeds with a diameter of ca. 10 nm, were synthesized as follows. In a three-necked flask connected to a condenser, 200 mL of 2 mM $C_6H_5Na_3O_7 \cdot 2H_2O$ in Milli-Q water were heated. After boiling, 487 µL of $HAuCl_4$ 0.1M were injected. The mixture was let under vigorous stirring for 1 hour. The color of the solution changes, in a couple of minutes, from bluish-grey to pink and then turns into a stable deep red confirming the formation of gold seeds. The synthesis was cooled until 90˚C. Then, in the same vessel, 2 mL aliquots of $C_6H_5Na_3O_7 \cdot 2H_2O$ (60 mM) and $HAuCl_4$ (25 mM) solutions were sequentially injected (time delay of 2 min). By repeating their sequential addition, gold particles of different sizes (47 ± 2.0, 41.5 ± 4.6, 25.5 ± 2.5, 17.7 ± 1.9, 13.9 ± 1.3, and 11.8 ± 1.3 nm) were obtained. Finally, all gold colloids were cleaned by centrifugation once and redispersed in water for further codification.

4.2.3 AuNPs codification

The so-produced AuNPs were functionalized with a small amount of MUA (1.25 molecules per nm^2) to impart colloidal stability during the subsequent encoding process with BT as the Raman reporter.[10] A solution containing a calculated amount of NH_4OH 2.9% solution and MUA was prepared and rapidly added to the AuNPs. For the functionalization of 200 mL of ca. 47, 41, 25, 18, 14, and 12 nm size colloids, 0.591 mL, 0.680 mL, 1.011 mL, 1.507 mL, 2.066 mL, 2.506 mL of MUA 1mM were added. For, 47, 41, and 25 nm colloids, the following aliquots of NH_4OH 2.9% were respectively added: 1.606 mL, 1.849 mL, and 2.751 mL. The mixtures were left to react overnight under stirring. Then, 100 mL of the so obtained MUA stabilized particles

were encoded with BT. Briefly, to 100 mL of MUA functionalized colloids of ca. 47, 41, 25, 18, 14, and 12 nm size, aliquots of BT 10^{-4} M solutions yielding ca. 3 probe molecules per nm^2 of Au surface (0.710 mL, 0.816 mL, 1.213 mL, 1.809 mL, 2.407 mL, and 3.007 mL, respectively) were added under energic stirring. 1 hour later, the Au@MUA-BT nanoparticles were cleaned by centrifugation and characterized. Six batches of SERS-encoded nanoparticles of different sizes (Au_{47}@MUA-BT, Au_{41}@MUA-BT, Au_{25}@MUA-BT, Au_{18}@MUA-BT, Au_{14}@MUA-BT, and Au_{12}@MUA-BT).

4.2.4 SiO_2 beads polyelectrolytes wrapping

0.25 mg of SiO_2 beads were washed once and redispersed in 1 mL of water. Subsequently, samples were coated with polyelectrolytes using the layer-by-layer (LBL) method.[11] Briefly, 1 mL of washed SiO_2 beads was added dropwise to 10 mL of PEI (2mg/mL) aqueous solution previously sonicated for 30 min. The mixture was kept under stirring for 1 h and then centrifuged twice at 8000 rpm, 5 min. The pellet was collected and redispersed in 1 mL of water. The same protocol was applied for the other two polyelectrolyte layers: PAA (2mg/mL, in 0.5 M NaCl) and PEI (2mg/mL), both previously sonicated for 30 minutes. Finally, the polyelectrolytes coated beads were washed four times to remove any excess of unbound polymer and redispersed in 1 mL of water.

4.2.5 Assembly of SERS-encoded NPs onto polyelectrolytes-coated SiO_2 beads

For the assembly of the first layer composed of 47 nm particles, 1 mL of polyelectrolyte coated SiO_2 beads (0.25mg/mL) was added dropwise, under energic stirring, to 4 mL of the previously obtained MUA/BT encoded 47 nm AuNPs (Au_{47}@MUA-BT; ca. 4×10^{11} NPs/mL of beads). The sample was kept under stirring for 1h to maximize particle coating and, then, left to sediment overnight. The supernatant was discarded and the pellet composed of Au_{47}@MUA-BT coated beads (SiO_2@Au_{47}@MUA-BT) was washed twice and redispersed in 1 mL of water for further particle coating. The deposition of the subsequent set of nanoparticles was performed by wrapping the so-obtained gold-covered beads with PEI [12, 13] and repeating the procedure for the number of the calculated layers. The final system will be covered by 32 layers of AuNPs with decreasing diameters. Briefly, 1 mL of SiO_2@Au_{47}@MUA-BT was added dropwise to 10 mL of PEI (2 mg/mL, aqueous solution previously sonicated 30 minutes) under stirring which was maintained for 1 hour. Samples were then left to sediment and pellets represented by positively charged gold-covered beads were washed extensively in water to remove the excess of the unbound polymer. The so-obtained sediments were assembled again with 4 mL of the previously obtained Au_{47}@MUA-BT until the number of layers required for this size was achieved. The same

procedure was repeated for each calculated layer working with 6×10^{11}, 1×10^{12}, 3×10^{12}, 5×10^{12}, and 8×10^{12} NPs/mL of beads for ca. 47, 41, 25, 18, 14, and 12 nm AuNPs respectively. Finally, multilayered beads were extensively washed with 2 mL of Milli-Q water via overnight sedimentation. No centrifugation was used in any of the cleaning steps to avoid particle detachment.

4.2.6 Characterization

Microscopy. JEOL 1011 Scanning transmission electron microscope operating at an acceleration voltage of 100 kV was employed to obtain corresponding micrographs of samples that were prepared by drying water suspensions on carbon−Formvar-coated 200 mesh copper grids.

UV-Visible spectroscopy. The optical response and size of individual particles as well as multilayered beads were characterized using UV-VIS spectroscopy (Thermo Scientific Evolution 201).

SERS spectroscopy. SERS spectra were collected in backscattering geometry with a Renishaw inVia Reflex system equipped with a 2D-CCD detector and a Leica confocal microscope. Excitation of the sample was carried out with 785 and laser line with an acquisition time of 10 s and power at the sample of about 26 mW. The laser was focused onto the sample with an x50 objective providing a spatial resolution of ca. 0.9 µm. The corresponding SERS maps obtained in the same conditions show an area of 27 × 12 µm. 50 µL of samples were spin-coated onto an RCA cleaned glass slide ((1st ramp) 500 rpm, 10 s; (2nd ramp) 3000 rpm, 30 s, with an acceleration rate of 500 rpm s^{-1} for both ramps) to ensure a homogenous distribution of isolated beads.

4.3 Results and discussion

SERS-encoded nanoparticles comprising spherical gold cores of different diameters were fabricated following the protocol described by Pazos et al.[10] Citrate-stabilized spherical gold nanoparticles of 47 ± 2.0, 41.5 ± 4.6, 25.5 ± 2.5, 17.7 ± 1.9, 13.9 ± 1.3, and 11.8 ± 1.3 nm diameter size (Figure 4.2A) were first functionalized with a submonolayer of 11-mercaptoundecanoic acid (MUA) to impart colloidal stability (the carboxylate headgroups of MUA afford an overall negative charge to the nanoparticles) and, then, encoded with benzenethiol (BT) as the SERS label to yield ca. 3 probe molecules per nm^2. The following six batches of SERS-encoded nanoparticles were fabricated: Au_{47}@MUA-BT, Au_{41}@MUA-BT, Au_{25}@MUA-BT, Au_{18}@MUA-BT, Au_{14}@MUA-BT, and Au_{12}@MUA-BT. Figure 4.2B illustrates the normalized extinction spectra of each batch of nanoparticles while Figure 4.2C shows the SERS spectra of the SERS-encoded nanoparticles in suspension. The SERS intensity rapidly decreases with the nanoparticle size as a result of the corresponding drop in enhancing efficiency. The SERS spectrum of BT on gold nanoparticles displays the characteristic vibrational features of this molecular probe, such as the bands centered at 685 cm^{-1} (ring in-plane deformation), 995 cm^{-1} (CH in-plane deformation), 1022 and 1074 cm^{-1} (CC ring breathing).[14, 15]

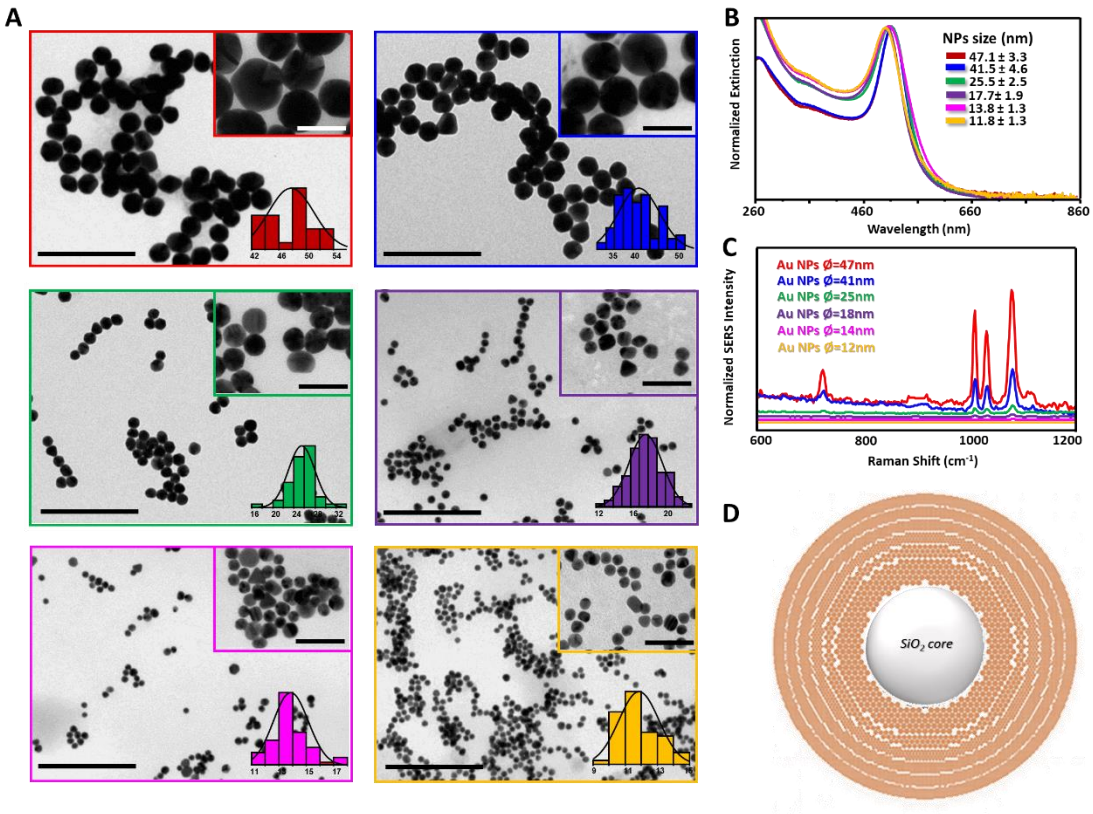

Figure 4.2. (A) representative TEM images with the corresponding histograms of particle diameter. (B) Normalized extinction spectra, (C) SERS spectra of Au@MUA-BT colloids and (D) Schematic representation of Grin Lens.

SiO_2 beads of ca. 1 µm diameter were coated with the first layer of Au_{47}@MUA-BT particle via layer-by-layer (LBL) method.[11] Briefly, pristine silica beads (ζ-potential = -55 mV) were consecutively coated with layers of polyelectrolytes of opposite charge (positively charged branched polyethyleneimine, PEI; poly(acrylic acid), PAA; and positively charged branched polyethyleneimine, PEI) to yield an external PEI shell with a compact collection of positive charges (+53 mV, Figure 4.2). An excess of Au_{47}@MUA-BT particles was then combined with the so-functionalized silica beads to yield hybrid plasmonic microparticles (Si@Au_{47}@MUA-BT, ζ-potential = -35 mV) via electrostatic adhesion.

A further PEI coating was carried out on the so-formed Si@Au_{47}@MUA-BT microparticles to reverse the surface charge (+40 mV), followed by a deposition of the second layer of Au_{47}@MUA-BT. The process was repeated to obtain 5 layers of Au_{47}@MUA-BT, 3 layers of Au_{41}@MUA-BT, 4 layers of Au_{25}@MUA-BT, 5 layers of Au_{18}@MUA-BT, 6 layers of Au_{14}@MUA-BT, and 9 layers of Au_{12}@MUA-BT for a total of 32 layers of SERS-encoded nanoparticles. The ζ-potential values were monitored after each step (Figure 4.3).

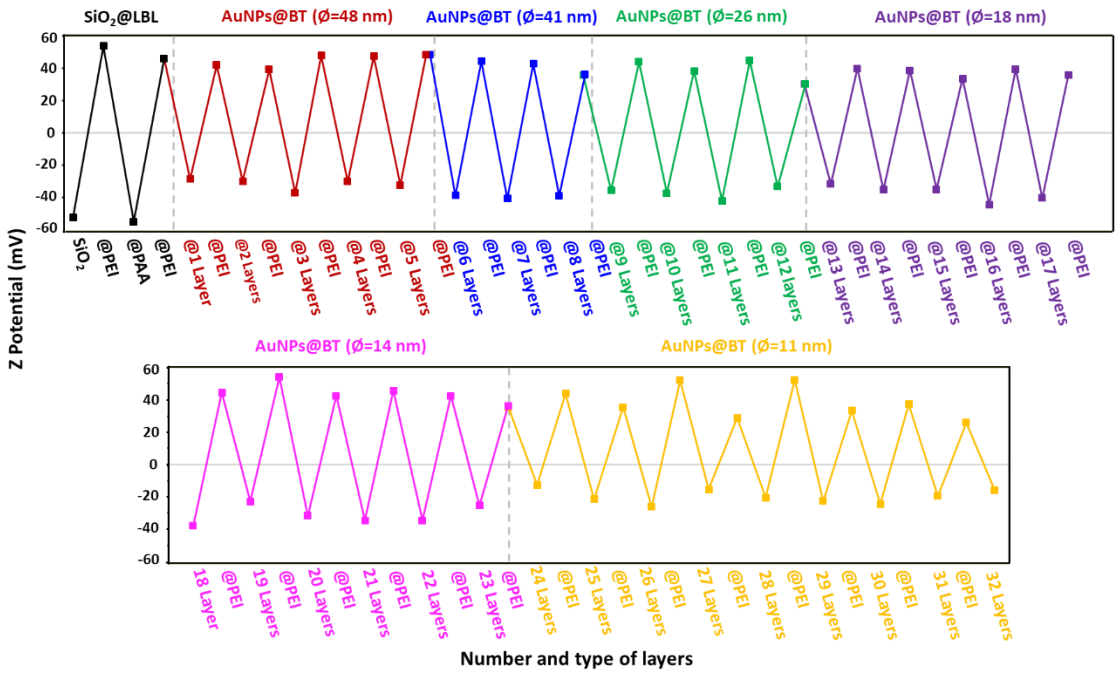

Figure 4.3. The plot represents ζ-potential values of Si@Au@MUA-BT from the 1st to 32nd layer.

The design of the complex material aims to yield a GRIN lens based on the self-assembling of SERS-encoded gold nanoparticles. The general features of the composite structure (i.e., silica and gold particle diameters, number of layers) were defined based on a theoretical model provided by Prof. Vincenzo Giannini (Instituto de Estructura de la Materia, CSIC).

Figure 4.4 and 4.5 shows representative TEM images of hybrid plasmonic microparticles after each deposition of SERS-encoded gold nanoparticles. Visual analysis of the images suggests the following. The first particle layer appears well distributed onto the bead surface thus resulting in a homogenous coating. As the deposition cycles proceed, especially from the ca. 5th to 15th layers, the hybrid microparticle beads progressively acquire a more pronounced asymmetric shape with spiked-like structures protruding from the core. This behavior is then reversed into a more regular sphere-like contour as further particle layers are integrated. These results can be interpreted based on the structural characteristic of the polymer interlayer employed in the synthesis (branched PEI). Because of its branched structures, PEI offers the possibility to anchor a greater number of particles than other tested polymers such as poly(diallyl dimethylammonium chloride) (PAH)[10, 16] which is key to achieving a dense nanoparticle distribution onto the bead surface. On the other hand, the extended ramifications of branched PEI together with the use of larger nanoparticles at the early stages of deposition may cause a certain degree of irregular arrangement caused by residual empty spaces randomly distributed over the external surface. Indeed, as the particle size is reduced (e.g., from the 15th

to 32nd layers), fewer and fewer empty spaces are detected, leading to multilayered beads with a more homogenous sphere-like profile.

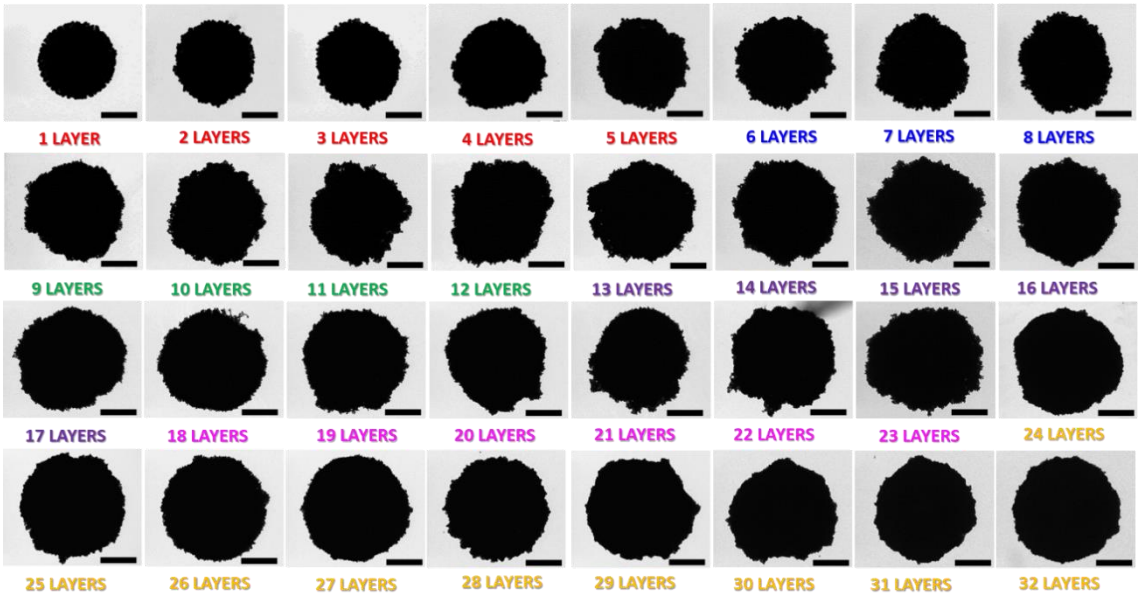

Figure 4.4. Representative TEM images of Si@Au@MUA-BT from the 1st to 32nd layer (scale bars = 500 nm).

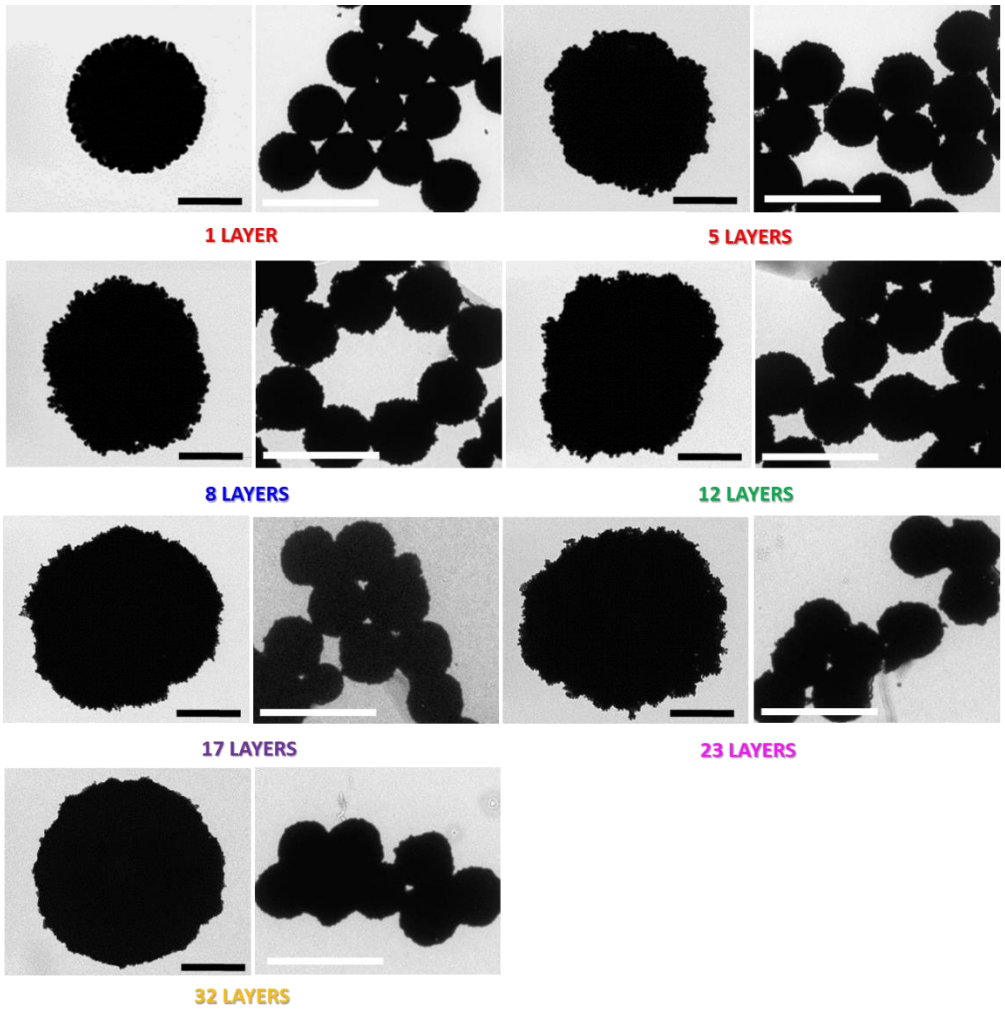

Figure 4.5. TEM images of 1st, 5th, 12th, 17th, 23th, and 32nd layers of Si@Au@MUA-BT chosen as representative low magnification micrographs (scale bars = 2µm). When otherwise indicated, scale bar = 500 nm.

The optical properties of hybrid material were also monitored via UV-Vis spectroscopy (Figure 4.6) and SERS spectroscopy (Figure 4.7). The extinction spectrum after the first coating with Au_{47}@MUA-BT exhibits an intense feature at ca. 560 nm with a long tail shoulder at a longer wavelength. Thus this result suggests the effective accumulation of the SERS-encoded structures onto the silica core and a certain degree of plasmon coupling at the bead surface (the LSPR of the individual colloidal nanoparticles is centered at ca. 533 nm, see Figure 4.2B). By increasing the NP deposition from ca. 1 to 5 layers, the broader contribution at longer wavelengths progressively redshifts while becoming the most prominent feature in the spectrum, indicating the larger extent of the interparticle coupling. As further layers of smaller nanoparticles are installed at the bead surface, the extinction spectra become very weak and featureless due to the damping of plasmon resonances via radiation scattering.[17]

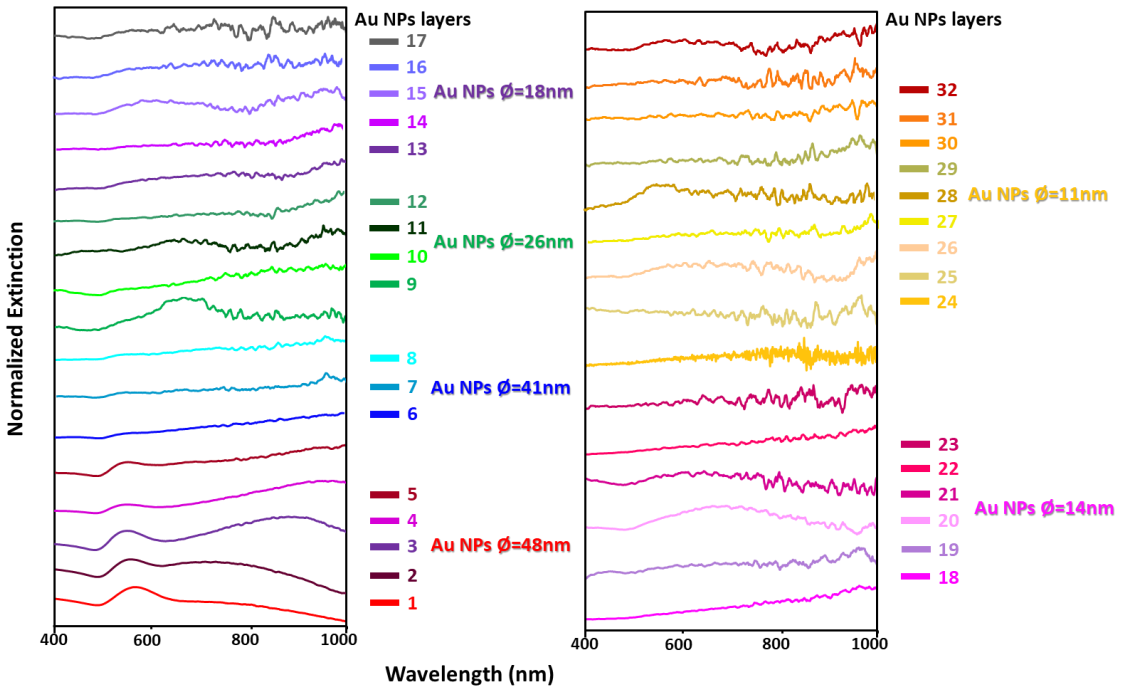

Figure 4.6. Stacked extinction spectra of Si@Au@MUA-BT from the 1st to 32nd layer.

SERS characterization was also carried out by spin-coating the individual beads on a glass support and acquiring SERS maps using a 785 nm laser line as the excitation source. The average intensity of the peak at 1070 cm^{-1} after each deposition of BT-encoded gold nanoparticles is represented in Figure 4.7. As extensively reported in the literature, the formation of a dense assembly of closely-spaced metal nanoparticles onto the silica beads promotes a dramatic intensification of the SERS signal as compared to isolated nanoparticles thanks to the generation of electromagnetic hot spots.[18, 19, 20, 21, 22] On the other hand, the collected spectroscopic data (Figure 4.7) clearly indicate that the overall SERS intensity rapidly drops when increasing the number of Au_{47}@MUA-BT layers from 1 to 5. An upsurge in signal intensity is observed after the first deposition of encoded particles of a smaller size (layer 5 to 6, Figure 4.7), which is then again followed by a decrease in SERS signal when further layers of Au_{41}@MUA-BT are deposited (from layer 6 to 8). This peculiar pattern is qualitatively repeated for each batch of SERS-encoded nanoparticles of a given diameter, although the maximum SERS intensity observed when transitioning from one nanoparticle size to the other appears to decrease with the AuNP dimension. These results can be precisely interpreted in the terms of a GRIN lens. As more layers of equally sized nanoparticles are deposited onto the microbead, the material behaviour approaches that of a metamaterial concentrating the light at the center of the sphere. This

corresponds to a reduction of the radiated power collected in the far field (i.e., decreased in registered SERS intensity). However, a disruption of the ordered periodic pattern of the plasmonic nanoparticles takes place when a new layer of SERS-encoded particles of a different diameter is assembled onto the substrates (e.g., from layer 5 to layer 6). This reduces the efficiency at focusing the EM waves at the designed focal point, as indicated by the larger SERS intensity collected at the detector.

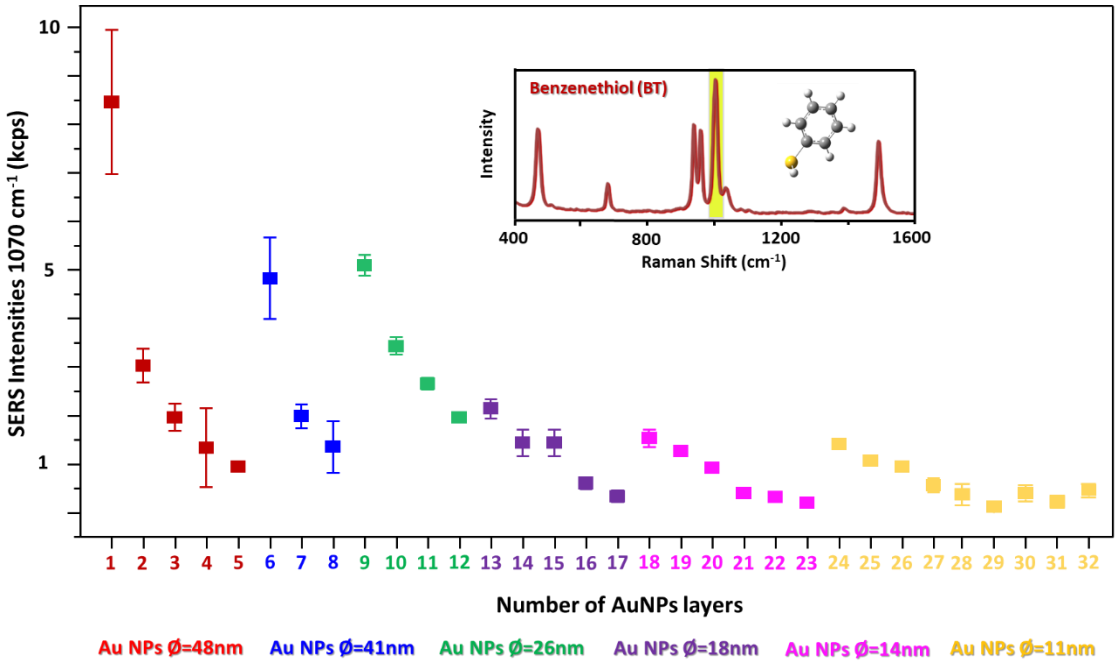

Figure 4.7. The plot represents averaged intensities at 1070 cm^{-1} of SiO_2@Au@MUA-BT from the 1st to 32nd layer. In the inset, the SERS spectrum of benzenethiol (BT) on hybrid microparticles.

4.4 Conclusions

A GRIN lens-like material was fabricated by depositing onto an inert silica core (1 um diameter) 32 layers of SERS-encoded nanoparticles comprising gold nanoparticles of decreasing diameter via electrostatic-mediated assembling. A step-by-step characterization of the complex material was performed using TEM microscopy, and extinction and SERS spectroscopies. The SERS response is consistent with that of a metamaterial concentrating the light at the center of the sphere.

REFERENCES

1. Huh, J.-H.; Lee, J.; Lee, S., Soft plasmonic assemblies exhibiting unnaturally high refractive index. *Nano Letters* **2020,** *20* (7), 4768-4774.
2. Kim, S.; Zheng, C. Y.; Schatz, G. C.; Aydin, K.; Kim, K.-H.; Mirkin, C. A., Mie-resonant three-dimensional metacrystals. *Nano letters* **2020,** *20* (11), 8096-8101.
3. Palmer, S. J.; Xiao, X.; Pazos-Perez, N.; Guerrini, L.; Correa-Duarte, M. A.; Maier, S. A.; Craster, R. V.; Alvarez-Puebla, R. A.; Giannini, V., Extraordinarily transparent compact metallic metamaterials. *Nature communications* **2019,** *10* (1), 1-7.
4. Paul, O.; Reinhard, B.; Krolla, B.; Beigang, R.; Rahm, M., Gradient index metamaterial based on slot elements. *Applied Physics Letters* **2010,** *96* (24), 241110.
5. Zhang, S.; Arya, R. K.; Whittow, W. G.; Cadman, D.; Mittra, R.; Vardaxoglou, J., Ultra-wideband flat metamaterial GRIN lenses assisted with additive manufacturing technique. *IEEE Transactions on Antennas and Propagation* **2020,** *69* (7), 3788-3799.
6. Zhao, Y. Y.; Zhang, Y. L.; Zheng, M. L.; Dong, X. Z.; Duan, X. M.; Zhao, Z. S., Three-dimensional Luneburg lens at optical frequencies. *Laser & Photonics Reviews* **2016,** *10* (4), 665-672.
7. Hu, C.; Xue, S.; Yin, Y.; Hao, Z.; Zhou, Y.; Chen, H., Acoustic super-resolution imaging based on solid immersion 3D Maxwell's fish-eye lens. *Applied Physics Letters* **2022,** *120* (19), 192202.
8. Valipour, A.; Kargozarfard, M. H.; Rakhshi, M.; Yaghootian, A.; Sedighi, H. M., Metamaterials and their applications: an overview. *Proceedings of the Institution of Mechanical Engineers, Part L: Journal of Materials: Design and Applications* **2021**, 1464420721995858.
9. Bastús, N. G.; Comenge, J.; Puntes, V., Kinetically controlled seeded growth synthesis of citrate-stabilized gold nanoparticles of up to 200 nm: size focusing versus Ostwald ripening. *Langmuir* **2011,** *27* (17), 11098-11105.
10. Pazos-Perez, N.; Fitzgerald, J. M.; Giannini, V.; Guerrini, L.; Alvarez-Puebla, R. A., Modular assembly of plasmonic core–satellite structures as highly brilliant SERS-encoded nanoparticles. *Nanoscale Advances* **2019,** *1* (1), 122-131.
11. Pastoriza-Santos, I.; Pérez-Juste, J.; Liz-Marzán, L. M., Silica-coating and hydrophobation of CTAB-stabilized gold nanorods. *Chemistry of Materials* **2006,** *18* (10), 2465-2467.
12. Kotov, N. A.; Dekany, I.; Fendler, J. H., Layer-by-layer self-assembly of polyelectrolyte-semiconductor nanoparticle composite films. *The Journal of Physical Chemistry* **1995,** *99* (35), 13065-13069.
13. Calderon, I.; Alvarez-Puebla, R. A.; Pazos-Perez, N., Gold-spiked coating of silver particles through cold nanowelding. *Nanoscale* **2021,** *13* (8), 4530-4536.
14. Pazos-Perez, N.; Guerrini, L.; Alvarez-Puebla, R. A., Plasmon Tunability of Gold Nanostars at the Tip Apexes. *ACS Omega* **2018,** *3* (12), 17173-17179.
15. Holze, R., The adsorption of thiophenol on gold–a spectroelectrochemical study. *Physical Chemistry Chemical Physics* **2015,** *17* (33), 21364-21372.
16. Turino, M.; Carbó-Argibay, E.; Correa-Duarte, M. A.; Guerrini, L.; Perez, N. P.; Alvarez-Puebla, R. A., Design and fabrication of bimetallic plasmonic colloids through cold nanowelding. *Nanoscale* **2022**.
17. Le Ru, E. C.; Etchegoin, P. G., *Principles of Surface-Enhanced Raman Spectroscopy*. Elsevier: Amsterdam, The Netherlands, **2009**.
18. Schwartzberg, A. M.; Grant, C. D.; Wolcott, A.; Talley, C. E.; Huser, T. R.; Bogomolni, R.; Zhang, J. Z., Unique gold nanoparticle aggregates as a highly active surface-enhanced Raman scattering substrate. *The Journal of Physical Chemistry B* **2004,** *108* (50), 19191-19197.
19. Pazos-Perez, N.; Wagner, C. S.; Romo-Herrera, J. M.; Liz-Marzán, L. M.; García de Abajo, F. J.; Wittemann, A.; Fery, A.; Alvarez-Puebla, R. A., Organized plasmonic clusters with high coordination number and extraordinary enhancement in surface-enhanced raman scattering (sers). *Angewandte Chemie International Edition* **2012,** *51* (51), 12688-12693.
20. Guerrini, L.; Rodriguez-Loureiro, I.; Correa-Duarte, M. A.; Lee, Y. H.; Ling, X. Y.; García de Abajo, F. J.; Alvarez-Puebla, R. A., Chemical speciation of heavy metals by surface-enhanced Raman scattering spectroscopy: identification and quantification of inorganic- and methyl-mercury in water. *Nanoscale* **2014,** *6* (14), 8368-75.
21. Turino, M.; Alvarez-Puebla, R. A.; Guerrini, L., Plasmonic Azobenzene Chemoreporter for Surface-Enhanced Raman Scattering Detection of Biothiols. *Biosensors* **2022,** *12* (5), 267.

22. Le Ru, E.; Etchegoin, P.; Meyer, M., Enhancement factor distribution around a single surface-enhanced Raman scattering hot spot and its relation to single molecule detection. *The Journal of chemical physics* **2006,** *125* (20), 204701.

GENERAL CONCLUSIONS

This dissertation mainly focused on exploring novel approaches for designing plasmonic nanomaterials and expanding the molecular library of surface ligands for SERS applications.

Firstly, the fabrication of bimetallic Au/Ag nanostructures via spontaneous nanowelding at room temperature remains a relatively unexplored route to generating novel plasmonic materials with unique features that otherwise cannot be obtained via conventional chemical reductions of metal salts in solution. Herein, it was carried out a systematic study on the cold-welding process of silver nanoparticles onto gold substrates that provides important insights into the role of different experimental parameters in determining the generation of well-defined bimetallic structures that retain the original gold substrate morphology. Secondly, a novel azobenzene derivative (AzoProbe) was successfully designed to yield highly SERS efficient and colloidally stable silver nanoparticle clusters for the sensitive detection and quantification of clinically relevant low molecular weight thiols. Finally, it was reported the production of a hybrid graded-index (GRIN) lens metallic metamaterial through the hierarchical assembly of gold nanoparticles onto a micrometric core of silica.

Accordingly, the main conclusions of the thesis can be summarized as follows:

(i) The formation of homogenous and smooth silver coating onto gold substrates of different geometrical features (bundles, nanorods, spheres) is favored by decreasing the silver nanoparticles size (from 43 to 15 nm diameter, approximately) while maximizing their surface loading. This latter factor is strictly related to the nature of the polymeric coating of gold substrates which mediates the electrostatic accumulation of silver nanoparticles onto the gold surface. Among different polymeric wrapping (poly(allylamine hydrochloride, PAH; polydiallyldimethylammonium chloride, PDDA; and branched polyethyleneimine, PEI), PEI showed the best result, which is possibly related to its branched structure. On the other hand, reducing the gold substrate overall dimensions (i.e., higher surface curvature) showed to slow the nanowelding process. A similar trend was observed by lowering the solvent polarity (from water to ethanol).

(ii) A mercapto-azobenzene probe (AzoProbe) was successfully synthesized as an efficient low-cost chemoreceptor for the SERS detection of biothiols. The AzoProbe was designed by combining 4-ATP and phenol through azo-coupling reaction. The reaction mixture was directly combined with silver nanoparticles without purification and the so-formed metastable

nanoparticle aggregates (Ag@AzoProbe) were further stabilized with thiolated PEG (Ag@AzoProbe@PEG). In the presence of the clinically relevant glutathione (GSH), the most abundant intracellular nonprotein thiol, the SERS signal of the AzoProbe underwent a drastic reshaping imposed by the GSH-mediated breakage of the diazo bond. The spectral alterations were quantitatively correlated with the analyte content showing a good linear relation in the ca. 7–100 nM range and an excellent limit of detection of ca. 5 nM. Other low molecular weight thiols (e.g., oxidized glutathione and cysteine) were also tested and an identical response was observed. Viceversa, in the case of thiolated macromolecules such as BSA, no distinguishable spectral alterations were detected, confirming the key role of PEG-SH in preventing the diffusion of large molecules close to the metal surface.

(iii) The complex architecture of the presented graded-index (GRIN) lens metallic metamaterial was carried out via electrostatic-mediated assembling achieving a dense-packed nanoparticle structure with a high degree of hierarchy. The characterization via TEM microscopy revealed an initial heterogenic distribution of particles which improves as the layering proceeds. The optical responses were characterized via extinction and SERS spectroscopies. Most notably, the SERS intensity displays a particular pattern that is consistent with the concentration of the light at the center of the microsphere.

In summary, this doctoral thesis provides contributions to the advancement of bimetallic plasmonic design and fabrication. Moreover, it expands the capability of SERS-based sensing at detecting and quantifying clinically relevant biomolecules, such as low molecular weight thiols, in complex fluids. Finally, it provides a novel experimental protocol to synthesize a graded-index (GRIN) lens metallic metamaterial using a micrometric silica core and ensembles of gold nanoparticles of different sizes.

ACKNOWLEDGMENTS

Few but significant lines to express my sincere gratitude.

I would like to acknowledge and give my warmest thanks to Prof. Ramón A. Álvarez-Puebla for the great opportunity he gave me to work in his group. Thanks to him I understood what it means to be a professional researcher.

A big debt of gratitude is owed to my supervisor Dr. Luca Guerrini who generously provided scientific knowledge and expertise and who also contributed to my personal growth with a crucial impact on my doctorate.

I also would like to thank Dr. Nicolas Pazos-Perez for the knowledge transmitted especially in the realm of nanoparticle synthesis with patience and dedication.

Last but not the least, I would like to dedicate special thanks to my colleagues, friends, and family for their support and encouragement.

APPENDIX I – List of Figures

APPENDIX II – List of Publications

M. Turino; E. Carbó-Argibay; M. A. Correa-Duarte*; L. Guerrini*; N. Pazos-Perez*; R. A. Alvarez-Puebla*. *Design and fabrication of bimetallic plasmonic colloids through cold nanowelding.* Nanoscale 2022, 14(26), 9439-9447.

M. Turino; N. Pazos-Perez; L. Guerrini*; R. A. Alvarez-Puebla*. *Positively-charged plasmonic nanostructures for SERS sensing applications*. RSC advances 2022, 12(2), 845-859.

M. Turino; R. A. Alvarez-Puebla*; L. Guerrini*. *Plasmonic Azobenzene Chemoreporter for Surface-Enhanced Raman Scattering Detection of Biothiols*. Biosensors 2022, 12(5), 267.

M. Blanco-Formoso; M. Turino; B. Rivas-Murias; L. Guerrini; A. Shavel; R. de la Rica; M. A. Correa Duarte; V. Salgueiriño*; N. Pazos-Perez*; R. A. Alvarez-Puebla*. *Iron-Assisted Synthesis of Highly Monodispersed and Magnetic Citrate-Stabilized Small Silver Nanoparticles*. The Journal of Physical Chemistry C 2020, 124(5), 3270-3276.

M. Blanco-Formoso; A. Sousa-Castillo; X. Xiao; A. Mariño-Lopez; M. Turino; N. Pazos-Perez; V. Giannini*; M. A. Correa-Duarte*; R. A. Alvarez-Puebla*. *Boosting the analytical properties of gold nanostars by single particle confinement into yolk porous silica shells*. Nanoscale 2019, 11(45), 21872-21879.

UNIVERSITAT
ROVIRA i VIRGILI